UNIVERSITY OF SOUTHAMPTON

FACULTY OF PHYSICAL SCIENCES AND ENGINEERING

Electronics and Computer Science

Rating Methodology of High Voltage Mass Impregnated DC Cable Circuits

by

Ziyi Huang

Thesis for the degree of Doctor of Philosophy

Octorber 2014

UNIVERSITY OF SOUTHAMPTON

ABSTRACT

FACULTY OF PHYSICAL SCIENCES AND ENGINEERING
ELECTRONICS AND COMPUTER SCIENCE

Doctor of Philosophy

RATING METHODOLOGY OF HIGH VOLTAGE MASS IMPREGNATED DC CABLE CIRCUITS

Ziyi Huang

With the continuing growth in energy consumption worldwide, the move towards a European wide super grid will result in significant changes in how modern transmission and distribution networks are operated. Fundamental to this is the need to accurately know or determine the available ampacity of high voltage cable circuits, because huge bulk power volumes need to be transmitted between maritime nations through dc power cables. Therefore, an accurate cable rating becomes paramount towards an efficient and safe operation of transmission networks, while the finance for large scale network construction schemes is limited.

Although the standardised thermal-limited rating has been successfully implemented for traditional ac cable networks for over 50 years, the move towards dc cable transmission imposes extra physical constraints on the cable rating, which are not considered by standard rating approaches. The two main concerns are the potential dielectric electrical breakdown prior to a normal thermal runaway and the development of dielectric cavities during cable cooling. In addition, the thermal-limited rating of submarine dc cable crossings, within a complex marine environment, requires an advanced numerical modelling method, where the traditional IEC thermal-limited rating method does not apply. Besides the technical value, significant interest exists both within the electrical power industry and organizations such as Cigré and IEC, because this work will inform future international standards for rating high voltage dc cables.

Considering the dielectric electrical stress constraint as the limiting factor for cable ratings, an analytical electrical stress-limited rating method has been developed and successfully benchmarked by numerical simulations for a practical cable design. This method allows ratings to be calculated against a criterion of maximum dielectric electrical strength.

Considering the dielectric cavity creation threshold as the limiting factor for cable ratings, a comprehensive study has been conducted, including thermal dynamics, theory of elasticity and electrical circuit theory. Subsequently, the analytical calculation of the cable internal pressure has been originally developed, together with a concept of the mechanical pressure-limited rating. The method has been successfully demonstrated for a practical cable design, yielding a rating which prevents the creation of cavity due to potential plastic deformations of the cable sheath.

When crossings are inevitably installed, cables are pushed towards their thermal limit, as a result of the mutual heating. In order to accurately rate these circuits under various ambient conditions; Finite Element Analysis (FEA) methods have been developed. Compared to the traditional IEC calculation, FEA modelling provides a more reasonable and accurate solution, by releasing idealistic assumptions in the IEC method. In addition, a systematic cable rating strategy has been suggested and successfully demonstrated through rating submarine high voltage dc cable crossings, which considers highly coupled physics: thermal, electrical and mechanical. In summary, this thesis contributes towards the modern rating methodology development for hvdc mass impregnated cable circuits, under a purpose of efficient and reliable long-term operation.

Contents

List of Tables

List of Figures

Symbols and Abbreviations

A	conductor cross section area	m^2
C	equivalent insulation electrical capacitance	F
C_p	specific heat capacity at constant pressure	$J.kg^{-1}.K^{-1}$
d	cylinder diameter	m
d_j	distance from the point under consideration to the actual buried cable j	m
$d_j{}'$	distance from the point under consideration to the image of buried cable j	m
D	electric flux density	$C.m^{-3}$
D_c	cable conductor outer diameter	mm
D_i	cable insulation outer diameter	mm
DF	de-rating factor for cable crossing	-
E	general electric field strength	$V.m^{-1}$
E_c	Young's modulus of conductor	$N.m^{-2}$
E_{const}	constant electrical stress at the middle of the insulation layer	$kV.mm^{-1}$
E_{geom}	geometric electrical stress	$kV.mm^{-1}$
E_i	equivalent Young's modulus of insulation	$N.m^{-2}$
E_L	Laplace field strength	$kV.mm^{-1}$
E_{mac}	macroscopic space charge field strength	$kV.mm^{-1}$
E_{max}	maximum long-term design stress of insulation	$kV.mm^{-1}$
E_{mic}	microscopic space charge field strength	$kV.mm^{-1}$
E_{pre}	preload steady state dielectric electrical stress	$kV.mm^{-1}$
E_r	local field strength at radius r	$kV.mm^{-1}$
E_s	Young's modulus of sheath	$N.m^{-2}$
E_{total}	total electric field strength	$kV.mm^{-1}$
E_{trans}	transient dielectric electrical stress	$kV.mm^{-1}$
E_Y	material Young's modulus	$N.m^{-2}$
f	operating voltage frequency	Hz
g	acceleration of gravity	$m.s^{-2}$
h_c	heat transfer coefficient of convection	$W.m^{-2}.K^{-1}$
i	dielectric leakage current	A
I	cable conductor current	A

$I_{thermal}$	cable current thermal-limited rating	A
I_{stress}	electrical stress-limited rating	A
$I_{pressure}$	mechanical pressure-limited rating	A
J	induced electric current density	A.m^{-3}
J_e	external current source	A.m^{-3}
k	general thermal conductivity	W.m^{-1}.K^{-1}
K_m	permeability of the medium	m^{2}
l	cable sample length	m
L	initial length before thermal expansion/contraction	m
L_c	characteristic length along the direction of growth (or thickness of the boundary layer)	m
L_h	laying depth of the heat source	m
L_r	laying depth of the rated cable	m
ΔL	change in length due to varying temperature	m
m	cementation exponent	-
N	thermal depolarization factor	-
p	pressure defined in Darcy's Law	N.m^{-2}
P_{cct}	cavity creation threshold pressure	N.m^{-2}
P_i	inner compressive pressure at r_i	N.m^{-2}
P_o	outer compressive pressure at r_o	N.m^{-2}
P_1	absolute interfacial pressure between conductor and insulation	N.m^{-2}
P_2	absolute interfacial pressure between insulation and sheath	N.m^{-2}
P_3	absolute compressive pressure from external pressure tapes	N.m^{-2}
q	general heat flux	W.m^{-3}
Q	total charge on the conductor surface	C
Q_h	rate of heat generation per unit volume	W.m^{-3}
Q_j	rate of charge generation per unit volume	C.m^{-3}
r	radius from the cable centre	mm
r_c	outer radius of cable conductor	mm
r_i	outer radius of cable insulation	mm
r_s	outer radius of cable sheath	mm
R_{ac}	ac resistance of conductor at its maximum operating temperature	Ω.m^{-1}
R_{dc}	dc resistance of conductor at its maximum operating temperature	Ω.m^{-1}

R_{eq}	equivalent radial resistance of the insulation per unit cable length	$\Omega.m^{-1}$
R_i	inner radius of the annulus	mm
R_o	outer radius of the annulus	mm
R_r	equivalent radial resistance between cable centre and radius r	$\Omega.m^{-1}$
$tan\delta$	dielectric loss factor	-
t	time	s
t_{slab}	backfill slab thickness	m
T	absolute temperature	K
T_{inner}	temperature of the boundary inner surface	K
T_{mh}	mutual thermal resistance between the rated cable and heat source	$K.W^{-1}$
T_{outer}	temperature of the boundary outer surface	K
T_{total}	total thermal resistance between annulus outer boundary and ambient	$K.W^{-1}$
T_1	thermal resistance per core between conductor and sheath	$K.W^{-1}$
T_2	thermal resistance between sheath and armour	$K.W^{-1}$
T_3	thermal resistance of external serving	$K.W^{-1}$
T_4	thermal resistance of surrounding medium	$K.W^{-1}$
$\mathbf{u}$	fluid velocity vector	$m.s^{-1}$
u	radial displacement	mm
u_f	flux rate	$m.s^{-1}$
U	operating voltage across the insulation	kV
U_0	phase voltage against ground	V
v	Poisson’s ratio	-
v_c	Poisson’s ratio of conductor	-
v_i	equivalent Poisson’s ratio of insulation	-
v_s	Poisson’s ratio of sheath	-
v_f	fluid kinematic viscosity	$m^2.s^{-1}$
V	initial volume before thermal expansion/contraction	m^3
ΔV	change in volume due to varying temperature	m^3
w	ground wind speed	$m.s^{-1}$
W_c	conductor joule loss per unit cable length	$W.m^{-1}$
W_d	dielectric loss per unit cable length	$W.m^{-1}$
W_h	heat generated by external heat source	$W.m^{-1}$

$W_{leakage}$	dielectric loss per unit cable due to leakage current	$W.m^{-1}$
W_s	sheath loss per unit cable length	$W.m^{-1}$
W_{tj}	total heat losses of cable j	$W.m^{-1}$
y	attenuation factor	-
α	temperature dependency coefficient	$℃^{-1}$
α_L	linear thermal expansion coefficient	K^{-1}
α_{Lc}	linear thermal expansion coefficient of conductor	K^{-1}
α_{Li}	equivalent linear thermal expansion coefficient of insulation	K^{-1}
α_{Ls}	linear thermal expansion coefficient of sheath	K^{-1}
$\alpha_{s\text{-}f}$	fluid/solid thermal conductivity ratio	-
α_V	volumetric thermal expansion coefficient	K^{-1}
α_{Vo}	volumetric thermal expansion coefficient of impregnant oil	K^{-1}
α_{Vp}	volumetric thermal expansion coefficient of Kraft paper	K^{-1}
α_{20}	constant mass temperature coefficient at 20 ℃	$℃^{-1}$
β_h	crossing angle between the heat source and rated cable	°
β_m	effective diffusivity of the saturated medium	$m^2.s^{-1}$
γ	field dependency coefficient	$mm.kV^{-1}$
γ_p	proximity effect factor	-
γ_s	skin effect factor	-
ε	general electrical permittivity	$F.m^{-1}$
ε_{ins}	insulation permittivity	$F.m^{-1}$
ε_r	relative permittivity of the insulation material	-
ε_{rock}	rock porosity related empirical parameter	-
ε_0	vacuum permittivity	$F.m^{-1}$
ϵ_z	mechanical strain in z direction (longitudinal)	-
θ	circumferential direction vector	-
θ_{air}	surrounding air temperature	℃
θ_{amb}	remote ambient temperature	℃
θ_c	cable conductor temperature	℃
$\theta_{critical}$	critical temperature between wet and dry zones	℃
θ_{drop}	temperature drop across the insulation	℃
θ_g	ground surface temperature	℃

θ_i	temperature at inner radius of the insulation	℃
θ_l	lower surface temperature of the slab	℃
θ_{local}	local backfill temperature	℃
θ_{max}	maximum operating temperature	℃
θ_o	temperature at outer radius of the insulation	℃
θ_r	local temperature at radius r	℃
θ_{rise}	temperature rise above ambient	℃
θ_s	sheath temperature	℃
θ_u	upper surface temperature of the slab	℃
θ_{vf}	dielectric cavity-free temperature during the impregnation process	℃
θ_w	cylinder surface temperature	℃
$\Delta\theta_d$	conductor temperature rise due to the dielectric loss	℃
$\Delta\theta_{max}$	maximum permissible temperature rise of cable conductor above ambient temperature	K
$\Delta\theta(0)$	conductor temperature rise at the crossing point due to the crossing heat source	℃
λ	dielectric thermal conductivity	W.m^{-1}.K^{-1}
λ_e	effective thermal conductivity of the rock/fluid system	W.m^{-1}.K^{-1}
λ_f	thermal conductivity of fluid phase	W.m^{-1}.K^{-1}
λ_{max}	maximum effective thermal conductivity	W.m^{-1}.K^{-1}
λ_{min}	minimum effective thermal conductivity	W.m^{-1}.K^{-1}
λ_s	thermal conductivity of solid phase	W.m^{-1}.K^{-1}
λ_1	sheath loss factor	-
λ_2	amour loss factor	-
μ_f	dynamic viscosity of the fluid	s.N.m^{-2}
ρ_c	static charge density	kg.m^{-3}
ρ_m	mass density	C.m^{-3}
ρ_0	reference electrical resistivity at 0 ℃ and 0 kV.mm^{-1}	Ω.m
ρ_{20}	reference conductor electrical resistivity at 20 ℃	Ω.m
ρ_{bf}	backfill thermal resistivity	K.m.W^{-1}
ρ_{dry}	thermal resistivity of drying-out backfill	K.m.W^{-1}
ρ_c	thermal resistivity of conductor	K.m.W^{-1}
ρ_{eq}	equivalent electrical resistivity of the cable insulation	Ω.m
ρ_i	thermal resistivity of insulation	K.m.W^{-1}

ρ_r	dielectric electrical resistivity at radius r	Ω.m
ρ_s	thermal resistivity of sheath	$K.m.W^{-1}$
ρ_{surf}	conductor surface charge density	$C.mm^{-2}$
ρ_t	general thermal resistivity	$K.m.W^{-1}$
ρ_{wet}	thermal resistivity of wet backfill	$K.m.W^{-1}$
σ_0	reference electrical conductivity at 0 ℃ and 0 $kV.mm^{-1}$	$S.m^{-1}$
σ	electrical conductivity at radius *r*	$S.m^{-1}$
σ_r	annulus radial stress	$N.m^{-2}$
σ_y	maximum yield shear stress	N/m^{-2}
σ_θ	annulus circumferential stress	N/m^{-2}
τ	cable insulation time constant	s
ϕ	porosity of the solid phase	-
Φ	electric field potential	V

Declaration of Authorship

I, Ziyi Huang, declare that this thesis and the work presented in it are my own and have been generated by me as the result of my own original research.

Rating Methodology of High Voltage Mass Impregnated DC Cable Circuits

I confirm that:

1. This work was done wholly or mainly while in candidature for a research degree at this university;
2. Where any part of this thesis has previously been submitted for a degree or any other qualification at this University or any other institution, this has been clearly stated;
3. Where I have consulted the published work of others, this is always clearly attributed;
4. Where I have quoted from the work of others, the source is always given. With the exception of such quotations, this thesis is entirely my own work;
5. I have acknowledged all main sources of help;
6. Where the thesis is based on work done by myself jointly with others, I have made clear exactly what was done by others and what I have contributed myself;
7. Parts of this work have been published as:
    - Z. Y. Huang, J. A. Pilgrim, P. L. Lewin, F. Waite and D. Payne, ‘Calculating the thermal impact of cable crossings’, *INSUCON 2013, International Electrical Insulation Conference*, 29 - 31 May 2013, Birmingham, UK, pp 185 - 190.
    - Z. Y. Huang, J. A. Pilgrim, P. L. Lewin, S. G. Swingler and D. Payne, ‘Current rating methodology for mass impregnated hvdc cables’, *IEEE 2013 Electrical Insulation Conference*, 2 - 5 Jun 2013, Ottawa, CA. pp 513 - 517.
    - Z. Y. Huang and J. A. Pilgrim, ‘Thermo-mechanical pressure analysis for hvdc cables’, *Jicable HVDC’13, European Seminar on materials for HVDC cables and accessories: Performance, Modelling, Testing, Qualification*, 18 - 20 Nov 2013, Perpignan, FR. CD-ROM.
    - Z. Y. Huang, J. A. Pilgrim, P. L. Lewin, S. G. Swingler and G. Tzemis, ‘Numerical thermo-mechanical stress analysis for hvdc cables’, *IEEE 2014 Electrical Insulation Conference*, 8 - 11 Jun 2014, Philadelphia, US. pp 387 - 391.

Signed: ……………………………………………………………………………………

Date: ……………………………………………………………………………………..

Acknowledgements

I would like to acknowledge the support of many people who have provided assistance in a wide variety of fields over the course of my PhD. Firstly I would like to acknowledge National Grid for funding the vast majority of the research contained within this thesis.

Particularly, I would like to express my greatest gratitude to Dr James A Pilgrim who has been helping me with various aspects of my academic progress, since my summer internship in 2010. He is more than just a great supervisor, but a trustworthy friend. I am also so grateful to Prof Paul Lewin and Prof Steve Swingler for their support and guidance over the course of my studies.

I would also like to thank a number of colleagues from the amazing Room 2029, Building 16, including Pedro Amaro, Dr Celia Yeung, Dr Richard Chippendale, Dr Matt Praeger, Dr Ian Hosier etc., for building up a pleasant atmosphere and friendship.

Finally I wish to acknowledge the overwhelming support of my parents (Kaisheng Huang, Hong Li) and fiancée (Zhihui Huang) throughout my ups and downs, over my time at the University of Southampton.

亲爱的主耶稣，我要把我今天所得的成就完全献给你，感谢你在我南安五年的时光中一直看护着我，感谢你对我无限的耐心。没有你，我不知道现在的我会是怎样，很可能就是一台负荷不断增加永远停不下来的机器，直到报废。感谢你教会我对错，感谢你让我有所依靠，感谢你向我显明生命除了工作，还有其他更有意义的目的。在我遇到困难的时候，你训练我坚持，等待和信心。 在我欢欣鼓舞的时候，你让我内心充满感恩。你用我习惯接受的方式对我说话，你一直带领着我前进。但是即使这样，我还是一个罪人，很多事情虽然知道是错，但依然难以战胜。我求主原谅我的过犯，赦免我的罪，并给我力量能过按你的计划活出一个圣洁的生命。原主永远与我同在，阿门。

Chapter 1

Introduction

Energy constitutes the physical foundation of the human civilization, with the majority being in the form of electricity throughout generation, transmission and distribution [1]. Although the traditional electrical industry has a long history of reliable operation, new challenges have arisen over the last 50 years to address technology innovations, such as the renewable energy generation and submarine HVDC power transmission.

1.1 UK's energy structure and power transmission

Marching into the 21st century, United Kingdom is facing a challenging transition period in power generation, transmission and distribution. Besides an estimated 30% - 100% increase of electricity demand by 2050 [2], a clear trend is to move from a low-efficiency, self-reliant, fossil-fuel heavy generation mix towards a high-efficiency, renewable, energy strategy.

1.1.1 Energy source & Power generation

According to [3], the UK energy consumption peaked at 3597 kilograms per capita of oil equivalent in 1990. Although the figure drops to 2997 in 2011 due to increasing immigration and an enhanced energy efficiency [4], it still exceeds the world average of 1890 kilograms by 60%. Detailed data is summarised in Table 1.1.

Table 1.1: Energy production and consumption from 1990 to 2011 (UK & World)

Region	**Energy production**		**Energy consumption**							
	Total*		Fossil fuel %		Nuclear %		Renewable %		Per capita**	
	1990	**2011**	**1990**	**2011**	**1990**	**2011**	**1990**	**2011**	**1990**	**2011**
UK	208	130	90.7	85.8	8.5	10.6	-	3.3	3597	2997
World	8823	13157	81	81.5	8.7	8.7	10.2	9.8	1665	1890

*thousand metric tons of oil equivalent **kilograms of oil equivalent

Note that the world renewable energy consumption percentage actually drops from 10.2% (1990) to 9.8% (2011), due to a huge increase of fossil fuel energy consumption from emerging countries.

Besides indicating a high living standard in the UK compared to the world average, Table 1.1 also shows two trends regarding the structure of the UK energy market.

- To sustain a high living standard, energy imports have been increased dramatically by 420% (from 2004 to 2010 [5]) to compensate a 37.5% drop in local energy production.

- The primary energy source is moving from fossil fuel (coal, oil, gas) towards other options such as nuclear power and renewable energy (wind, hydroelectric).

The UK's fossil fuel mainly comprises coal, oil and natural gas. In the early 1940s, 90% of the generating capacity was fired by coal, with oil providing most of the remainder. With the development of oil/ gas exploration & extraction technologies for both onshore (Amethyst, Armada, Ryedale etc.) and offshore (North Sea) applications, the contribution of coal-based electricity generation against the total generation had fallen to 33% of total generation by 2004, while gas and oil together contribute to a total of 41% [6]. Based on data in [7], the change of fossil fuel consumption (mainly for power generation, but not limited to) is plotted in Figure 1.1 below.

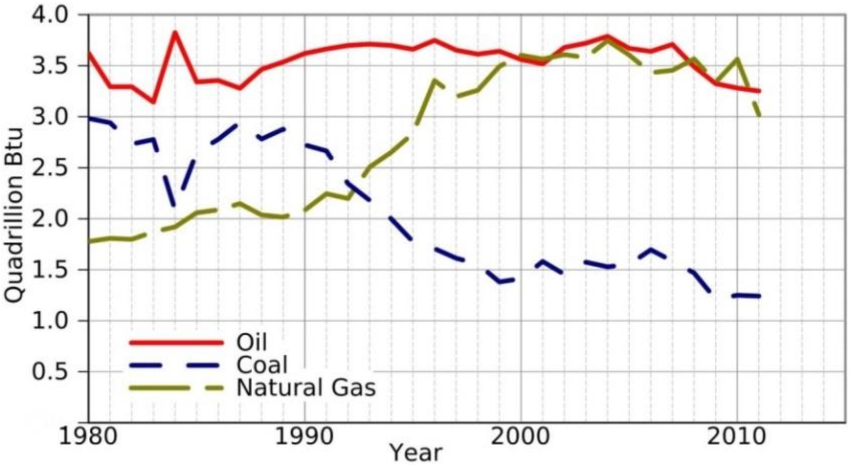

Figure 1.1: Fossil fuel consumption in the UK through the 90s [7]

In Figure 1.1, it is clear to see that the dropping coal consumption through the 1990s is mostly compensated by the increased natural gas consumption, while the consumption of oil remains steady. In another aspect, this trend requires and conceives a fast development of underground pipeline transmission.

The UK's commercial nuclear power industry started in 1956, and peaked in 1997 when 26% of the nation's electricity was supplied by nuclear power plants. However, with a rising concern of the safety and sustainability issues, a number of reactors have been closed and its share dropped to 19% in 2012 [8] (in Table 1.1, the figure is against the total energy consumption rather than the electricity generation). On one hand, nuclear power plants can be reliable (easily operating for 50 years) and 'clean' with little greenhouse gas emission in operation, provided that no major technical faults occur. As an example, Britain recently signed a £16bn contract with EDF in 2013 to build a low-carbon-emission nuclear plant in Hinkley [9]. On the other hand, catastrophic environmental problems result if a plant leaks or collapses, such as Fukushima Daiichi nuclear disaster (Japan, 2011) and Chernobyl nuclear station failure (Ukraine, 1986). Further, a high capital investment (towards 70% [10] to 80% [11] of the final electricity price) with a long construction period (minimum 5 years) is generally required. Therefore, the application of this technology is controversial in the UK and it normally comes as an alternative solution.

The UK's renewable energy mainly consists of wind power, as the UK is one of the best locations for wind power in the world and is considered to be the best in Europe [12]. According to [13], Britain aims to deliver 15% of its energy demand from renewable sources by 2020 and specifies a requirement for 30% renewable electricity generation through legislation [14]. Quantitatively speaking, the draft Electricity Market Reform (EMR) Delivery Plan shows a potential deployment of up to 16GW of offshore wind power by 2020 and up to 39 GW by 2030. As an example, the world's largest offshore wind farm (London Array, 630MW installed capacity) was opened in July 2013, at a value of £1.9bn [13]. Figure 1.2 shows the UK electricity generation from 1980 to 2011.

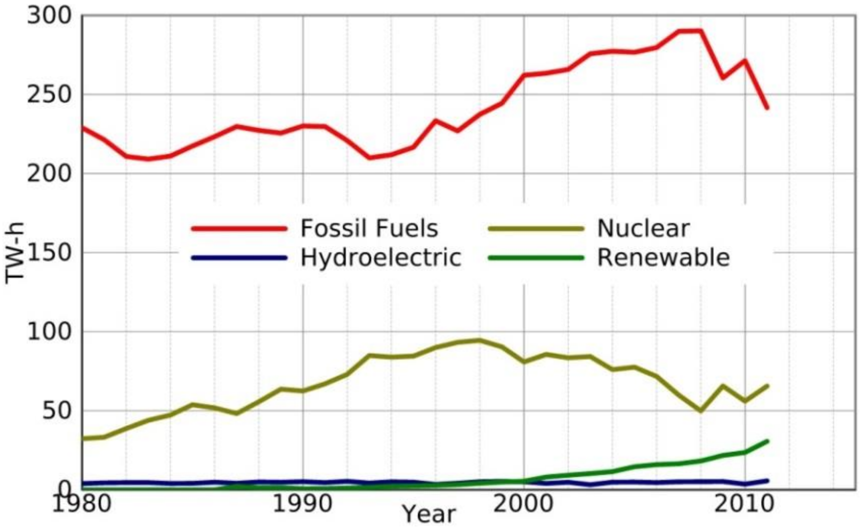

Figure 1.2: UK electricity generation from 1980 to 2011 [7]

In Figure 1.2, it can be shown that the fossil-fuel based generation has kept its dominant role over the last 30 years, but suffered from a long-term global economic recession starting in 2008. Conversely, renewable energy has witnessed a fast growth in the past 10 years under an increasing awareness of environmental sustainability.

In summary, oil, natural gas and wind power will take over the traditional coal fuel to fulfil the UK's long-term requirements for clean energy in the 21st century. Simultaneously, an upgrade of the existing power transmission network is necessary to support modern clean energy generation. For instance, transmission networks in areas with a high density of coal plants may begin to shrink, with much wind generation being in areas with little transmission infrastructure [15].

1.1.2 Power transmission & Technique

The traditional power network (c1900) started with a large number of isolated, small coal-fired generation stations, serving the needs of local areas. However, this type of generation was proved inadequate soon after the development of large-scale electricity-based applications (symbol of the second industrial revolution). In 1947, 625 municipal and privately owned electricity generation & supply utilities were merged into twelve electricity boards across the UK and then interconnected by a 132kV national grid [16]. Since then, the UK has experienced the construction of the 275kV and finally the 400kV supergrid which is still in place today, to fulfil a rapid growth in power demand. At the same time, high-capacity onshore generation stations were built close to coal fields (or coastal sites for nuclear power) to achieve high economic efficiency. However, a trend of growing offshore generation is expected towards 2030, which requires the development of long-distance, high-efficiency transmission technology.

In terms of onshore electricity transmission, utilities have a strong preference for overhead lines (OHL) rather than underground cables, stemming mainly from the economical fact that the OHL installation cost is much lower than the equivalent cable circuit. For instance, a study in 1996 suggests a cost ratio between 5 and 21 for ac systems operating between 220kV and 362kV [17]. Technically speaking, the overhead line has an intrinsic advantage in insulation with a much better heat dissipation performance, and is very suitable for large-scale power transmission. For instance, several 800kV OHL projects have been successfully commissioned and a further 1000kV link is scheduled in China [18] [19].

However, for power transmission across urban areas and offshore connections, cable transmission becomes preferable or the only practical option, as evidenced by the 1400km of high voltage (132/ 275/ 400kV) cable circuits operated by National Grid [20]. Figure 1.3 shows all the major scheduled offshore links towards 2020.

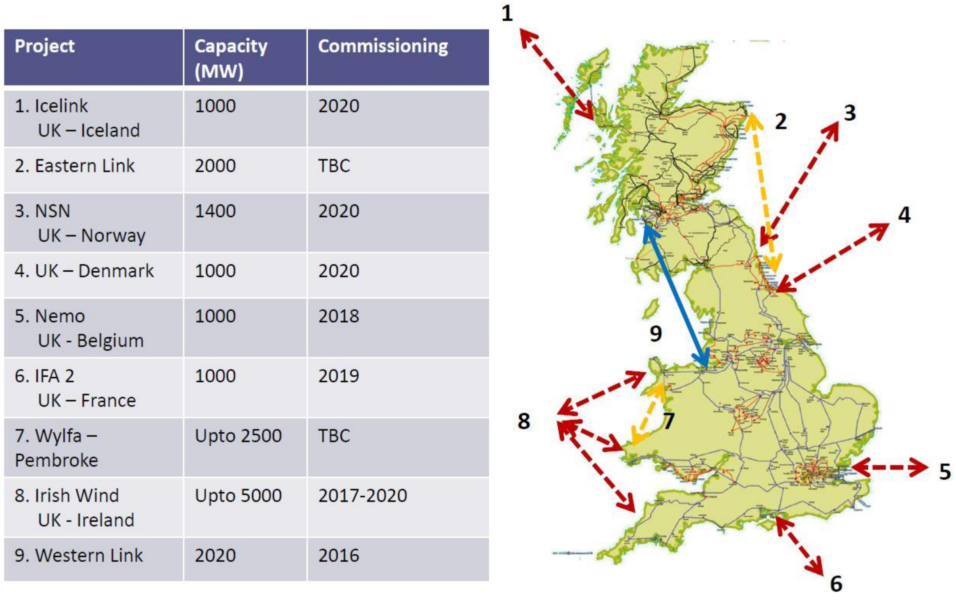

Project	Capacity (MW)	Commissioning
1. Icelink UK – Iceland	1000	2020
2. Eastern Link	2000	TBC
3. NSN UK – Norway	1400	2020
4. UK – Denmark	1000	2020
5. Nemo UK - Belgium	1000	2018
6. IFA 2 UK – France	1000	2019
7. Wylfa – Pembroke	Upto 2500	TBC
8. Irish Wind UK - Ireland	Upto 5000	2017-2020
9. Western Link	2020	2016

Figure 1.3: Major UK offshore links towards 2020 [21]

1.2 High voltage DC cable transmission

According to [22], the ac system dominated the development of modern electrical supply systems in the 20th century because of an easy transformation between generation, transmission and distribution voltages, thus delivering greater efficiency and controllability. However, by the 1950s there was a growing demand for long-distance transmission schemes and it became clear that in certain circumstances, there could be benefits from adopting a dc voltage. Figure 1.4 below shows a schematic HVDC transmission technology.

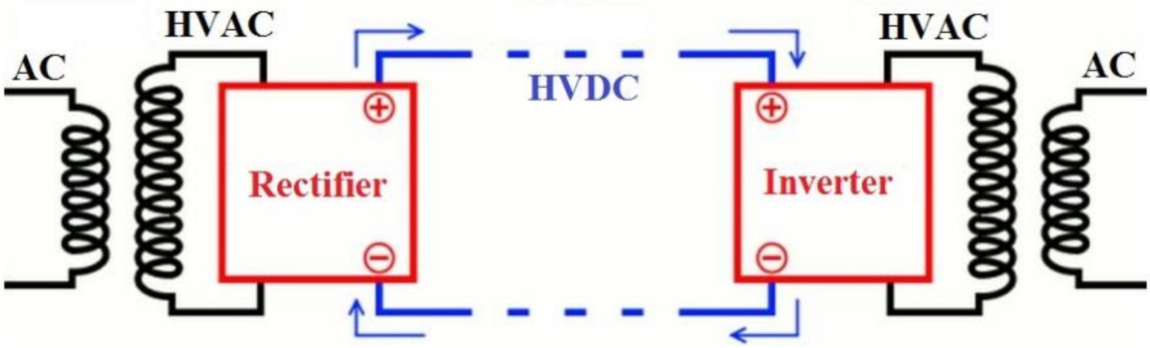

Figure 1.4: Schematic HVDC transmission technology

In Figure 1.4, the low voltage AC from the generating end (left hand side) will be firstly transformed to high voltage AC before getting rectified to DC. Then in the form of DC, power is transmitted to the receiving end (right hand side) through either overhead lines or power cables. At the receiving end, DC power will be inverted back to AC and then through a step down transformer before being distributed to customers. Compared to the widely used three-phase ac systems, dc systems have the following main advantages and disadvantages, as summarised in Table 1.2.

Table 1.2: Summary of direct current (DC) systems

Technical advantages	• Interconnect asynchronous networks operating at different frequencies. • Transmission distance is not restricted by stability. • Higher operating voltages and less loss than ac lines (no reactive power consumption). • Possibility of altering transmission directions without polarity reversal (voltage source converter technology).
Technical disadvantages	• Challenges for circuit breaking. • Voltage transformation is only achieved on the ac part of the system. • Require large filters to remove harmonics generated by converters. • Localised regions of high electric stress can be induced due to space charge accumulation in dielectrics.
Economic concerns	• The high capital investment for converter stations results in a critical transmission length above which the use of DC is more economical. (550 – 750km for overhead lines and 50km for cables)

Figure 1.5 below shows an economic comparison between AC and DC transmissions.

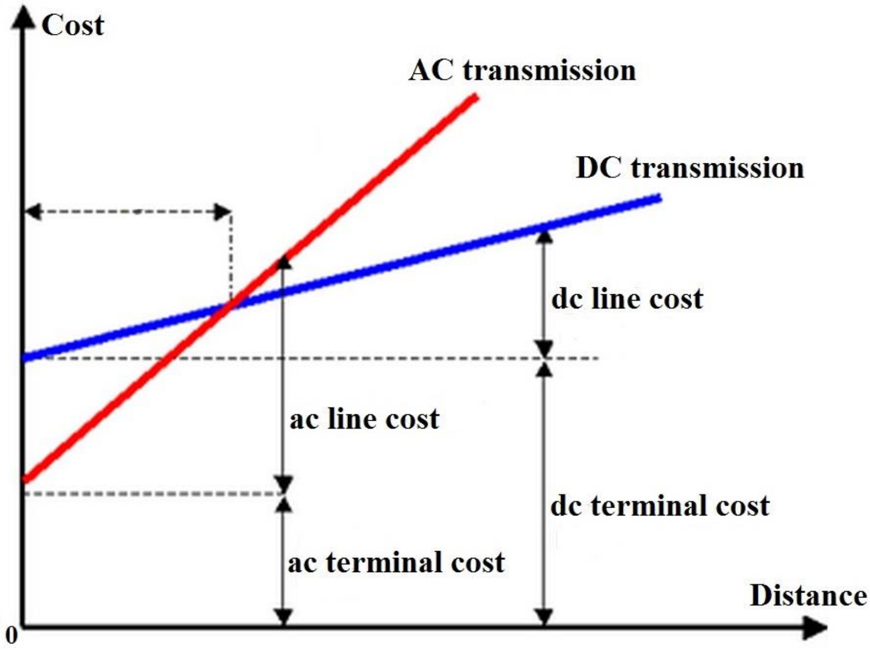

Figure 1.5: Economic comparison between AC and DC

From Figure 1.5, the main economic advantage of HVDC systems over AC is the high-efficiency transmission over long distances. Particularly, the critical distances (i.e. intersection point in Figure 1.5) for overhead line and cable applications are 550km and 50km respectively. As the UK's power generation will rely more and more on remote offshore wind farms (Round 3 offshore wind farm development [23]), HVDC transmission through submarine cables becomes the only practical solution. Submarine cables have five main applications as follows:

a. Power supply to islands

Power transmission between near-shore islands and the mainland grid can be operated through submarine power cables. This is normally done with medium-voltage ac submarine cable (≤ 52kV) with a rating of 10 to 30 MW per cable, for as described in [24]. Where power demand is higher, HVDC submarine power cables are chosen, such as those at Vancouver Island, Canada [25] and Shikoku Island, Japan [26].

b. Connection of autonomous girds

With the development of submarine power cable manufacturing and HVDC technology, autonomous ac grids with different operating frequencies can be connected, for example the 2000MW HVDC link between England and France [27]. In addition, extremely long-distance submarine power transmission can be applied through HVDC. For instance, the world longest submarine cable link is 580km (NorNed), and a number of 200+ km links are either in successful operation (BritNed, Baltic Cable, Swepol, Bass Link) or under construction (SAPEI) [28].

c. Offshore wind farms

Offshore wind farms (OWF) generally consist of hundreds of individual wind turbine generators (WTG) with a distance of 300 to 800m between every two WTGs. In large offshore parks, the WTGs are firstly connected by in-field three-phase ac cables to an offshore platform (converter station), where a submarine export cable can transmit bulk power back to onshore utilities. Although ac export cables are typically used for near-shore OWFs, the larger, more remote Round 3 installations in the UK waters are likely to use the HVDC technology. Further, the European Wind Energy Association (EWEA) has drawn a target of 40GW capacity installed by 2020 and 150GW installed by 2030 [29], which would need to be facilitated by the development of a submarine HVDC supergrid.

d. Supply of marine platforms

Production platforms in the offshore oil and gas industry have a large power demand for extracting hydrocarbons from wells, and this demand varies widely according to local circumstances and operational conditions. Currently, the electric power for many platforms is generated from locally produced natural gas in steam plants or gas turbines at a very low efficiency, making the on-board power generation costly [28]. With increasing power demand on offshore platforms, it becomes economically viable to transmit power from onshore grids to the platforms through submarine cables.

e. Short-haul crossings

Hundreds of submarine power cables, rather than overhead lines, have been installed to transport power across rivers, channels, straits or bays. One main advantage is that these cables do not restrict the height of ships passing through. For instance, the OHLs over the Ems River in Germany have to be shut down each time an upstream shipyard transports its new mega-size cruise ships to the North Sea. Moreover, submarine power cables normally have a longer lifespan and lower maintenance, while OHLs are exposed to potential hazards like storms, salt and ice deposition [28].

In summary, the future of HVDC cable transmission technology will be heavily linked to the development of the European supergrid, which requires a flexible control of power flow between different rigid systems with an efficient power generation and transmission. Under this blueprint, HVDC cable transmission (especially the submarine application) becomes the only rational solution if, for instance, the European continent plans to benefit from the potential for solar energy in North Africa or France wants to export its nuclear power to the UK. Figure 1.6 below outlines existing and potential HVDC links in Europe by 2050.

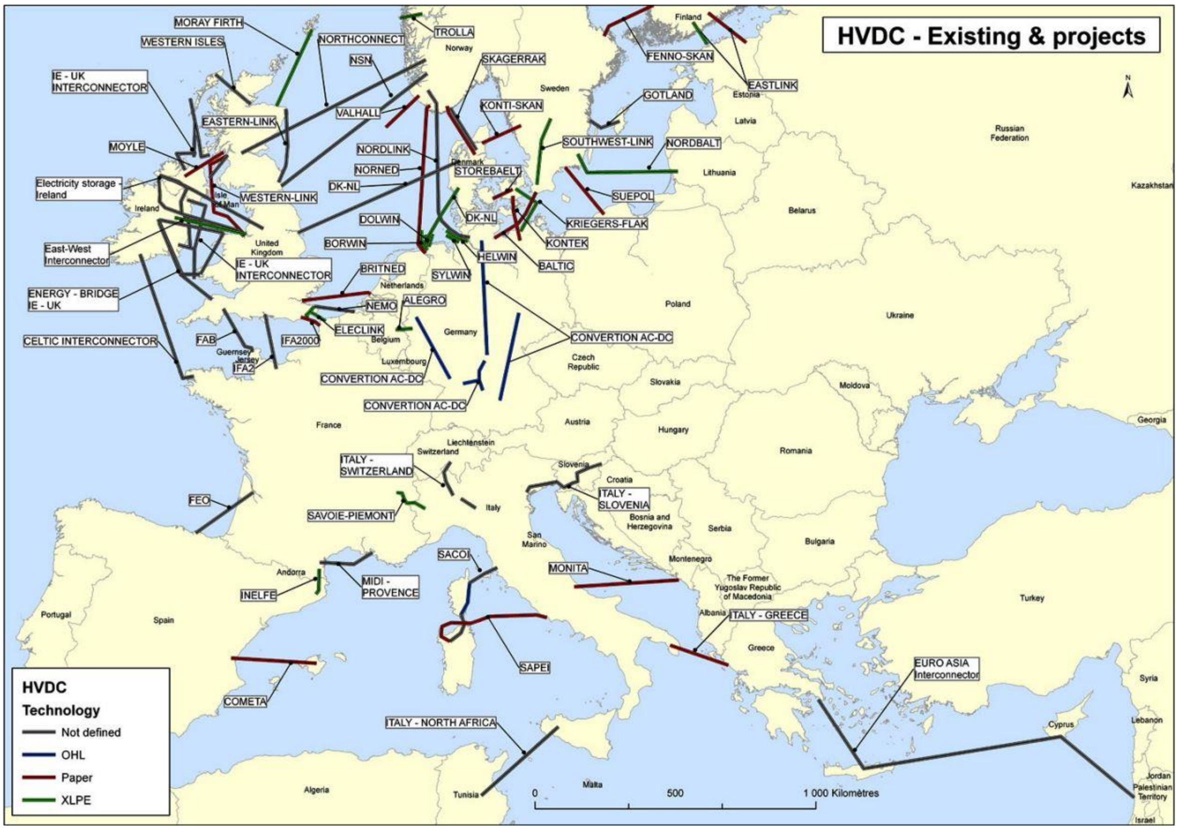

Figure 1.6: Existing and potential HVDC links in Europe by 2050 [30]

1.3 Research motivation

Under the existing thermal-limited rating method IEC60287-1-1 [31] (mainly for ac cables), the maximum conductor temperature is the only limiting factor on the rating calculation, e.g. 90 ℃ for cross-linked polyethylene (XLPE) and 50 ℃ for mass impregnated paper (MI paper). Although this thermal-limited rating works well for HVAC cables, it can only be applied to dc cables up to 5kV, where the associated dielectric electrical stress distribution is mainly regulated by the cable geometry and applied voltage (capacitively graded field) [32].

However, when considering HVDC cables, the permissible current is not only limited by the operating temperature, but also by the inverted electrical stress distribution within the insulation, owing to a resistively graded field caused by the leakage current. As a result, dangerously high electrical stress appears close to the insulation screen, which may cause a dielectric breakdown before any upper thermal limit is exceeded. Therefore the IEC60287 standard is considered insufficient for some HVDC applications because it fails to include the electrical stress limitation. At present, no calculation for the electrical stress-limited rating has yet been published.

In addition, for some mass-impregnated (MI) paper insulated HVDC cables, unacceptably high pressures or pressure drops occur at the insulation-sheath interface under rapid loading changes, due to a strong impregnant thermal expansion or contraction. As this can degrade cables by either causing sheath plastic deformations or introducing voids into the insulation, it is important to investigate and model this thermal-mechanical phenomenon. In other words, the cable rating can be mechanically limited by the pressure related cavity creation threshold. Similarly, no published method exists for rating cables where this limit may be an issue.

Further, practical concerns arise when rating high voltage cable crossings, where dangerously high temperatures can occur at crossing points. This may result in premature ageing of the cable insulation and potentially catastrophic failure. At present, the only explicit rating method, IEC60287-3-3 [33], is relatively conservative and adopts idealistic assumptions. In order to optimise the crossing capacity, it is necessary to consider convective ground surface, backfill drying out, subsea protection installations etc., through advanced numerical modelling techniques such as Finite Element Analysis (FEA). In other words, the developed modelling method provides an alternative way to approach the problem without any accuracy compromise, and it becomes the only method in certain cases where traditional analytical calculations are inapplicable.

1.4 Contribution of this thesis

In Summary, this thesis makes three significant contributions to the state of the art in the area of HVDC cable ratings. Firstly, the electrical stress-limited rating method for HVDC cables is developed, which considers the maximum allowable dielectric stress as the current limiting factor. More importantly, the method is developed in analytical format and subsequently demonstrated by numerical FEA modelling, which allows an easy review and application for practical users. The method described in this thesis has already proven valuable when applied to industrial R&D projects.

The second key contribution of this thesis is an original development of the mechanical pressure-limited rating method for HVDC cables, which sets the pressure-related cavity creation threshold as the limiting factor. In detail, this equation-based method involves highly coupled physics: theory of elasticity, thermal dynamics and circuit theory, and its applicability is demonstrated on a practical cable design.

The third key contribution of this thesis is the development of a numerical modelling method to evaluate high voltage cable crossing ratings. Throughout the FEA modelling, idealistic assumptions from the IEC method have been removed and key environmental factors affecting the rating calculation have been identified. In addition, protected submarine cable crossings have been investigated and analysed, for the first time. The method helps to remove the conservatism of the existing IEC method and delivers a more optimal solution.

Taken together, these three key contributions offer a significant step forward in the state of the art for HVDC cable circuit rating calculations, which will be of great value to the cable industry in building the offshore grid of the future.

1.5 Thesis structure

This chapter presents an overview of the UK's energy structure and related infrastructure system updates, which covers electricity generation, transmission and distribution. Among various solutions, power cable transmission with HVDC technology becomes the most preferable strategy for the UK to join a national or even European supergrid. Further, HVDC technology and relevant cable applications are summarised, with the main technical concerns being identified in applying this technology. The remainder of this thesis intends to address these concerns by developing advanced rating methods.

Chapter 2 undertakes a comprehensive literature review of high voltage cable technology, in order to provide the necessary context to the work. A summary of general cable category and insulation, a recap of existing cable rating methodology, and an in-depth explanation of high voltage cable designs (thermal, electrical and mechanical) are presented.

In Chapter 3, two nominal high voltage cable designs are presented with a full list of modelling parameters. In addition, standard FEA modelling techniques used in this thesis are outlined. Finally, a short discussion over the thermal effect from dc voltage ripple is presented.

Chapter 4 documents the in-depth development of the novel electrical stress-limited rating method for HVDC cables. This chapter firstly introduces several well established calculations related to the dielectric electric stress distribution, which will contribute to the subsequent method development. Secondly, the analytical derivation of the stress-limited rating and proposed solutions are presented before being benchmarked by numerical FEA modelling. Finally, applications of the developed electrical stress-limited rating are demonstrated under both steady state and transient operations.

In Chapter 5, the novel mechanical pressure-limited rating method has been originally developed, which aims to prevent dangerous dielectric cavity creation. This chapter firstly outlined the logic between various physics. Secondly, a detailed derivation of the cable internal pressure calculation as a function of current loading is presented. Finally, together with a cavity creation threshold, the mechanical pressure-limited rating is developed, with its applicability demonstrated.

In Chapter 6, numerical modelling method (FEA technique) is developed to evaluate high voltage cable crossing ratings for both onshore (HVAC) and offshore (HVDC) crossings. Its broad applicability is firstly demonstrated and compared to the IEC60287-3-3 through onshore HVAC crossings, which involves various ambient conditions. Subsequently, this method is extended to offshore submarine HVDC cable crossings, where the traditional IEC method is inapplicable due to a much more complicated installation environment.

1.6 Summary

This chapter has presented a broad review on the energy structure in the UK and the modern HVDC transmission technology. Specially, HVDC cables will play an increasingly important role in future power networks. This thesis has investigated the rating of such cable systems and contributed to understanding of the thermal, electrical and mechanical limiting conditions for HVDC cables in service.

Chapter 2

High Voltage Cable Technology

This chapter presents a comprehensive literature review of high voltage cable technology, providing the necessary background knowledge to support all the research in this thesis. Key issues addressed in this chapter include cable construction, insulation types, cable rating methodology development, and cable designs under dc voltages.

2.1 Cable construction

Historically, the power cable industry started in the early 20th century when engineers were able to transplant telegraph cable technology to original low voltage power cable designs. However, the 1st generation power cables suffered from a low operating temperature and weak dielectric strength.

To overcome these drawbacks, the innovative fluid filled (FF) cable was introduced in 1920 which has paper tapes wound around a copper conductor, with the whole assembly then being immersed in mineral oil or synthetic insulating fluid, contained within a metal sheath. This design massively increased the electrical breakdown strength of the insulation from 4 kV/mm to 40 kV/mm, enabling high voltage applications up to 400kV [34] and a maximum operating temperature up to 110 ℃ [35].

With an increasing demand for long-distance cable transmission, the traditional pressurised fluid filled cable shows potential problems of fluid leakage, pressure drop and complexity of jointing. An improved option is the so called ‘solid type’ cable which has either polymer or mass-impregnated paper as the main insulation material. According to [30], over 95% of HVDC cable transmission projects adopt the solid type cable. In Figure 2.1, the cross section of a nominal single-core, armour-free, solid type cable is outlined.

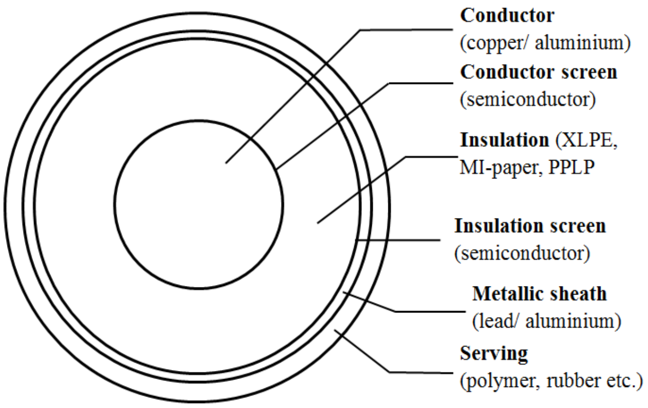

Figure 2.1: Cross section of the nominal single-core solid type cable

In Figure 2.1, the metallic conductor, either copper or aluminium, is normally manufactured in a stranded formation (Milliken) to minimise the skin effect in case of ac applications. Above the cable conductor, a thick insulation layer is attached with the material being either polyethylene-based or paper-based. In order to regulate the electric field distribution within the insulation, two thin layers of carbon-based semiconductors are inserted at the dielectric inner and outer radii, named conductor screen and insulation screen respectively. From the insulation screen outwards, the whole inner structure is surrounded by a reinforced lead or aluminium sheath to prevent moisture penetration and a final polymeric serving is laid to give a layer of extra protection. In submarine cable applications, metallic armour is found between the cable sheath and serving, which provides extra mechanical endurance. For detailed parameter values, refer to Chapter 3.

As dielectric innovation is the driving force for modern cable designs, it is necessary to review various widely used dielectric types. The two most common insulation types are polymeric materials (specifically XLPE) and Kraft paper.

2.1.1 Polymeric insulation

Polyethylene-based insulation has built up its reputation for high voltage cable applications since early 1960s, when thermoplastic PE was initially used for some 63kV cables [28]. At the same time, low-density polyethylene (LDPE), medium-density polyethylene (MDPE) and high-density polyethylene (HDPE) were examined and the main chemical difference among these three categories is the degree of chain branching. Normally, LDPE is more widely used as insulation material than the other two, while HDPE is mainly used as over sheathing [22].

In order to increase the maximum operating temperature of LDPE (70 ℃), cross-linked polyethylene (XLPE) insulation was developed, allowing 90 ℃ continuous operating temperature. Although early XLPE cables suffered from water-treeing effects (leading to reduced dielectric strength), modern manufacturing techniques, triple-extrusion and dry curing tubes, have largely eliminated the water-treeing problem. In addition, its maintenance-free property is beneficial for submarine cable applications.

However, one drawback of the XLPE insulation is its low carrier mobility and high charge trapping rates, which gives rise to an accumulation of space charge under dc applications. Consequently, local electrical stress can be increased by 5 to 8 times, which greatly increases the possibility of an electrical breakdown [36]. In addition, the fact that XLPE is not biodegradable may arise some environmental concerns.

Recent innovations of polymeric insulation are focusing on minimizing the dielectric space charge accumulation by adding a type of conductive or polarized inorganic fillers [37] [38]. However, commissioned dc links with XLPE insulation can only operate up to 320kV at present.

2.1.2 Paper-based insulation

Compared to polymeric insulation, paper-based insulation cables have a much longer service history and also have a higher electrical breakdown strength and a better space charge resistance under dc applications. The classical paper insulation design for HVDC submarine cables is to impregnate Kraft paper with pressurized low-viscosity oil.

In early installations, three common types are named low-pressure oil-filled (LPOF), self-contained oil-filled (SCOF) and self-contained fluid-filled (SCFF) with oil as the main insulation impregnant for the first two types and synthetic fluid for the third type [22]. On one hand, a big advantage for all the three types is that the positive dielectric internal pressure feature helps to minimize the creation of cavities, which guarantees a high dielectric strength during thermal cycles. Moreover, the LPOF design allows operations at extremely high temperatures (>100 ℃ [35]), due to an effective heat dissipation through the moving oil. On the other hand, all the three designs can contaminate the environment once leakage occurs. Also for the LPOF design, a sufficient oil flow can only be guaranteed for 30km to 60km and it has a higher financial cost due to the requirement for external oil feeding units to maintain the necessary internal pressure.

In order to address the environmental issue and increase the transmission distance, the mass-impregnated (MI) design became an alternative, which was first applied to the Moutiers – Lyon dc link in 1907 [39]. This type of insulation comprises several layers of pressurized Kraft paper, which are fully impregnated with a high-viscosity component (oil T2015 [40]). Compared to traditional oil-filled or fluid-filled cables, the MI paper insulated cable is maintenance free and does not leak impregnant when damaged. In practice, the mass impregnated design is the dominant solution for long-distance submarine HVDC transmission under operating voltages from 320kV up to 550kV [41]. However, this insulation type can only sustain an operating temperature up to 55 ℃.

For Submarine transmission with operating voltages over 550kV, the mass impregnated polypropylene laminated paper (PPLP) insulation is the only commercially available option, with a record 600kV HVDC line being commissioned in the UK [42]. The construction of PPLP consists of a layer of extruded polypropylene (PP) film sandwiched between two Kraft paper layers. Thanks to the physical properties of PP film, PPLP has a better dielectric strength under both ac and dc voltages and a lower dielectric loss than the conventional Kraft paper insulation [43 - 45]. Figure 2.2 below shows the construction of PPLP.

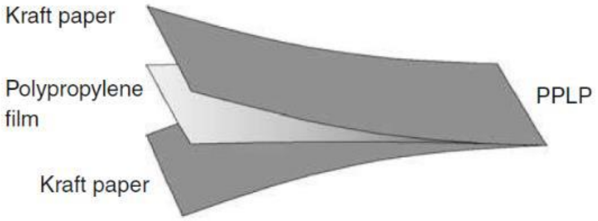

Figure 2.2: PPLP construction [28]

Once cables are manufactured, experimental tests are conducted to ensure the integrity of the product. Routine and type tests are suggested by Cigré for high voltage operations, loading cycles, polarity reversals and surges [46] [47]. However, such tests may need to be revised in order to address modern insulations with improved electrical characteristics (e.g. modified XLPE) and more complex multi-layer construction (PPLP) [48].

2.2 Cable rating methodology development

Before conducting the derivation of new rating methods for HVDC cables, it is necessary and beneficial to review the historical development of the cable rating methodology in order to fully understand the existing IEC method as well as its potential drawbacks. Generally, the development can be characterized into the following two categories since 1940s.

- Thermal network analogue and detailed lumped parameter method
- Computational finite difference/ element method

2.2.1 Thermal network analogue and Detailed lumped parameter method

Under steady state analysis, the cable cross section can be modelled as thermal resistors connected in series from the conductor outwards, in the radial direction. This approach forms a one dimensional thermal network with each annular cable component being represented by a thermal resistor, assuming homogeneous physical conditions within each component [49]. By introducing thermal capacitances, transient thermal-limited rating calculations can be developed for both cables and joints, which require a two dimensional thermal network with both radial and longitudinal elements [50-52]. However, the accuracy largely depends on the number of elements and it requires geometric simplifications to make the network solvable.

With the aim to increase transmission capacity, through allowing higher load currents, fluid filled cables began to be used with water pipe cooling cable systems [53]. The previous coarse thermal network analogue evolved to the detailed lumped parameter method, by increasing the number of subdivisions and introducing partial differential equations (PDEs) to describe the effect of oil flow in SCFF cables, or water coolant in pipes [54] [55]. However, one difficulty is that this method requires a mixed solving strategy linking thermal network calculations on different cable cross-section slices to PDEs which describe the longitudinal heat transfer. In addition, for a 2D slice analysis, geometric simplifications are still necessary and some components must be assumed isothermal.

2.2.2 Finite difference method and Finite element method

The computational finite difference method was introduced to improve the accuracy of transient rating calculations, where the radial heat transfer dominates over the longitudinal transfer [56]. The method requires many more nodes than the lumped parameter method in order to accurately represent the heat generation by dielectric losses and the heat transfer between the cable and surrounding environment. However, it requires a software implementation and for cable rating applications in [56], its accuracy may reduce for steady state analysis because some assumptions are more suitable for transient calculations, such as constant backfill thermal properties.

By adopting the idea of dividing a continuum into small finite elements [57], the FEA technique transforms a continuous global physical problem in PDEs into a discretized local finite element problem in the form of either algebraic equations or ordinary differential equations (ODEs). Therefore, without the need for idealistic assumptions, more realistic physical conditions can be assigned to different nodes using PDEs. Compared to the finite difference methods, FEA is more powerful and flexible especially for complex geometries where a traditional rectangular meshing cannot easily be applied. Many researchers have applied this technique to cable rating calculations [58] [59] and the IEC TR 62095 [60] has been issued to standardise the relevant calculations. With the advance of modern computing power and commercial FEA software packages, large scale 2D/ 3D FEA models have become viable for cable applications which include complex layouts with or without a geometric symmetry. However, the tricky part of this technique is to build the smallest possible model which still accurately captures the thermal behaviour of the cable system. Although challenging, this is now possible and can be deployed for cable crossings as demonstrated in [61]. Note that more details of this method can be found in Chapter 3.

2.2.3 IEC 60287 thermal-limited rating

The IEC60287 thermal-limited rating for directly buried cables or cable crossings is relatively simple to apply, but may not satisfy certain accuracy requirements because the calculation is somewhere between being the thermal network analogue method and the detailed lumped parameter method. It adopts a simple 1D thermal network representation for radial heat transfer within the cable cross section (IEC60287-1-1 [31]) and applies partial differential equations to describe longitudinal heat transfer (IEC60287-3-3 [33]). The general rating equation for single ac cables is defined as:

$$I_{thermal} = \left[\frac{\Delta\theta_{max} - W_d[0.5T_1 + n(T_2+T_3+T_4)]}{R_{ac}T_1 + nR_{ac}(1+\lambda_1)T_2 + nR_{ac}(1+\lambda_1+\lambda_2)(T_3+T_4)}\right]^{0.5} \tag{2.1}$$

Where; $I_{thermal}$ is the cable thermal-limited rating [A], $\Delta\theta_{max}$ the maximum permissible temperature rise of the conductor above ambient temperature [K], R_{ac} the ac resistance of conductor at maximum operating temperature [Ω.m^{-1}], W_d the dielectric loss per unit cable length [W.m^{-1}], λ_1 the sheath loss factor, λ_2 the armour loss factor, n the number of conductors, T_1 the thermal resistance per core between conductor and sheath [K.W^{-1}], T_2 the thermal resistance between sheath and armour [K.W^{-1}], T_3 the thermal resistance of external serving [K.W^{-1}], and T_4 is the thermal resistance of surrounding medium [K.W^{-1}].

For dc cables, the dielectric loss W_d, the sheath loss λ_1 and the armour loss λ_2 in (2.1) are removed and a simplified rating equation (up to 5 kV) is derived as:

$$I_{thermal} = \left[\frac{\Delta\theta_{max}}{R_{dc}T_1 + nR_{dc}T_2 + nR_{dc}(T_3 + T_4)}\right]^{0.5} \tag{2.2}$$

Where; R_{dc} is the dc resistance of cable conductor at maximum operating temperature [$\Omega.m^{-1}$]. However, both (2.1) and (2.2) ratings are only thermal-limited and are believed to be insufficient for modern HVDC applications under electrical and mechanical constraints.

2.3 High voltage DC cable electrical design

The main challenge for the electrical design of HVDC cables is to simultaneously determine both the thermal field and the electric field distribution within the insulation. Owing to the dielectric electrical conductivity being dependent upon both local temperature and electric stress under dc voltages, a resistively graded field develops instead of a classic (under ac voltages) capacitively graded field. Based on an empirical electrical conductivity equation, two scenarios may occur.

1. Field reversal results where the highest stress is found at the interface between the insulation and sheath. Because the stress is believed to be determined by the temperature difference across the insulation rather than the absolute temperature [62], electrical breakdown may occur before a thermal limit is exceeded.
2. Under high local temperature and electric field, a positive feedback loop may develop between the dielectric leakage current and its resulting heat losses. The joule loss due to the leakage current heats up the insulation, which in return leads to an even higher leakage current through the temperature dependence of the dielectric electrical conductivity (assuming that the extra heat cannot dissipate efficiently into ambient). Consequently, a thermal runaway can occur.

Generally speaking, the first scenario is due to the distribution of macroscopic space charge (across the whole insulation) and the second scenario is identified as an intrinsic thermal breakdown through a mathematic derivation [63].

At present, a big challenge is that all the previous studies can only deal with either scenario 1 or 2 one at a time, while they are actually happening and affecting each other simultaneously. Moreover, when the microscopic space charge (on interfaces) is also included, the electric field will be further distorted (Figure 2.4) and the calculation of the field distribution gets much more complicated.

2.3.1 Space charge creation and modified electric field

Generally speaking, the dielectric space charge creation and accumulation are related to the following three phenomena. The first phenomenon accounts for a macroscopic space charge accumulation and the other two result in the microscopic space charge accumulation.

1. Dielectric electrical conductivity gradient
2. Electrode charge injection/ polarization of dielectric residual charges
3. Trapping of charge within nonhomogeneous dielectrics (e.g. interfaces)

Normally, phenomenon 1 is observed for HVDC cables with a temperature gradient across the insulation [64] [65]. Derived from experimental data, the dielectric conductivity is an exponential function of both local temperature and electrical stress. To explain how this conductivity gradient causes a global macroscopic space charge distribution, a brief mathematical derivative is presented. In the electrostatic theory, (2.3) below indicates that the divergence of net electric flux density, D, through a closed surface equals to the net charge density, ρ_c, enclosed by the same surface.

$$\rho_c = \nabla_{div} D = \nabla_{div}(\varepsilon E) \tag{2.3}$$

Where; ε is the general electrical permittivity [F.m^{-1}] and E is the general electric field strength [V.m^{-1}]. Since even the best dielectric possesses some degree of conductivity, electric field strength is thus linked to current density, J, through electrical conductivity, σ, as:

$$J = \sigma E \tag{2.4}$$

By substituting (2.4) into (2.3) and calculating the divergence, following equation results:

$$\rho_c = \nabla_{div}\left(J \frac{\varepsilon}{\sigma}\right) = \frac{\varepsilon}{\sigma}\nabla_{div}(J) + J\nabla_{grad}\left(\frac{\varepsilon}{\sigma}\right) \tag{2.5}$$

Where; ∇_{grad} is the gradient operator. As the divergence of current density equals to the changing rate of charge density against time, i.e. $\nabla_{div}(J) + \partial\rho_c/\partial t = 0$ (continuity equation), (2.5) becomes:

$$\rho_c = -\frac{\varepsilon}{\sigma}\left(\frac{\partial \rho_c}{\partial t}\right) + J\nabla_{grad}\left(\frac{\varepsilon}{\sigma}\right) \tag{2.6}$$

Under steady state (i.e. $\partial\rho_c/\partial t = 0$), (2.6) is simplified into (2.7).

$$\rho_c = J\nabla_{grad}\left(\frac{\varepsilon}{\sigma}\right) \tag{2.7}$$

Based on (2.7), macroscopic space charge is continuously distributed across the entire insulation for dc cables, provided that the insulation has constant dielectric leakage current and permittivity, but a varying dielectric electrical conductivity (i.e. $\nabla_{grad}(\varepsilon/\sigma) \neq 0$). In [66], the macroscopic space charge accumulation is suggested as an inherent consequence of the non-uniform variation in the dielectric electrical conductivity. A typical effect of the macroscopic space charge accumulation is the 'field inversion', shown in Figure 2.3.

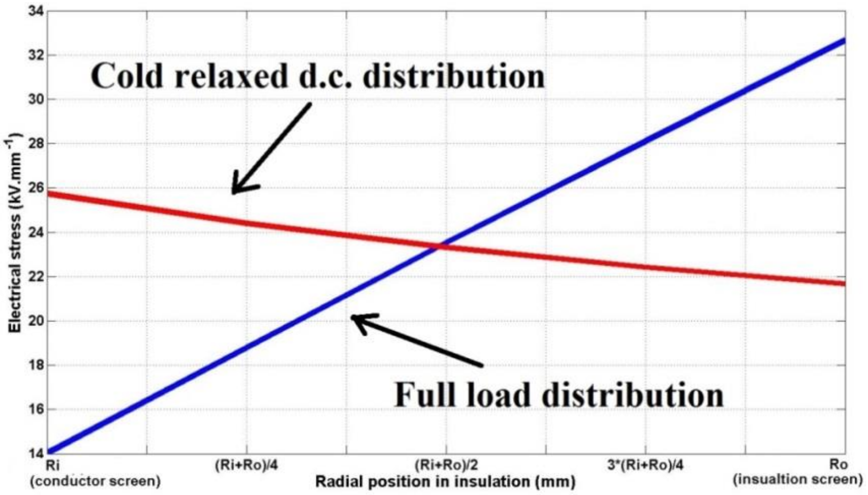

Figure 2.3: Electric stress in dc cable insulation under different load conditions

In Figure 2.3, the cold relaxed dc distribution is similar to the capacitively graded ac distribution, where the maximum stress is found close to the conductor screen and gradually decreases towards the insulation screen. Once the cable is loaded, a temperature difference develops across the insulation and the field inversion occurs with the maximum stress moving to the insulation screen.

Phenomena 2 and 3 are commonly linked together under HVDC cable operations. The electrode charge injection only occurs when a certain voltage level across the insulation is reached, which is called the space charge threshold characteristic [67]. However, this voltage threshold level is lower than most HVDC operating voltages and the injected charges will subsequently travel towards the middle of insulation. Simultaneously, pre-existing residual charges within the insulation become polarized under the applied voltage and start to travel towards the electrode with the opposite polarity. Over the whole process, these travelling charges are likely to become trapped on interfaces between inhomogeneous dielectrics or between paper layers. As the charges are trapped locally, this space charge type is named the microscopic space charge. A typical effect of microscopic space charge accumulation is a locally modified electric field (from experimental tests), for example as shown in Figure 2.4.

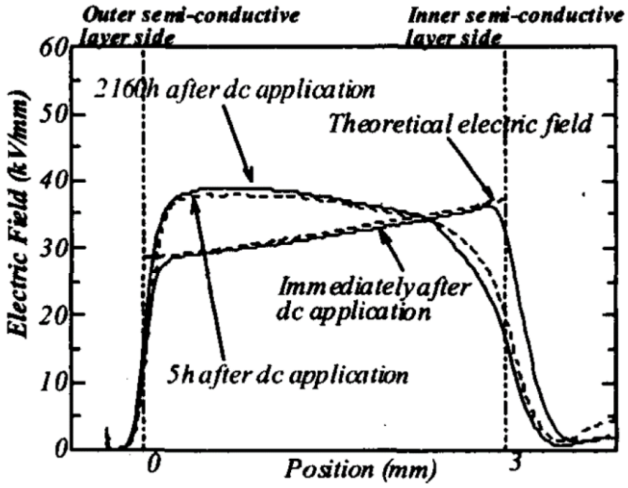

Figure 2.4: Electric stress distribution in DC XLPE cable [37]

Although the macroscopic space charge effect has already been presented by the empirical dielectric electrical conductivity equation, the interfacial microscopic space charge accumulation is hard to estimate analytically and it is heavily material dependent. Except for lab experiments like Pulsed Electroacoustic (PEA) tests, applying the Maxwell-Wagner (MW) polarization within FEA modelling may provide a preliminary estimation [68]. Compared to the classical Maxwell polarization which considers the permittivity discontinuity only, the Maxwell-Wagner polarization also includes the conductivity discontinuity effect in the interfacial space charge calculation [69]. Once both macroscopic and microscopic space charges are present, the total field strength, E_{total}, is calculated under the superposition principle.

$$E_{total}(r) = E_L(r) + E_{mac}(r) + E_{mic}(r) \tag{2.8}$$

Where; E_L is the geometrical Laplace field strength [kV.mm^{-1}], E_{mac} the macroscopic space charge field strength [kV.mm^{-1}], and E_{mic} is the microscopic space charge field strength [kV.mm^{-1}]. Note that the microscopic space charge field, E_{mic}, can be calculated through the Poisson's equation, and both the Laplace field, E_L, and the macroscopic space charge field, E_{mac}, are further discussed in Section 2.3.3. Therefore, the theoretical work developed in this thesis only deal with the first two types of electric field (i.e. E_L and E_{mac}). The E_{mic} analysis requires experimental microscopic space charge measurements and, according to (2.8), can be added in future work.

2.3.2 Empirical electrical conductivity equation of dielectrics

As the empirical equation describes the cable dielectric electrical conductivity as a function of local temperature and electrical stress, a much more complicated thermal-electric field distribution results, which constitutes a fundamental difference in the electrical design between ac and dc cables. Good understanding of the empirical electrical conductivity equation is the root of developing the electrical stress-limited rating method for HVDC cables.

Back in the early 1950s, the dielectric electrical conductivity was only represented as a function of local temperature, based on experimental observations. Whitehead in 1951 [70] studied its dependence on local field and expressed this relation implicitly through its temperature dependence. Since then, the empirical electrical conductivity equation, with explicit field dependence included, has been widely observed and verified in experiments [71] [72]. Generally speaking, the temperature dependence of the electrical conductivity mainly accounts for the field inversion, while the field dependence tries to level the field distribution by minimising the stress difference between the conductor screen and insulation screen. Especially under high field strengths, the field dependence cannot be ignored [62], and the empirical equation takes the following form.

$$\sigma = \sigma_0 e^{\alpha\theta_r} e^{\gamma E_r} \tag{2.9}$$

Where; σ is electrical conductivity at radius r [S.m^{-1}], σ_0 the reference electrical conductivity at 0 ℃ and 0 kV.mm^{-1} [S.m^{-1}], α is the temperature dependency coefficient [℃$^{-1}$], γ is the field dependency coefficient [mm.kV^{-1}], E_r the local field strength at radius r [kV.mm^{-1}], and θ_r is the local temperature at radius r [°C]. Typical values of σ_0, α and γ for mass impregnated paper insulation are shown in Table 2.1 below.

Table 2.1: Summary of the empirical electrical conductivity equation coefficients

	BICC [22]	**Cigré** [47]	**Eoll** [63]	**Jeroense** [62]
σ_0 [S.m^{-1}]	-	0.57×10^{-16}	0.5×10^{-15}	1×10^{-16}
α [°C^{-1}]	0.1	0.1	0.088	0.1
γ [mm.kV^{-1}]	0.03	0.033	0.03	0.03

Although (2.9) is mainly derived through fitting curves to experimental data, an ionic conduction mechanism in the MI paper insulation was suggested by Jeroense, after a close comparison between the empirical equation and the hopping transportation mechanism [73]. The base of the ionic conduction is the movement of ions through ionic crystals, which has been used to explain the interactions between the solid and the ions of the liquid in impregnated paper. According to [74], liquid pockets within the dielectric paper pores contain ions of both polarities, but with one polarity dominant. As a result, the net ions absorbed by the paper do not move freely but are fixed by the cellulose; the oil phase along the pore of the impregnated paper becomes the main path for charge conduction, where travelling ions are likely to suffer from the electrostatic repulsion forces. This obstacle can be modelled as a potential barrier in the hopping mechanism. In [62], equations of both the hopping mechanism and the Poole-Frenkel mechanism have been closely compared to the electrical conductivity empirical equation. Results show that the hopping mechanism gives a much closer solution for an electric field range from 1kV.mm^{-1} to 80kV.mm^{-1} and a temperature range from 0 °C to 80 °C. Therefore, Jeroense suggested that the ionic conduction can be a probable physical explanation of the empirical equation for the MI paper insulation.

Theoretically speaking, with the application of (2.9), the dielectric leakage current heat loss is included. By considering such loss in different ways, interactive thermal breakdown and intrinsic thermal breakdown are identified separately. On one hand, if the heat loss of the leakage current is ignored by comparing to the much larger conductor joule loss, the general interactive thermal breakdown occurs when the system fails to sustain a thermal equilibrium between the losses generated within the cable and the amount dissipated into the environment. On the other hand, when the leakage current heat loss is included within high voltage and temperature applications, the intrinsic thermal breakdown can occur before an interactive breakdown. A simple explanation is that when the heat loss, due to the leakage current, reaches a certain level, it heats up the insulation which in turn results in a higher local electrical conductivity. As the higher conductivity means a higher leakage current and heat losses, a positive thermal feedback loop exists until a breakdown occurs.

The concept of intrinsic thermal breakdown was initially proposed by Eoll through solving equations for the dielectric electrical stress distribution, with leakage current heat losses included [63]. The finding is purely based on the mathematical consideration of the number of available solutions. In Eoll's work, the sheath temperature is set as a constant with varying voltages across the insulation. It is observed that when the applied voltage is small, two stress distribution solutions with physical meaning can be found and usually the smaller one leads to a correct field distribution. As the voltage increases, the two solutions start to converge and become the same value at a certain voltage. Above this voltage threshold, no available solutions exist (i.e. leakage current goes to infinity). As this type of thermal runaway is purely derived mathematically, it is named the intrinsic thermal breakdown.

Recent research [75] on the intrinsic thermal breakdown suggested that the applied voltage across the insulation is the product of dielectric leakage current and its non-linear equivalent resistance. For a certain critical value of leakage current, the voltage attains its maximum. Above this voltage, the decrement in resistance is much more rapid than the increment in leakage current, which finally leads to a voltage collapse. An application of a voltage higher than this critical voltage would result in thermal intrinsic breakdown and for voltages less than this, there are two solutions: a stable one and an unstable one. A brief comparison between the interactive thermal breakdown and intrinsic thermal breakdown is summarized in Table 2.2.

Table 2.2: Comparison between interactive and intrinsic thermal breakdown

	Intrinsic thermal breakdown	**Interactive thermal breakdown**
Cause	Local stress and temperature dependence of the dielectric electrical conductivity (failure of Ohm's law in dielectrics)	Failure of thermal equilibrium with surrounding (assuming constant heat transfer rate of the environment)
Affecting parameter	Internal thermal resistance of the insulation (constant sheath temperature)	Heat transfer property of the sheath and the surrounding thermal resistivity
Occurrence	If the insulation electrical conductivity is a function of temperature only, the intrinsic breakdown may not occur [75]	Occurs in any circumstances once the thermal limit is reached
Mathematical explanation	1. For voltages less than the intrinsic threshold, both stable and unstable solutions exist at two different value of leakage currents 2. For voltages higher than the threshold, no solution exists	1. For voltage less than the interactive threshold, both stable and unstable solutions exist at two different values of sheath temperatures 2. For voltage higher than the threshold, no solution exists

2.3.3 Calculation of dielectric electric field

Under ac operations, the electric field distribution within the cable insulation is capacitively graded and determined by the geometry, the applied voltage, and the dielectric permittivity (constant under normal operating conditions). In general, the highest field is found near the conductor screen and it drops gradually towards the insulation screen. Figure 2.5 below shows the insulation cross section.

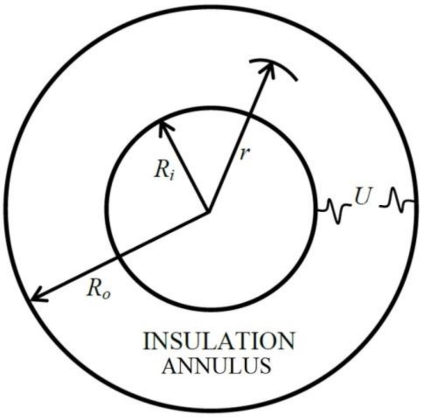

Figure 2.5: Cable insulation cross section

In Figure 2.5, R_i denotes the inner radius of the annulus [mm] and R_o is the outer annulus radius [mm]. Let ρ_{surf} be the conductor surface charge density [C.mm^{-2}] and U the voltage across the insulation [kV], then at the distance r from the cable centre [mm], Gauss Law is applied as:

$$Q = (2\pi R_i)\rho_{surf} = (2\pi R_i)\varepsilon_{ins}E_r \tag{2.10}$$

Where; ε_{ins} is the insulation permittivity [F.m^{-1}] and Q the total charge on the conductor surface [C]. As the field stress is the gradient of electric potential, the ac voltage U can be expressed as follows by assuming zero potential at R_o.

$$U = -\int_{R_o}^{R_i} E_r dr = \int_{R_i}^{R_o} \frac{Q}{2\pi r\varepsilon_{ins}} dr = \frac{Q}{2\pi\varepsilon_{ins}} \ln\left(\frac{R_o}{R_i}\right) \tag{2.11}$$

$$E_r = \frac{Q}{2\pi r\varepsilon_{ins}} = \frac{U}{r\ln\left(\frac{R_o}{R_i}\right)} \tag{2.12}$$

From (2.12), it can be seen that the local stress E_r is inversely proportional to the distance r, which leads to a stress drop from the cable conductor to sheath.

Under dc operation, the dielectric electric field distribution is much more complicated due to the temperature-field-dependent electrical conductivity and possible space charge accumulations. Depending on whether the dielectric leakage current is included, two types of calculations have been previously developed.

a. Field calculation excluding leakage current loss

Based on the fact that the leakage current loss within HVDC cables is generally very small, a simplified stress distribution equation is initially presented by assuming zero heat losses from the insulation. From various physical bases, two types of calculations are well-recognized.

The first calculation is mainly derived from fundamental heat transfer equations and was proposed by Eoll [63], for the stress distribution within impregnated paper insulation under steady state analysis. The empirical equation (2.9) is initially expressed in terms of electric resistivity ρ_r as:

$$\rho_r = \rho_0 \, e^{-\alpha\theta_r} \, e^{-\gamma E_r} \tag{2.13}$$

Where; ρ_0 is the reference electrical resistivity at 0 ℃ and 0 kV.mm^{-1} [Ω.m^{-1}].Through Ohm's law, the electrical stress E_r at radius r is related to ρ_r by:

$$E_r = \frac{i\rho_r}{2\pi r} \tag{2.14}$$

Where; i is the leakage current [A]. Assuming a constant sheath temperature, θ_s, allows the temperature at any point with distance r from the cable centre to be calculated by:

$$\theta_r = \theta_s + \frac{W_c}{2\pi\lambda} \ln\left(\frac{R_o}{r}\right) \tag{2.15}$$

Where; λ is the dielectric thermal conductivity [W.K^{-1}.m^{-1}] and W_c is the conductor joule loss [W.m^{-1}]. Substituting (2.13) and (2.15) into (2.14), the stress distribution can be derived as:

$$E_r = \frac{i\rho_0}{2\pi R_o}\left(\frac{r}{R_o}\right)^{\beta-1} e^{-\alpha\theta_s} e^{-\gamma E_r} \tag{2.16}$$

$$\beta = \frac{\alpha W_c}{2\pi\lambda} \tag{2.17}$$

According to [76], the following simplification for the exponential term in (2.16) is adopted for an analytical approximation (the error introduced by this simplification is discussed in Section 4.1).

$$e^{-\gamma E_r} \simeq (E_r/E_0)^{-\tau} \tag{2.18}$$

$$\tau = \frac{\gamma U}{R_o - R_i} \tag{2.19}$$

$$E_0 = \frac{U}{e(R_o - R_i)} \tag{2.20}$$

By applying (2.18), (2.16) becomes:

$$E_r = E_0 \left(\frac{i\rho_0}{2\pi R_o E_0}\right)^{\frac{1}{1+\tau}} \left(\frac{r}{R_o}\right)^{\delta-1} e^{-\frac{\alpha\theta_s}{1+\tau}} \tag{2.21}$$

$$\delta = \frac{\beta+\tau}{\tau+1} \tag{2.22}$$

Note that as the integral of E_r across the insulation gives the potential difference, the leakage current i and an analytical solution of E_r can be derived as:

$$i = \frac{2\pi e^{\alpha\theta_s}}{\rho_0 (R_o E_0)^{\tau}} \left[\frac{U\delta}{1-(R_i/R_o)^{\delta}}\right]^{\tau+1} \tag{2.23}$$

$$E_r = \frac{U\delta (r/R_o)^{\delta-1}}{R_o\left[1-(R_i/R_o)^{\delta}\right]} \tag{2.24}$$

The second calculation [73] is also developed for mass impregnated paper insulation, but is largely based on the fundamental electrical circuit theory, which regards the insulation as a bulk resistor. Let R_{eq} be the equivalent radial resistance of the insulation per unit cable length as:

$$R_{eq} = \frac{1}{2\pi}\int_{R_i}^{R_o} \frac{\rho_r}{r}\, dr \tag{2.25}$$

So the equivalent resistance from the centre to radius r is given by:

$$R_r = \frac{1}{2\pi}\int_{R_i}^{r} \frac{\rho_{r'}}{r'}\, dr' \tag{2.26}$$

Where; r' is the radial integration variable (first order); Thus the voltage and stress at radius r, with reference to the outer radius of the insulation (zero potential) becomes:

$$U_r = \left(1 - \frac{R_r}{R_{eq}}\right) U \tag{2.27}$$

$$E_r = \frac{dU_r}{dr} = \frac{U}{R_{eq}} \frac{dR_r}{dr} \tag{2.28}$$

Let θ_r be the local temperature at radius r, which is defined as:

$$\theta_r = \frac{s}{\alpha} \ln\left(\frac{R_o}{r}\right) + \theta_o \tag{2.29}$$

$$s = \frac{\alpha\Delta\theta}{\ln(R_o/R_i)} = \frac{\alpha W_c T_1}{\ln(R_o/R_i)} \tag{2.30}$$

$$\Delta\theta = \theta_i - \theta_o \tag{2.31}$$

Where; θ_i is the temperature at insulation inner radius [℃], and θ_o is the temperature at the insulation outer radius [℃]. Substituting (2.13), (2.25), (2.26), (2.29), (2.30) into (2.28) results in:

$$E_r = \frac{U e^{-s\ln\left(\frac{R_o}{r}\right)} e^{-\gamma E_r} e^{-\alpha\theta_i}}{r\int_{R_i}^{R_o} \left(\frac{1}{r}\right) e^{-s\ln\left(\frac{R_o}{r}\right)} e^{-\gamma E_r} e^{-\alpha\theta_i} dr} \tag{2.32}$$

Recognizing that

$$e^{-s\ln\left(\frac{R_o}{r}\right)} = \left(\frac{r}{R_o}\right)^{s} \tag{2.33}$$

Finally, it follows that

$$E_r = \frac{U r^{s-1} e^{-\gamma E_r}}{\int_{R_i}^{R_o} r^{s-1} e^{-\gamma E_r} dr} \tag{2.34}$$

A comparison between (2.24) and (2.34) implies that although the analytical equation (2.24) can give a solution rapidly, its accuracy may largely depend on the applicability of the approximation (2.18) in practice. Solving (2.34) provides a more accurate dielectric stress distribution, but it can only be solved numerically using a computer based method.

b. Field calculation including leakage current loss

The main purpose of this section is for the completeness of relevant calculation and reference. However, the leakage current contributes only 1% of additional heat losses as shown in Section 3.3. In the case of high field and temperature, the dielectric leakage current has a rapid exponential increase due to (2.9). Therefore the corresponding heat losses cannot be ignored and (2.15) is modified into (2.35) [77]:

$$\theta_r = \theta_s + \frac{1}{2\pi\lambda}\int_r^{R_o}\frac{dr'}{r'}\left[W_c + W_{leakage}(r')\right] \tag{2.35}$$

$$W_{leakage}(r') = i\int_{R_i}^{r'} dr'' E(r'') \tag{2.36}$$

Where; *r ´*and *r ´´*are the first and second radial integration variable respectively. By applying the simplification (2.18), (2.21) becomes:

$$E_r = E_0\left(\frac{i\rho_0}{2\pi R_o E_0}\right)^{\frac{1}{1+\tau}}\left(\frac{r}{R_o}\right)^{\delta-1} e^{-\frac{\alpha i}{2\pi\lambda(\tau+1)}\int_r^{R_o}\frac{dr'}{r'}\int_{R_i}^{r'} dr'' E(r'')}\, e^{-\frac{\alpha\theta_s}{1+\tau}} \tag{2.37}$$

As (2.37) can only be solved numerically, perturbation theory is applied for an analytical approximation. Mathematically, the perturbation theory is applicable if the problem can be formulated by adding a small deviation to the mathematical description of an exactly solvable problem as:

$$A = A_0 + {\varepsilon_s}^1 A_1 + {\varepsilon_s}^2 A_2 + {\varepsilon_s}^3 A_3 + \cdots \tag{2.38}$$

Where; ε_s is a ‘small’ dimensionless deviation, A_0 is the known solution to the exactly solvable initial problem, and A_1, A_2… are the higher-order terms which may be found iteratively. By neglecting the higher order components of (2.38) for small ε_s, an analytical approximation results:

$$A \approx A_0 + {\varepsilon_s}^1 A_1 \tag{2.39}$$

By assuming the leakage current, *i*, should tend to zero and the stress, E_r, should approach some finite non-zero limit as the dielectric resistivity increases without bound, the following equation must hold:

$$\lim_{\rho_r\to\infty} iE_r = 0 \tag{2.40}$$

Therefore (2.37) becomes (2.21) when the local electrical resistivity, ρ_r , goes to infinity. As a result, the solution (2.24) can be chosen to be the exact solution for (2.37) defined as parameter A_0.

Generally, the parameter ρ_r is used as the small deviation ε_s. For mathematical convenience, an artificial ε_s is defined as being both dimensionless and inversely proportional to ρ_r [77].

$$\varepsilon_s = \frac{E_0 R_o \alpha U exp[\alpha\theta_o]}{2\rho_0\lambda(\beta+\tau)}\left[\frac{U\delta}{E_0 R_o(1-q)}\right]^{\tau+1} \tag{2.41}$$

With an artificial parameter I_a is defined as:

$$I_a \equiv \frac{4\pi\lambda(\beta+\tau)}{\alpha U} \tag{2.42}$$

Under such definitions, the product of I_a and ε_s refers to the asymptotic value of the current i (2.23). Therefore, both dielectric stress $g(r, \varepsilon_s)$ and leakage current $i(\varepsilon_s)$ can be presented in perturbation expansions as:

$$E_r = g(r, \varepsilon_s) = \frac{U\delta(r/R_o)^{\delta-1}}{R_o[1-(R_i/R_o)^{\delta}]}\left[1+\varepsilon_s g^{(1)}(r)+\varepsilon_s{}^2 g^{(2)}(r)+\cdots\right] \tag{2.43}$$

$$i(\varepsilon_s) = \varepsilon_s I_a[1+\varepsilon_s i^{(1)}+\varepsilon_s{}^2 i^{(2)}+\cdots] \tag{2.44}$$

Substituting (2.43), (2.44) into (2.21) and matching the coefficients term by term, parameter A_1 can be calculated. A final expression for dielectric stress considering the leakage current heat losses can be derived as:

$$E_r = \frac{\delta U}{(1-b)}\frac{B}{r}\left[1-\frac{\varepsilon_s}{(1-b)}\left(1+3b-2B+2b\ln B+\frac{2b^2\ln b}{1-b}\right)\right] \tag{2.45}$$

$$b = (\frac{R_i}{R_o})^{\delta} \tag{2.46}$$

$$B = (\frac{r}{R_o})^{\delta} \tag{2.47}$$

Note that δ is defined in (2.22).

2.4 High voltage DC cable mechanical design

For high voltage dc cables, the mechanical design becomes extremely important given the tough operating environments. For instance, although submarine cable has a similar structure to land cable (refer to Figure 2.1) at the same voltage level, it requires a specially designed armour layer to provide corrosion protection and extra mechanical endurance against the external hydraulic force. Particularly for submarine applications, the enhanced cable mechanical strength is necessary to survive the regular movements of the seabed and sediment. Being quoted from [22], the two universal types of armour are steel tape armour (STA) and galvanised steel wire (GSW). The later one is usually referred to either single wire armour (SWA) or double wire armour (DWA).

The steel tape armour normally comes with a cushion of bituminised textile materials, which contribute to corrosion protection. Practically, two tapes are applied helically with the first tape having a gap between turns of up to half the width of the tape. Subsequently, the second tape covers the gap and overlaps the edges of the first tape. Therefore, by applying the two tapes from the same taping head of the armouring machine, the lay length of each tape is identical and the tapes are able to register correctly with each other. Although the tapes and the underlying bedding are flooded with bitumen during the application, the tapes are pre-coated by the supplier with a bitumen varnish to prevent rusting during delivery and storage and to ensure that the underside of the tape is always coated.

The steel wire armour consists of a layer of galvanised steel wires applied with a fairly long lay. It is generally more expensive than STA, but has several advantages as:

- Better corrosion protection and longer armour life
- Increased longitudinal reinforcement of the cable
- Avoidance of problems due to armour displacement
- Better compatibility with extruded thermoplastic over-sheath layers

2.4.1 Dielectric cavity creation mechanisms

Internally for MI-type HVDC cables, unexpected dielectric breakdowns during the cable cooling have been widely reported by both manufacturer type tests and practical experience [78]. It is generally accepted that the weakened dielectric strength results from the creation of cavities within the insulation, which is reflected experimentally by an increasing number of partial discharges [79]. To theoretically explain the creation of these dielectric cavities, two mechanisms (named ‘microscopic cavity creation’ and ‘macroscopic cavity creation’ in this thesis) are currently proposed, but based on different assumptions.

The microscopic cavity creation mechanism assumes that dielectric cavities exist even before the cable is loaded. It is believed that the practical impregnation process ceases at a temperature beyond its designed value (e.g. 20 ℃ room temperature). Thus, dielectric cavities can develop when the impregnation tank continues to cool down to room temperature from that point. This is because the existing impregnant begins to thermally contract, but no more extra impregnant can be added into the insulation to compensate. At this stage, the microscopic cavities are assumed uniformly distributed across the insulation. Under loading in service, the cavities close to the conductor will be firstly filled up due to an impregnant thermal expansion under a temperature gradient across the insulation. With increasing temperature, the surplus impregnant starts to ‘push’ cavities outwards, which effectively increases the cavity density near the cable sheath. As long as the cable is fully loaded, these microscopic cavities are mostly fully filled, thus a high dielectric strength remains. However, as the cable cools and the impregnant contracts, numerous cavities reappear close to the insulation-sheath interface, which can potentially cause an electrical breakdown. This mechanism explains, on a microscopic scale, the redistribution of pre-existing dielectric cavities. However, the complicated mechanism is hard to examine through experiments and even advanced numerical models [40] [80] can only reflect the above process in qualitative terms.

The macroscopic cavity creation mechanism assumes that there is a negligible quantity of pre-existing cavities before loading the cable. Therefore in service, all the cable layers will expand radially outwards with increasing temperature. As the metallic sheath does not expand with temperature to the same extent as the interior components (conductor and insulation), the sheath may go through permanent plastic deformation if its yield strength is exceeded. Subsequently on cooling, the sheath cannot return to its original position, while the insulation contracts. As a result, the interior of the sheath is no longer completely filled and cavities occur. Although this mechanism is more simplified than the previous one, it has been successfully observed within belted solid type cables [22]. This mechanism explains, on a macroscopic scale, the cavity creation process and is straight forward to follow. One possible argument is the validation of the initial cavity-free insulation assumption, as information on the impregnation process is commercially sensitive. However, it is clear that all manufacturers aim to eliminate any pre-existing cavities through various techniques, such as refining the impregnation process with a long period of slow cooling, redesigning impregnant waxes with a much improved expansion coefficient-temperature relationship, and applying pressure tapes (0.8 to 1 $MN.m^{-2}$ [78]) to keep a positive pressure within the insulation. Therefore, it is often claimed that the pre-existing cavity creation is prevented after all these measures [22] [81].

Although the two cavity creation mechanisms may have distinct assumptions and explanations, they can be linked together to deliver a correlated thermal-mechanical effect on calculating the MI cable rating. Eliminating pre-existing cavities (impregnation refinement/ pressure tape) does help to reduce the cavity development under cable cooling. However, this approach also effectively reduces the initial ‘free expansion’ allowance for the impregnant, which makes yielding of the sheath more likely to occur. Overall, the microscopic cavity creation specifies a minimum cable rating which prevents a reoccurrence of the pre-existing cavities, and the macroscopic cavity creation specifies a maximum cable rating which prevents a new cavity creation. With a general aim of developing modern cavity-free insulations, the macroscopic cavity creation mechanism will become more dominant and it would be valuable to quantify how many pre-existing cavities are allowed. Therefore, a simple and reliable pressure calculation method is ideal to answer the question above.

To calculate the cable internal pressure as a function of current loading, a coupled physics approach, using a combination of elasticity theory, thermodynamics and electrical circuit theory is required. Table 2.3 below summarises the necessary knowledge required from each.

Table 2.3: Summary of fundamental requirements

Physics	Application
Electrical circuit theory	• Ohmic loss calculation
Thermodynamics	• Temperature distribution for under cylindrical coordinates • Linear/ volumetric thermal expansion
Theory of elasticity	• Plane stress/ strain analysis under cylindrical coordinates

2.4.2 Electrical fundamental and thermodynamics

Within HVDC cables, the main cause of the dielectric thermal expansion is the heat generated by the conductor joule loss, W_c, and the dielectric leakage current loss, $W_{leakage}$. However under normal operating conditions (of thermal and electrical limit), the dielectric leakage current loss is neglected with a value less of than 1% of the joule loss [22]. A simple joule loss calculation found from electrical fundamentals is:

$$W_c = I^2 R_{dc} \tag{2.48}$$

$$R_{dc} = \frac{\rho_{20}}{A}[1 + \alpha_{20}(\theta_c - 20)] \tag{2.49}$$

Where; I is the cable conductor current [A], R_{dc} is the conductor dc resistance [Ω.m^{-1}], ρ_{20} the reference conductor electrical resistivity at 20 ℃ [Ω.m], α_{20} the constant mass temperature coefficient at 20 ℃ [℃$^{-1}$], θ_c the cable conductor temperature [℃], and A is the conductor cross section area [m^2].

Once the heat source is defined in (2.48), the classic 1D thermal network can be established from the conductor towards ambient with series thermal resistances in the middle. Therefore, by modelling the two-dimensional dc cable cross section as concentric annuli, the temperature distribution within each annular layer is:

$$\theta(r) = I^2 R_{dc}\left[\frac{\rho_t}{2\pi}\ln\left(\frac{R_o}{r}\right) + T_{total}\right] + \theta_{amb} \tag{2.50}$$

Where; ρ_t is the general thermal resistivity [K.m.W^{-1}], R_o the outer radius of the annulus [mm], T_{total} the total thermal resistance between annulus outer boundary and ambient [K.W^{-1}], and θ_{amb} is the remote ambient temperature [℃]. Thus by assuming the cable has the same initial temperature as ambient before load is applied, the temperature rise, θ_{rise}, becomes:

$$\theta_{rise}(r) = \theta(r) - \theta_{amb} = I^2 R_{dc}\left[\frac{\rho_t}{2\pi}\ln\left(\frac{r_o}{r}\right) + T_{total}\right] \tag{2.51}$$

For most engineering materials in either solid or liquid state, thermal expansion is the tendency of matter to change in volume in response to a change in temperature, which is formulated as:

$$\Delta L = \alpha_L L \theta_{rise} \tag{2.52}$$

$$\Delta V = \alpha_V V \theta_{rise} \tag{2.53}$$

Where; ΔL and ΔV are the change in length [m] and volume [m^3] due to varying temperature, α_L and α_V the linear and volumetric thermal expansion coefficient [K^{-1}], and L and V are the initial length [m] and volume [m^3] before thermal expansion or contraction.

2.4.3 Theory of elasticity

In the theory of elasticity, plane stress and plane strain are the two distinct fundamental models for two-dimensional plane analyses [82]. However, both models come from the same partial differential equations (PDEs), which describe the mechanical stress relationship on an infinitesimal element, shown in Figure 2.6:

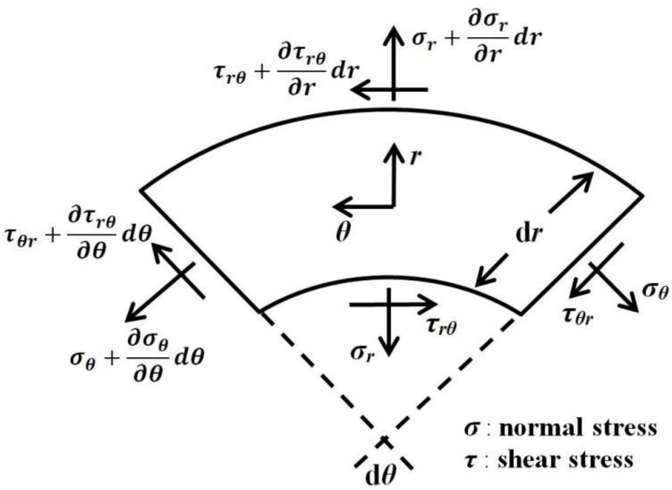

Figure 2.6: Local stress distribution on an infinitesimal element

In Figure 2.6, all the four shear stresses are intrinsically balanced due to annular symmetry. The governing PDE is derived by equating the stress in both radial (r) and circumferential (θ) directions:

$$r\frac{d\sigma_r}{dr} + (\sigma_r - \sigma_\theta) = 0 \tag{2.54}$$

Where; r is the radial coordinate [m], σ_r the radial stress [N.m^{-2}], and σ_θ is the circumferential stress [N.m^{-2}].

Plane stress is defined to be a stress state where the normal stress and associated shear stress (in z direction), directed perpendicular to the x-y plane, are assumed to be zero [82]. This model applies to practical situations where 3D objects have one dimension extremely small compared to the other two or extremely long cables without end constraints (free longitudinal expansion at cable ends). Particularly for an annulus under thermal expansion (with inner/ outer radius R_i/ R_o subject to inner/ outer compressive pressures P_i/ P_o), the resulting radial strain, u, and two principle stresses, σ_r and σ_θ, are formulated by:

$$u(r) = (1+v)\frac{\alpha_L}{r}\int_a^r \theta_{rise}(r) r dr + K_1 r + \frac{K_2}{r} \tag{2.55}$$

$$\sigma_r(r) = \frac{-\alpha_L E_Y}{r^2}\int_a^r \theta_{rise}(r) r dr + \frac{E_Y}{1-v^2}\left[K_1(1+v) - \frac{K_2(1-v)}{r^2}\right] \tag{2.56}$$

$$\sigma_\theta(r) = \frac{\alpha_L E_Y}{r^2}\int_a^r \theta_{rise}(r) r dr - \alpha_L E_Y \theta_{rise}(r) + \frac{E_Y}{1-v^2}\left[K_1(1+v) + \frac{K_2(1-v)}{r^2}\right] \tag{2.57}$$

$$\sigma_z(r) = 0 \tag{2.58}$$

$$\epsilon_z(r) = -\frac{v}{E}[\sigma_\theta(r) + \sigma_r(r)] \tag{2.59}$$

Where; u is the radial displacement [mm], v the material Poisson's ratio, E_Y the material Young's modulus [N.m^{-2}], σ_r the annulus radial stress [N.m^{-2}], σ_θ the annulus circumferential stress [N.m^{-2}], ϵ_z the longitudinal strain, and constant K_1 and K_2 are defined by boundary conditions. For a normal annulus, $a = R_i$ and for solid discs, $a = K_2 = 0$.

Conversely, the plane strain is defined to be another stress state where the normal strain and associated shear strains (in *z* direction), directed perpendicular to the *x-y* plane, are assumed to be zero [82]. This model applies to practical situations where 3D objects have one dimension extremely large compared with the other two, e.g. extremely long cables with constrained ends. Therefore for an annulus under boundary conditions the same as previously, we obtain:

$$u(r) = \frac{(1+v)\alpha_L}{(1-v)r}\int_a^r \theta_{rise}(r)rdr + K_1 r + \frac{K_2}{r} \tag{2.60}$$

$$\sigma_r(r) = \frac{-\alpha_L E_Y}{(1-v)r^2}\int_a^r \theta_{rise}(r)rdr + \frac{E_Y}{1+v}\left[\frac{K_1}{1-2v} - \frac{K_2}{r^2}\right] \tag{2.61}$$

$$\sigma_\theta(r) = \frac{\alpha_L E_Y}{(1-v)r^2}\int_a^r \theta_{rise}(r)rdr - \frac{\alpha_L E_Y \theta_{rise}(r)}{1-v} + \frac{E_Y}{1+v}\left[\frac{K_1}{1-2v} + \frac{K_2}{r^2}\right] \tag{2.62}$$

$$\sigma_z(r) = v[\sigma_r(r) + \sigma_\theta(r)] \tag{2.63}$$

$$\epsilon_z = 0 \tag{2.64}$$

Where; constants K_1 and K_2 are defined by boundary conditions. For a normal annulus, $a = R_i$ and for solid discs, $a = K_2 = 0$. Generally, the radial stress, σ_r, and circumferential stress, σ_θ, are defined, by default, as two principle stresses perpendicular to each other. Note that for real applications, the plane strain assumption is more appropriate and thus adopted in this thesis (see Section 5.3 for details).

2.5 High voltage AC/ DC cable thermal design

In the cable industry, the thermal limit is the most straightforward design criterion which is set to prevent the dielectric material incurring thermal damage (e.g. melting). Normally, the thermal design specifies the maximum conductor temperature depending on the insulation used. The maximum continuous operating temperatures for typical dielectrics are outlined in Table 2.4 below.

Table 2.4: Maximum allowable temperature of several insulations

Cable insulation type	**Maximum continuous operating temperature (℃)**
Low pressure oil filled paper (LPOF)	110
Cross linked polyethylene (XLPE)	90
polypropylene laminated paper (PPLP)	80
Low density polyethylene (LDPE)	70
Mass impregnated paper (MI)	50

2.5.1 Heat sources within high voltage cables

Within the cable system, the three principle heat sources are defined as the joule loss, the dielectric loss and the sheath loss, which result respectively from the conductor electrical resistance, insulation polarization/ leakage current, and the induced sheath current.

Under ac applications, the conductor joule loss, W_c per unit cable length, is calculated using:

$$W_c = I^2 R_{ac} \tag{2.65}$$

$$R_{ac} = R_{dc}[1 + \alpha_{20}(\theta_c - 20)](1 + \gamma_s + \gamma_p) \tag{2.66}$$

Where; α_{20} is the temperature coefficient of conductor electrical resistivity at 20 ℃, θ_c the conductor temperature [℃], γ_s the skin effect factor, and γ_p is the proximity effect factor [31]. The dielectric loss, W_d, is calculated as:

$$W_d = 2\pi f \left(\frac{\varepsilon_r \cdot 10^{-9}}{18 \ln(D_i/D_c)}\right) U_0^2 \tan\delta \tag{2.67}$$

Where; f is the operating voltage frequency [Hz], ε_r the relative permittivity of the insulation material, D_i the external diameter of the insulation [mm], D_c the external diameter of the conductor [mm], $\tan\delta$ the dielectric loss factor, and U_0 is the phase voltage against ground [V]. The sheath loss, W_s per unit cable length, is calculated as a function of joule loss with a constant sheath loss factor λ_1.

$$W_s = \lambda_1 I^2 R_{ac} \tag{2.68}$$

However, only the joule loss is considered under dc applications [31], owing to its overwhelming effect over the other two (a discussion of the dc voltage ripple effect can be found in Chapter 3).

The main difficulty for the cable thermal design does not come from the cable itself, because the cable structure is relatively standard and each component is designed with a stable thermal property under normal operating conditions. Therefore, the main concern lies in the varying thermal ambient, represented by the parameter T_4 in (2.1) or (2.2) on page 17. For buried land cables, the various ground boundary conditions and the partial drying out of backfill are the main issues. For submarine export cables, the thermal effect of protection installations (rock berm/ concrete mattress) becomes extremely important.

2.5.2 Ground boundary condition & backfill partial drying out

At present, IEC60287-1-1 [31] and IEC60287-3-3 [33] are the thermal-limited rating methods widely recognized for high voltage cables and cable crossings respectively. To be mathematically valid, they both assume an isothermal ground surface in order to apply the image theory. Practically, this assumption holds only for deeply buried cables where the presence of the cable, as a heat source, does not cause a significant increase in the local ground surface temperature. However, when cables are buried closed to the ground, the ground surface is more likely to have a peak temperature directly above the cable, gradually reducing away from the cable. Moreover, the ground boundary conditions (e.g. isothermal, convective) can have a big effect on the cable rating, because these various conditions can make the boundary to be either a heat source or a heat sink.

To describe a convective ground boundary, following equation [83] can be adopted to calculate the ground convective heat flux, q, in this thesis.

$$q = h_c(\theta_g - \theta_{amb}) \tag{2.69}$$

Where; h_c is the heat transfer coefficient of convection [W.m^{-2}.K^{-1}], θ_g the ground temperature [°C], and θ_{amb} is the surrounding ambient temperature [°C]. The heat transfer coefficient, h_c, normally is difficult to determine, however, an explicit expression found from experimental data measured in Poona, India [84] has been used:

$$h_c = 6.0 + 4.6w \tag{2.70}$$

Where; w is the ground wind speed [m.s^{-1}]. Note that the use of (2.70) may result in an overestimation of the heat transfer coefficient condition in the UK where the climate is cooler and the difference between ground and air temperature is likely to be lower [85] [86]. However, this issue is left to be addressed in the further work, because this thesis mainly focuses on rating methodology development and demonstration.

In cases where the drying out of backfill occurs, an approximation based on a simple two-zone physical model is recommended in [31], where the zone adjacent to the cable is considered to be dry with one thermal resistivity value whilst the other zone retains the site's wet thermal condition with another value. The zone boundary is assumed to be isothermal at a given critical temperature and can be expressed mathematically as:

$$\rho_t = \rho_{wet} + H(\Theta)(\rho_{dry} - \rho_{wet}) \tag{2.71}$$

with $\Theta = \theta_{local} - \theta_{critical}$ and the Heaviside function $H(\Theta)$ is defined as:

$$H(\Theta) = \begin{cases} 0, & \Theta < 0 \\ 1, & \Theta \geq 0 \end{cases} \tag{2.72}$$

Where; θ_{local} is the local backfill temperature [°C], $\theta_{critical}$ the critical temperature between wet and dry zones [°C]. Note that as the backfill thermal resistivity is very sensitive to backfill moisture content, (2.71) is considered to be appropriate for those applications where backfill behaviour is considered in simple terms only. For a more rigorous backfill model, accounting for moisture migration mechanisms, see [87]. As [87] focuses on environmental modelling through complex nonlinear coupling, it is very computationally consuming and thus out of the scope of this work.

2.5.3 Thermal-limited rating of cable crossings

IEC60287-3-3 [33] is the only method for rating cable crossings, but it may not satisfy particular accuracy requirements or may lose its applicability under complex installation environments. Theoretically, it adopts a simple 1D thermal network representation for radial heat transfer within the cable cross section and applies partial differential equations to describe longitudinal heat transfer. To account for thermal interference between two cable circuits, the simple principle of superposition is used.

The main concept in the IEC60287-3-3 is to calculate the de-rating factor of one cable caused by crossing another, which is modelled as an external heat source. The de-rating factor is defined as:

$$DF = \sqrt{1 - \frac{\Delta\theta(0)}{\Delta\theta_{max} - \Delta\theta_d}} \tag{2.73}$$

Where; $\Delta\theta(0)$ is the conductor temperature rise at the crossing point due to the crossing heat source [℃], $\Delta\theta_{max}$ is the maximum permissible conductor temperature rise above ambient [℃], and $\Delta\theta_d$ is the conductor temperature rise due to the dielectric loss [℃].

To calculate the temperature rise of the rated cable due to other crossing cables (modelled as independent heat sources), superposition is applied based on Kennelly's principle [88]. Equations (2.74) to (2.76) are repeatedly used in an iterative procedure:

$$T_{mh} = \frac{\rho_{bf}(e^{y\Delta z} - 1)}{4\pi} \sum_{n=1}^{k} e^{-ny\Delta z} \ln\left\{\frac{(L_r + L_h)^2 + [(z_r - z_h + n\Delta z)\sin\beta_h]^2}{(L_r - L_h)^2 + [(z_r - z_h + n\Delta z)\sin\beta_h]^2}\right\} \tag{2.74}$$

$$\Delta\theta(0) = \sum_{h=1}^{k} T_{mh} W_h \tag{2.75}$$

Where; T_{mh} is the mutual thermal resistance between the rated cable and heat source [K.W^{-1}], ρ_{bf} the backfill thermal resistivity [K.m.W^{-1}], y the attenuation factor as a function of $\Delta\theta(0)$ defined in [33], β_h the crossing angle between the heat source and rated cable [°], L_r the laying depth of the rated cable [m], L_h the laying depth of the heat source [m], and W_h is the heat generated by external heat source [W.m^{-1}]. Note that the definition of z_r, z_h and Δz are found in Figure 2.7.

However, (2.74) has been slightly amended from IEC60287-3-3 by removing the absolute operator for the distance 'z_r - z_h', because the distance between the moving calculating point and two outer phases heat sources are not always the same, as shown in Figure 2.7.

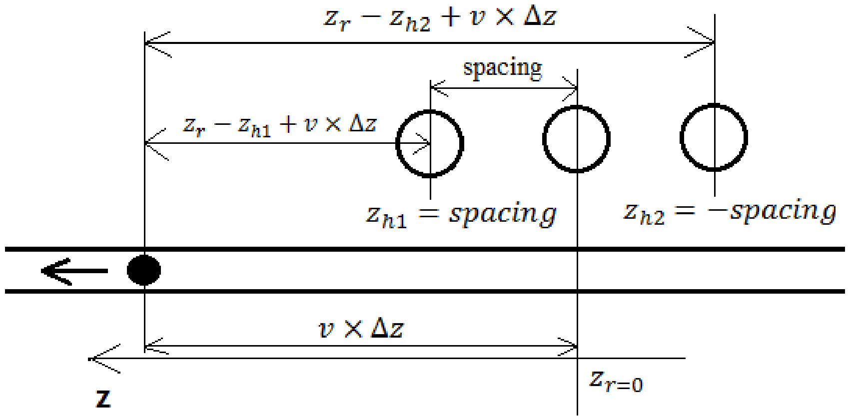

Figure 2.7: Demonstration of equation amendment

As shown in Figure 2.7, $z_r - z_{h2} + v \cdot \Delta z \geq z_r - z_{h1} + v \cdot \Delta z$ always holds in reality when the calculating point travels from the crossing point to the cable end. In IEC60287-3-3, with an absolute operator applied to 'z_r - z_h', these two distances become equal, which is incorrect. However, this issue does not affect the calculation for the crossing with two single cables, as $z_r - z_h = 0$ [89].

To start the iteration procedure, a first estimation of $\Delta\theta(0)$ is given by (2.76), which assumes that the external heat source is parallel to the rated cable with crossing angle $\beta_h = 0$.

$$\Delta\theta(0) = \frac{\rho_t}{4\pi}\sum_{h=1}^{k} W_h \ln\left[\frac{(L_r+L_h)^2+(z_r-z_h)^2}{(L_r-L_h)^2+(z_r-z_h)^2}\right] \tag{2.76}$$

Following the initial estimation, an iterative procedure starts with calculating the de-rating factor for the rated cable, assuming that all the other cables are carrying isolated current equal to their maximum rating when operated without a crossing. Then the de-rating factor for one other cable is calculated, assuming that the previous cable is carrying its de-rated current. This is repeated for each cable until the convergence criterion for the de-rating factor is satisfied.

Generally, the use of the superposition principle and Kennelly's principle requires a homogeneous backfill and the isothermal ground boundary condition, which may not be realistic (refer to Section 6.1 for details).

2.6 Submarine cable protection and thermal property

In this sub section, three main submarine cable protections are outlined, and a detailed literature review on thermal conductivity calculations for porous material is presented. This supports the 3D FEA submarine cable crossing modelling and relevant thermal analyses in Chapter 6.

2.6.1 Cable protection measures

When installing submarine cables (either for power transmission or communication purposes), proper mechanical protection is of great importance to guarantee reliable long-term operation. If a high voltage submarine cable system is damaged, the challenge of fault location and repair can lead to many months of downtime [90]. Typical submarine hazards towards cables include:

- Interaction with fishing gear/ recreational vessels/ ship anchors
- Dredging activities/ other dropped objects
- Exposure of the cable due to seabed movement

Generally, the primary protection method for cables in any submarine environment, against any hazard, is to sufficiently bury the cable in the seabed. The only parameter determining the design of the burial protection is the burial depth, where a 'stronger' seabed backfill provides a greater protection than a 'softer' backfill for a cable buried at a similar depth [91]. To provide a guideline for determining a proper burial depth, the concept of a 'Burial Protection Index' (BPI) has been developed based on [92], which considers various backfill characteristics. In 1999, P. Allen [93] gave a further definition of the BPI as follows:

BPI = 1	Depth of burial consistent with protecting a cable from normal fishing gear only. It would be appropriate to water depths greater than say 50 to 100m, where anchoring of ships is unlikely.
BPI = 2	Depth of burial which will give protection from vessels with anchors up to approximately 2 tons. This may be adequate for normal fishing activity, but would not be adequate for larger ships (tankers, large container ships).
BPI = 3	Depth of burial sufficient to protect from anchors of all but the largest ships. Suitable for anchorages with adjustments made to suit known ship/ anchor sizes.

In Figure 2.8 below, a guideline is proposed to be used in the protection design with necessary adjustments for local conditions, the nature of backfill and the burial method (Ploughing/ Jetting/ Mechanical Trenching/ Mass Flow Excavation).

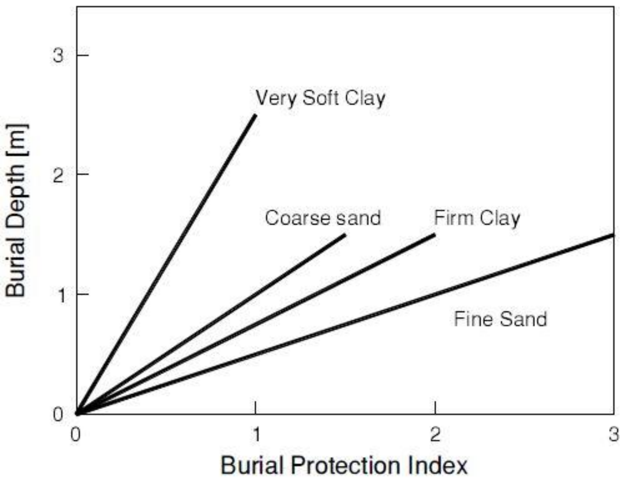

Figure 2.8: Illustration of burial protection index [92]

However, when sufficient burial depth is not achievable, or a burial is impractical at particular locations, remedial cable protection methods will be required [94]. Two typical remedial protection measures are rock placement and the use of a concrete mattress.

Protection by rock placement normally involves an installation of a rock ‘berm’ over the submarine cable which is pre-laid on seabed. A typical rock berm cross section would be a trapezoidal berm of 0.5m - 1.5m height, 5m - 12m base width, and either 1:4 or 1:3 side slope. Figure 2.9 below shows typical rock berm designs for isolated single cable and bundled bipole cable respectively.

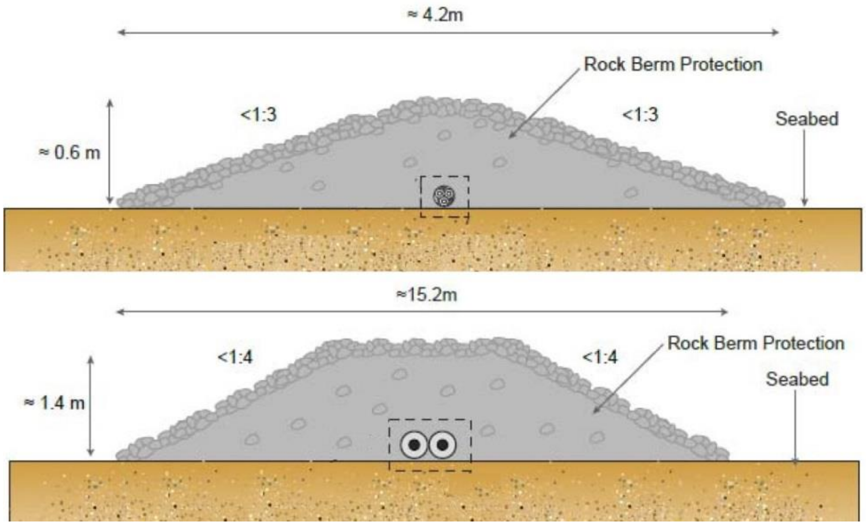

Figure 2.9: Illustration of typical rock berm design [94]

To install these rock berms, either a remotely operated, propelled vehicle (ROV) with fall pipe or a side stone dumping vessel (SSDV) is utilized depending on results from a bathymetric survey, accuracy requirement and rock grading (illustrated in Figure 2.10). The typical protective berm rocks are granite or basalt with sufficient size to resist movement under hydrodynamic loads, but not so large as to make the berm overly permeable. Therefore, appropriate rock size (diameter up to 300mm) can be derived by equating critical shear for limiting equilibrium of rock to bed shear from current and waves [95]. In some cases, a filter layer consisting of finer rocks may be used within large size rock berm design to stabilize the coarser layer just above. Refer to [96] for a detailed sample design calculation.

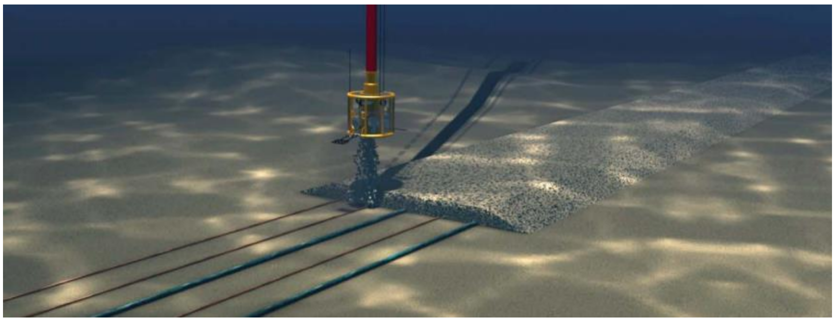

Figure 2.10: 3D illustration of ROV controlled fall-pipe rock dumping [97]

Protection by concrete mattress consists of a number of concrete blocks linked together by flexible ropes. Depending on practical factors (application type, function and environmental conditions), various concrete mattress designs are available including bitumen, flexi-form and pipe-form. In most cases, smoothly tapered edge sections are designed, as they are preferable for a reduced impact upon trawling. For cable protection applications, the concrete mattresses are lowered down over the cables in a predetermined pattern to hold the cables in place and provide protection against fishing gear and vessel anchors. For submarine cable crossing applications, a concrete mattress is the major vertical separator installed between the upper and lower cables. Figure 2.11 shows a sample concrete mattress laid over submarine pipeline/ cable.

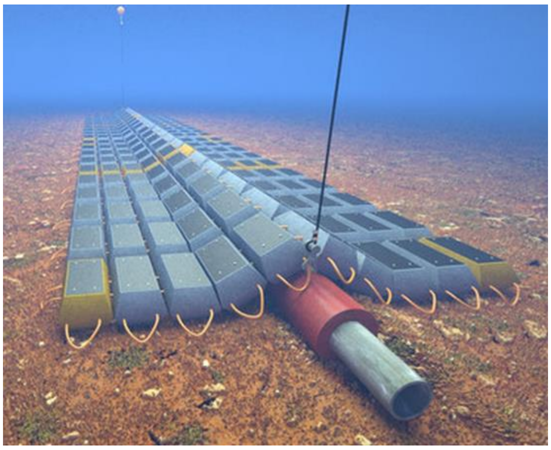

Figure 2.11: 3D illustration of concrete mattress installation [98]

In more demanding situations where strong seabed scour occurs, a flow energy dissipation device (frond mat) is placed on top of the concrete mattress in order to slow down the water velocity and trap mobile sediments, which becomes a new protective covering. According to [99], typical commercial concrete mattress can reach up to 10m x 4m plan area with 150mm to 450mm thickness.

One big challenge is to accurately model the heat transfer mechanism of the rock berm, which has a structure of unconsolidated porous rock, combined with sea water. Theoretically, three heat transfer mechanisms can occur based on local conditions.

- Thermal conduction in the solid phase, liquid phase and across the solid/ liquid interface.
- Thermal convection between the solid phase and the liquid phase.
- Thermal radiation from one internal solid ‘wall’ to another.

As far as practical models are concerned, the thermal conduction inevitably occurs within the rock berm, constituting the fundamental heat dissipation path. Based on the pore-size-related permeability, a free convection can occur, which provides an extra heat transfer up to ten times of that from thermal conduction. As the maximum model temperature is limited to 50℃ (MI-type cable in this thesis), the thermal radiation is weak and neglected [100] [101]. In addition, although water can be transparent to electromagnetic radiation with wavelengths in the visible spectrum (requires high temperature for thermal radiation in visible spectrum), it is opaque to wavelengths outside this band and even visible light is heavily subject to both refraction and attenuation once in sea water [102].

2.6.2 Empirical conductivity calculation without thermal convection

It is important to calculate the effective thermal conductivity of a two-phase system, given the conductivities and volume fractions of each component. Main empirical models found in the literature include those of the harmonic/ arithmetic mean equation, Hashin and Shtrikman boundary, Maxwell, Kunii and Smith, and Revil calculations.

a. Harmonic and Arithmetic Mean

Following the idea in [103], the harmonic and arithmetic mean calculations are the simplest mixing laws which present the upper and lower bounds of the effective conductivity. We denote λ_e as the effective thermal conductivity of the rock/ fluid system [W.m^{-1}.K^{-1}], λ_s the thermal conductivity of solid phase [W.m^{-1}.K^{-1}], λ_f the thermal conductivity of fluid phase [W.m^{-1}.K^{-1}], and ϕ the porosity of the solid phase.

The porosity-weight arithmetic mean is equivalent to two phases being thermally in parallel with respect to the direction of heat flow. It gives the highest possible thermal conductivity for the rock/fluid system among all the mixing laws.

$$\lambda_{max} = \lambda_f \phi + \lambda_s (1 - \phi) \tag{2.77}$$

The harmonic mean is equivalent to two phases being thermally in series with respect to the direction of heat flow, which gives the lowest possible thermal conductivity for the rock/ fluid system among all the mixing laws.

$$\lambda_{min} = \left[\frac{\phi}{\lambda_f} + \frac{1-\phi}{\lambda_s}\right]^{-1} \tag{2.78}$$

Notice that for the upper (2.77) and lower boundaries (2.78), the following condition is satisfied:

$$\left(\frac{d\lambda_e}{d\lambda_s}\right)_{\lambda_s=\lambda_f} = 1 - \phi \tag{2.79}$$

Thus all the effective conductivity equations following the mixing law should satisfy (2.79) [101].

b. Hashin and Shtrikman Boundary

The Hashin and Shtrikman Boundary gives the tightest bounds possible from a range of composite moduli for a two-phase material, assuming a volume fraction of the constituent moduli is pre specified [104]. However, it works better for liquid/ solid systems than gas/ solid systems, and final equations for the maximum and lowest effective conductivities, λ_{max} and λ_{min}, are quoted.

$$\lambda_{max} = \lambda_s + \frac{3\lambda_s \phi (\lambda_f - \lambda_s)}{3\lambda_s + (\lambda_f - \lambda_s)(1-\phi)} \tag{2.80}$$

$$\lambda_{min} = \lambda_f + \frac{3\lambda_f (1-\phi)(\lambda_s - \lambda_f)}{3\lambda_f + \phi(\lambda_s - \lambda_f)} \tag{2.81}$$

The choice of (2.80) or (2.81) depends on the rating strategy being either conservative or optimal, and sometimes an average value can be suitable to start.

c. Maxwell's Model

Maxwell's model was initially applied to calculate the effective electrical conductivity of a random dispersion of spherical inclusions in a continuous medium [105]. When applied to thermal calculations, the equation is derived from calculating the perturbed temperature field due to a large number of small inclusions, and then setting this equal to a single larger inclusion which has the proper ‘effective conductivity’ [106].

$$\lambda_e = \lambda_s \left[\frac{2(1-\phi)\lambda_s + (1+2\phi)\lambda_f}{(2+\phi)\lambda_s + (1-\phi)\lambda_f}\right] \tag{2.82}$$

Note that the theory assumes that the spherical inclusions are far enough apart that they do not mutually interact. In other words, the disturbance to a local thermal field by an inclusion is not ‘seen’ by its neighbouring inclusion.

d. Kunii and Smith Model

The Kunii and Smith model was developed for both loosely-packed and tightly-packed spheres in 1960 [107]. It considers a parallel heat transfer through the fluid in the pore space and the rock solids. Moreover, a series term is added to the solid system to account for the heat transfer between solid grains through a stagnant fluid layer near to the grain contact points. In other words, the model is a combination of the weighted arithmetic mean and harmonic mean equations.

$$\lambda_e = \lambda_f \left\{\phi + \left[(1-\phi)/\left(\varepsilon_{rock} + \tfrac{2}{3}\lambda_f/\lambda_s\right)\right]\right\} \tag{2.83}$$

$$\varepsilon_{rock} = \varepsilon_2 + (\phi - 0.259)(\varepsilon_1 - \varepsilon_2)/0.217 \tag{2.84}$$

Note that ε_{rock} is an empirical parameter depending on the rock porosity. The value of the parameter ε_1 and ε_2 are plotted as functions of λ_s/λ_f, where ε_1 corresponds to a cubic packing of uniform spheres ($\phi = 0.476$) and ε_2 corresponds to a tetrahedral packing of uniform spheres ($\phi = 0.259$). For intermediate porosity values, ε is calculated by linear interpolation between ε_1 and ε_2. For $\phi \leq 0.259$ or $\phi \geq 0.476$, ε_{rock} equals to ε_1 or ε_2 respectively.

e. Revil Model

The Revil thermal conductivity model [108] for unconsolidated porous rocks adopts a differential scheme. Within the model, a grain is firstly assumed to be added into a pure fluid system and the resulting influence of this grain upon the temperature field is analysed. Subsequently, the grain-fluid system is used to coat a second grain and to compute the influence of the newly formed mixture upon the temperature field. This process will keep repeating until a desired porosity value is reached. In summary, the Revil equation is simplified as:

$$\lambda_e = \lambda_f \phi^{\frac{m}{1-m}} \left(\frac{1-\lambda_f/\lambda_s}{1-\lambda_e/\lambda_s}\right)^{\frac{m}{1-m}} \tag{2.85}$$

$$m = 1/(1-N) \tag{2.86}$$

Where; *m* is the ‘cementation exponent’ which is identical to the cementation exponent defined in the electrical conductivity problem from first principles [109] and *N* is the ‘thermal depolarization factor’ which depends on the shape of the solid grain. For spherical grains, $N = 1/3$.

Note that the pore space is assumed to be fully connected and the contiguity between the grains is assumed to be small. Therefore, the theoretical basis of the model stands only for high-porosity unconsolidated sediments with porosity higher than 0.2.

2.6.3 Theoretical conductivity calculation without thermal convection

As most analytical models have integrated correction/ geometric factors based on experimentally measured data, they permit interpolation of data within the range of experimental conditions and even limited extrapolation is possible [100]. However, a more general model based on fundamental properties and basic heat-transfer mechanisms is needed to break the experimental limits.

In 1973, Gomaa [110] developed a theoretical model for thermal conductivity calculation of uniform-diameter spheres in cubic packing configuration, containing wetting (capable of maintaining surface contact with a solid with < 90 ° contact angle) and non-wetting fluids (smaller contact area with > 90 ° contact angle). Based on the fundamental heat transfer principle, unidirectional heat flow through the rock solid, wetting fluid and non-wetting fluid is assumed and the electrical resistance analogy is applied. Moreover, varying porosity is regarded as a function of the flattening level of horizontal contacts between spheres in the cubic packing configuration. Once the rock/ fluid geometry is fixed, the fluid distribution firstly becomes a function of saturation, assuming the non-wetting fluid to be in the centre of the pore space. Secondly, resistances of the three regions: rock solid, rock solid/wetting fluid, and rock solid/ wetting/ non-wetting fluid are modelled separately as resistors in series. Finally, these three regions are combined in parallel to calculate an overall effective thermal conductivity of the unit cell.

In 1976, Ozbek [111] improved Gomaa's model by further dividing the unit cell into five regions. To represent the heat transfer across boundaries, Ozbek considered two semi-infinite phases (liquid and solid) which are at uniform and constant but different temperatures. When the two phases are brought together at time (t = 0s), the temperature-time relation at a prescribed distance from the boundary is given by a set of differential equations. Moreover, if the phase thermal conductivity and diffusivity are given, the temperature at a particular distance from the boundary is a function of contact resistance and time only. From this, Ghaffari [112] developed a 2D heat transfer model for the same cubic pack of flattened spheres used in the previous two models. One difference, however, is that provisions are made so that flattening in the direction perpendicular to heat flow could be different from that parallel to the heat flow direction. This provided an adjustable parameter which made it possible to model more closely the structural characteristics of the rock.

The most recent theoretical model is given by C.T.Hsu who adopts Kunii and Smith's concept of the unit cell and applies it for analysing periodic in-line arrays of square cylinders in either a 2D or 3D configuration. Within each unit cell, only a quarter is analysed (symmetric geometry) which consists of three layers: a rectangular solid layer and two rectangular composite layers with both solid and liquid phases [113].

- **2D solution**

$$\lambda_e = \lambda_f \left[\frac{\gamma_a\gamma_c}{\alpha_{s-f}} + \frac{\gamma_a(1-\gamma_c)}{1+(\alpha_{s-f}-1)\gamma_a} + \frac{1-\gamma_a}{1+(\alpha_{s-f}-1)\gamma_a\gamma_c}\right] \tag{2.87}$$

$$1-\phi = \gamma_a^2 + 2\gamma_a\gamma_c(1-\gamma_a) \tag{2.88}$$

$$\gamma_a = \alpha_{s-f}/L_e \tag{2.89}$$

$$\gamma_c = c_e/\alpha_{s-f} \tag{2.90}$$

- **3D solution**

$$\lambda_e = \lambda_f \left[(1-\gamma_a^2 - 2\gamma_a\gamma_c + 2\gamma_c\gamma_a^2)\frac{\gamma_a^2\gamma_c^2}{\alpha_{s-f}} + \frac{\gamma_a^2-\gamma_a^2\gamma_c^2}{1-\gamma_a+\gamma_a\alpha_{s-f}} + \frac{2(\gamma_a\gamma_c-\gamma_c\gamma_a^2)}{1-\gamma_a\gamma_c+\gamma_a\gamma_c\alpha_{s-f}}\right] \tag{2.91}$$

$$1-\phi = (1-3\gamma_c^2)\gamma_a^3 + 3\gamma_a^2\gamma_c^2 \tag{2.92}$$

$$\gamma_a = \alpha_{s-f}/L_e \tag{2.93}$$

$$\gamma_c = c_e/\alpha_{s-f} \tag{2.94}$$

Where; α_{s-f} is the fluid/ solid thermal conductivity ratio, γ_a, γ_c the geometric constants and a_{s-f}, c_e, L_e are geometric parameter defined in [113].

2.6.4 Effect of natural thermal convection

In most practical cases, free thermal convection is expected to occur within the porous rock berm. However, its effect largely depends on the rock porosity and permeability which normally varies from case to case. Therefore, only empirical calculations are available and widely used in the literature. Within this sub section, several key theories, assumptions and dimensionless parameters are introduced, considering the effect of thermal convection.

a. Darcy's Law

Darcy's Law states that the flow through a porous medium is linearly proportional to the applied pressure gradient and inversely proportional to the viscosity of the fluid [114]. In 1856, Henry Darcy carried out experiments to investigate the hydrology of water flowing through vertical homogeneous sand filters and his finding takes the following empirical form:

$$u_f = -\frac{K_m}{\mu_f}\frac{dp}{dx} \tag{2.95}$$

Where; u_f is the flux rate [m.s^{-1}], K_m the permeability of the medium [m^2], p the pressure defined in Darcy's Law [N.m^{-2}], and μ_f is the dynamic viscosity of the fluid [s.N.m^{-2}]. Note that the permeability K_m is independent of the nature of the fluid but it depends on the geometry of the medium. A list of K_m for normal porous materials can be found in [115].

For all the relevant convection calculations in this thesis, we assume that Darcy's law and the boundary-layer approximations are applicable, and that the gravitational force normal to the heated surface is negligible (flow in Darcy's Law is assumed to be purely driven by pressure gradient and diffusion) [116].

b. Rayleigh Number

In fluid mechanics, the Rayleigh number (Ra) is a dimensionless number associated with buoyancy driven flow (natural convection), which quantifies the convection onset state. Lord Rayleigh states that when the Rayleigh number is below the critical value for a particular fluid, heat transfer is primarily in the form of conduction, while convection becomes dominant if it exceeds the critical value. In this thesis, two complementary models are considered to approximate the rock berm Rayleigh Number.

In Model one, Rayleigh number, Ra_1, is given for thermal convection in a slab of porous of material with constant temperatures at both the upper and lower surfaces horizontally (heat from below) [114]:

$$Ra_1 = \frac{\alpha_V K_m g t_{slab}(\theta_l - \theta_u)}{v_f \beta_m} \tag{2.96}$$

Where; α_V is the volumetric thermal expansion coefficient [K^{-1}], t_{slab} the thickness of the slab [m], g the acceleration of gravity [m.s^{-2}], θ_l the lower surface temperature [℃], θ_u the upper surface temperature [℃], v_f the fluid kinematic viscosity [m^2.s^{-1}], and β_m is the effective diffusivity of the saturated medium [m^2.s^{-1}]. Note that (2.96) assumes that the slab is horizontally unbounded with an isothermal boundary condition on both upper and lower surfaces, so only vertical heat transfer is considered. This model is considered because the cable is located at the bottom of the rock berm and the thick layer above it can be modelled as a flat slab.

In Model two, Rayleigh number, Ra_2, is given for natural convection heat transfer from a horizontal cylinder embedded in a porous medium [116].

$$Ra_2 = \frac{\alpha_V K_m g d(\theta_w - \theta_{amb})}{v_f \beta_m} \tag{2.97}$$

Where; d is the diameter of the cylinder [m], θ_w the cylinder surface temperature [℃], and θ_{amb} is the remote ambient temperature [℃]. Note that (2.97) assumes a heated circular cylinder in an unbounded porous region to satisfy the ‘image theory’. Therefore, this model is applicable because the relatively thermally-resistive concrete mattress beneath the cable is equivalent to a thermal symmetric boundary as it blocks much of the heat transfer downwards (heat flux $q \approx 0$ across the mattress).

c. Nusselt Number

For boundary heat transfer with fluid, the Nusselt number (Nu) is a dimensionless number which represents the ratio of thermal convection to conduction across the boundary. The general form of Nusselt number is:

$$Nu = \frac{Convective\ heat\ transfer}{Conductive\ heat\ transfer} = \frac{h_c L_c}{\lambda_f} \tag{2.98}$$

Where; h_c is the convective heat transfer coefficient, λ_f the fluid thermal conductivity [W.m^{-1}.K^{-1}], and L_c is the characteristic length along the direction of growth (or thickness) of the boundary layer [m]. As the convective heat transfer is geometry related and difficult to specify, the average Nusselt number for free convection is empirically expressed as a power function of the Rayleigh number, $Nu = C(Ra)^n$. For a slab porous medium in Model one, the scale analysis of the convection regime from Bejan [117] indicates that the Nusselt number should increase linearly with Rayleigh number, based on Figure 2.12.

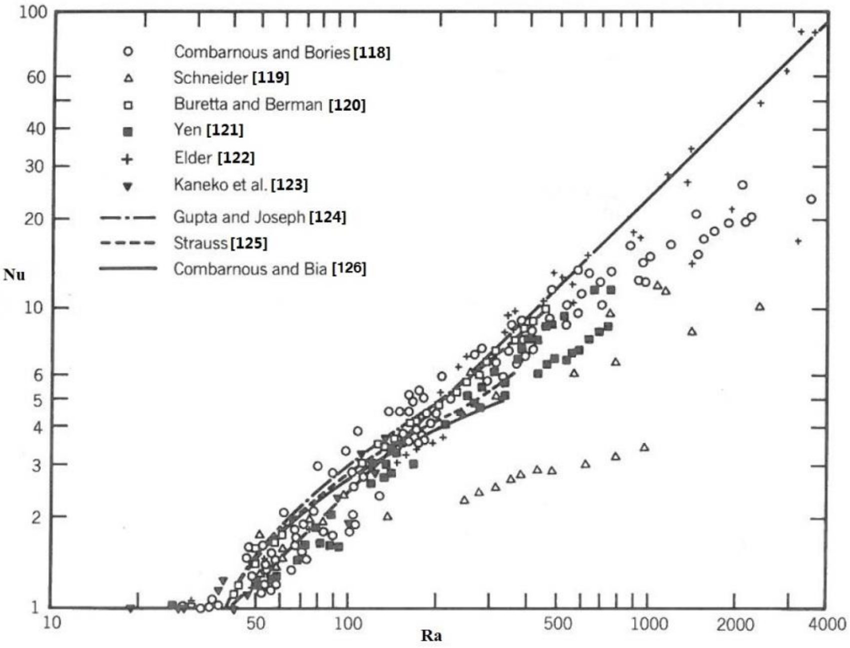

Figure 2.12: Overall heat transfer through porous layers heated from below [127]

Note that as Figure 2.12 is based on practical experiments for a wide range of porous materials, the observed empirical correlations are assumed suitable for the research purpose of this thesis. From Figure 2.12, it is observed that the Nusselt number is roughly proportional to the Rayleigh number once the later one exceeds a threshold of $4\pi^2$. Therefore we have:

$$Nu_1 = \begin{cases} 1 \quad (Ra_1 \leq 4\pi^2) \\ \frac{1}{40} Ra_1 \ (Ra_1 > 4\pi^2) \end{cases} \tag{2.99}$$

For porous medium in Model two, Cheng [128] modified Merkin's analysis [129] and obtained the following expression for the Nusselt number, Nu_2, in the case of a horizontal isothermal circular cylinder:

$$Nu_2 = 0.465 Ra_2^{0.5} \tag{2.100}$$

As (2.100) agrees well with experimental results only for $Ra_2 < 10$ where Darcy's law holds, Ingham [130] ran some numerical calculations and modified (2.100) into:

$$Nu_2 = 0.3995 Ra_2^{0.5} + 0.78 - 1.9 Ra_2^{-0.5} \tag{2.101}$$

Note that all the empirical calculations are tested and compared in Section 3.2.

2.7 Summary

This chapter has presented a broad literature review on high voltage cable technology, covering fundamental cable construction, existing rating methodology, modern design criteria and submarine cable protection. Some key intellectual gaps are pointed out which lead to the development of an improved rating methodology considering electrical/ mechanical constraints under various installation environments. The next chapter summarizes the parameters of two nominal cables and standardizes the FEA modelling procedure used in this thesis. In addition, a short discussion of DC voltage ripples is presented.

Chapter 3

Nominal Cable Design, Installation Environment, and Modelling Technique

In this chapter, two nominal high voltage cable designs are presented with a full list of modelling parameters, which will be subsequently used for all the tests in this thesis. In addition, background to the FEA modelling techniques used in this thesis is provided, including heat source allocation, boundary condition setting and meshing technique. Finally, a short discussion over the thermal effect from dc voltage ripples is presented.

3.1 Two nominal cable designs

Both the two nominal HV cables are amour free and have a similar cross section to that shown in Figure 2.1 on page 13. The HVAC cable with XLPE insulation has parameters summarized in Table 3.1.

Table 3.1: Parameter summary of HVAC XLPE cable

Parameter	Value	Unit
conductor material	copper	-
conductor core number	1	-
conductor outer diameter	34.7	mm
conductor cross section	800	mm^2
conductor electric resistivity	1.7241×10^{-8}	Ω.m
conductor maximum temperature	90	℃
conductor thermal resistivity	0.0026	K.m.W^{-1}
insulation material	XLPE	-
insulation outer diameter	72.8	mm
insulation thermal resistivity	3.5	K.m.W^{-1}
sheath material	lead	-
sheath outer diameter	78.5	mm
sheath electric resistivity	21.4×10^{-8}	Ω.m^{-1}
sheath thermal resistivity	0.0283	K.m.W^{-1}
sheath loss factor	0.011546	-
serving material	PE	-
serving outer diameter	86.8	mm
serving thermal resistivity	3.5	K.m.W^{-1}
nominal operating voltage	132 (AC)	kV

Note that this HVAC land cable design is specially chosen, in Section 6.1 only, to demonstrate the applicability of the developed numerical modelling method for cable crossing rating/ thermal evaluations, through a comparison to the IEC method. For submarine HVDC cable crossings, the IEC calculation is inapplicable due to a failure of the ‘image’ theory (refer to Chapter 6 for details).

The bipole HVDC cable with MI paper insulation has parameters summarized in Table 3.2 below.

Table 3.2: Parameter summary of MI-type HVDC cable

Parameter	**Value**	**Unit**
conductor material	copper	-
conductor core number	1	-
conductor outer diameter	60.5	mm
conductor cross section	2500	mm^2
conductor electric resistivity	1.7241×10^{-8}	Ω.m
conductor thermal resistivity	0.0026	K.m.W^{-1}
conductor maximum temperature	50	℃
conductor volumetric specific heat	3.45×10^{6}	J.m^{-3}.K^{-1}
conductor Young’s modulus	1.25×10^{11}	N.m^{-2}
conductor Poisson’s ratio	0.35	-
conductor linear thermal expansion coefficient	1.7×10^{-5}	℃$^{-1}$
insulation material	MI paper	-
insulation outer diameter	101 / 103	mm
insulation thermal resistivity	6	K.m.W^{-1}
insulation relative permittivity	3.5	-
insulation volumetric specific heat	2×10^{6}	J.m^{-3}.K^{-1}
impregnant volumetric thermal expansion coefficient	6.4×10^{-4}	℃$^{-1}$
Kraft paper volumetric thermal expansion coefficient	1.92×10^{-5}	℃$^{-1}$
sheath material	lead	-
sheath outer diameter	111	mm
sheath thermal resistivity	0.0283	K.m.W^{-1}
sheath volumetric specific heat	1.45×10^{6}	J.m^{-3}.K^{-1}
sheath Young’s modulus	1.6×10^{10}	N.m^{-2}
sheath Poisson’s ratio	0.44	-
sheath yield strength	5.5×10^{6} - 66×10^{6} [131]	N.m^{-2}
sheath linear thermal expansion coefficient	2.93×10^{-5}	℃$^{-1}$
serving material	PE	-
serving outer diameter	120	mm
serving thermal resistivity	3.5	K.m.W^{-1}
Serving volumetric specific heat	2.4×10^{6}	J.m^{-3}.K^{-1}
nominal operating voltage	500 (DC)	kV
external compressive pressure	1×10^{6} [78]	N.m^{-2}

Note that the 1×10^{6} N.m^{-2} compressive pressure is equivalent to the pressure value at 100m water depth and the above HVDC cable design is used for all of the remaining tests in this thesis. Also, the cable insulation layer has two outer diameters (i.e. 101mm/ 103mm) due to various modelling simplifications for the 1mm thin insulation screen layer.

3.2 Installation environment calculation

The cable installation environment affects the rating calculation through the ambient thermal resistance T_4, either explicitly (thermal limited) or implicitly (electrical stress limited/ mechanical pressure-limited). Table 3.3 below summarises the environmental parameters adopted in this thesis, followed by a calculation of equivalent rock berm thermal conductivity.

Table 3.3: Parameter summary of installation environment

Parameter	**Value**	**Unit**
On land		
ambient temperature	12	℃
backfill critical temperature	50	℃
backfill thermal resistivity (wet)	1.2 [86]	$K.m.W^{-1}$
backfill thermal resistivity (dry)	3 [61]	$K.m.W^{-1}$
backfill specific heat capacity*	2050	$J.kg^{-1}.K^{-1}$
cable burial depth (XLPE AC)	0.5 - 2	m
cable burial depth (MI-type DC)	0.5 - 10	m
pole-pole separation (XLPE AC)	140, 310, 450, 590	mm
pole-pole separation (MI-type DC)	5 – 20 or single	m
Submarine		
ambient temperature	4 - 12	℃
backfill thermal resistivity	0.7	$K.m.W^{-1}$
concrete mattress thermal resistivity	1	$K.m.W^{-1}$
pole-pole separation (MI-type DC)	bundled/ isolated	-
cable burial depth (MI-type DC)	500 - 2000	mm

* The backfill specific heat capacity is calculated as the ratio of the thermal conductivity to the product of diffusivity ($4.04\times10^{-7}m^2.s^{-1}$ [88]) and mass density ($1000kg.m^{-3}$).

As explained in Section 2.6, the equivalent thermal conductivity of the porous rock berm is a key parameter to identify, as it may affect the heat dissipation between the cable and ambient (refer to Chapter 6 for details). Therefore, either a pure thermal conduction mechanism or a mixed thermal transfer mechanism (including free convection) is examined.

3.2.1 Rock berm thermal conductivity without free convection

The rock/ fluid properties used to calculate the effective thermal conductivity of the rock berm are summarized in Table 3.4 below.

Table 3.4: Rock/ fluid property summary

Parameter	**Value**	**Unit**
Brine thermal conductivity	0.60 [132]	$W.m^{-1}.K^{-1}$
Basalt thermal conductivity	1.67 [133]	$W.m^{-1}.K^{-1}$
Granite thermal conductivity	2.05 – 3.13 [134]	$W.m^{-1}.K^{-1}$
Average rock thermal conductivity	1.86	$W.m^{-1}.K^{-1}$
Rock berm porosity (loose packed)	0.476	-
Rock berm porosity (compact packed)	0.259	-

The average rock thermal conductivity is calculated based on the worst case scenario and two types of rock packing profiles are shown in Figure 3.1 below.

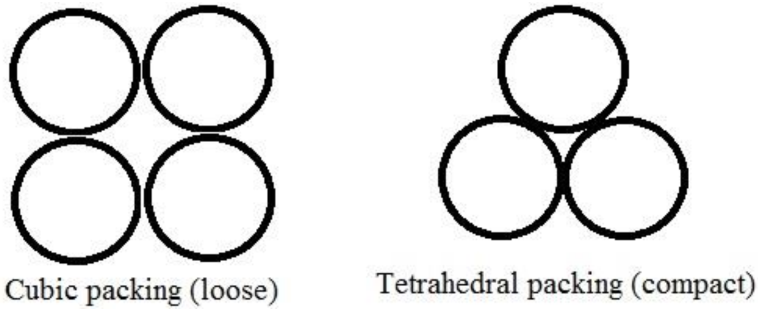

Figure 3.1: Illustration of rock packing profiles

Based on the parameters in Table 3.4, the pure rock berm thermal conductivity (no thermal convection) is calculated through the different methods stated in Section 2.6 and results are compared and summarized in Table 3.5.

Table 3.5: Summary of rock berm thermal conductivity calculation

Method	**Thermal conductivity (W.m^{-1}.K^{-1})**
Harmonic and Arithmetic Mean	$1.20 \le \lambda \le 1.53$ (compact) $0.93 \le \lambda \le 1.26$ (loose)
Hashin and Shtrikman Boundary	$1.39 \le \lambda \le 1.47$ (compact) $1.10 \le \lambda \le 1.18$ (loose)
Maxwell's Model	$\lambda = \begin{cases} 1.47\ (compact) \\ 1.18\ (loose) \end{cases}$
Kunii and Smith's Model	$\lambda = \begin{cases} 1.31\ (compact) \\ 0.99\ (loose) \end{cases}$
Revil's Model	$\lambda = \begin{cases} 1.37\ (compact) \\ 1.12\ (loose) \end{cases}$
C.T.Hsu's Model	$\lambda = \begin{cases} 1.33\ (compact) \\ 1.02\ (loose) \end{cases}$ (2D analysis) $\lambda = \begin{cases} 1.22\ (compact) \\ 1.07\ (loose) \end{cases}$ (3D analysis)

From Table 3.5, it is verified that the Harmonic and Arithmetic Mean gives the highest and lowest possible thermal conductivity for the rock/ fluid system among all the mixing laws, while the Hashin and Shrikman Boundary provides a much tighter region. Thus to include a wide thermal conductivity range for consideration, the effective rock berm thermal conductivity, without considering free convection effects, in the FEA modelling is $1.22 \le \lambda \le 1.47$ for the compact profile and $0.99 \le \lambda \le 1.18$ for the loose profile.

3.2.2 Equivalent rock berm thermal conductivity with free convection

To consider the free convection effect through the Rayleigh number and Nusselt number calculation, supplementary data for the porous medium and saturating brine are summarised in Table 3.6 below:

Table 3.6: Summary of rock berm thermal conductivity calculation

Parameter	Value	Unit
Acceleration of gravity	9.8	$m.s^{-2}$
Average rock berm thickness	1.1	m
Cable overall diameter	0.12	m
Rock permeability*	10^{-8}	m^2
Brine mass density	1025 [135]	$kg.m^{-3}$
Brine specific heat capacity	4020 [132]	$J.kg^{-1}.K^{-1}$
Brine kinematic viscosity	$1.83{\cdot}10^{-6}$ [136]	$m^2.s^{-1}$
Brine thermal expansion coefficient**	$52{\cdot}10^{-6}$ - $166{\cdot}10^{-6}$ [137]	K^{-1}
Brine thermal diffusivity***	$1.46{\cdot}10^{-7}$	$m^2.s^{-1}$
Temperature difference****	12 - 24	℃

* Typical soil intrinsic permeability ranges from 10^{-7} to 10^{-19} m^2 [138]. As the rock berm is assumed unconsolidated, a relatively high permeability within the range is chosen.

** With 35 $g.kg^{-1}$ brine salinity and pressure from 0.1 $MN.m^{-2}$ to 100 $MN.m^{-2}$. An average value of $109{\cdot}10^{-6}$ is adopted in this thesis. Refer to [139] for other situations

*** The Brine thermal diffusivity is calculated as the ratio of thermal conductivity (see Table 3.4) to the volumetric heat capacity (specific heat capacity $\times$ mass density)

**** Temperature difference is calculated based on a 24^0C cable surface temperature ($\theta_c = 50^0$C and an average $I \approx 2500$A for the MI-type cable in Table 3.2) and a 0^0C - 12^0C ambient temperature. An average of 18^0C is adopted in this thesis.

Based on the parameters in Table 3.6, the Rayleigh number, Ra, and Nusselt number, Nu, for the rock berm are calculated through different methods stated in Section 2.6 and results are compared and summarized in Table 3.7.

Table 3.7: Summary of Rayleigh and Nusselt number calculation

Model	Dimensionless parameter	Value
One (slab material, heat from lower surface)	Ra_1 (2.96)	792
	Nu_1 (2.99)	19.8
Two (heat from embedded cylinder)	Ra_2 (2.97)	86
	Nu_2 (2.101)	4.3

According to Table 3.7, thermal convection needs to be considered for the designed rock berm geometry, with Rayleigh number being above the convection onset value of $4\pi^2$ [100]. In comparison, Model two (Ra_2, Nu_2) with horizontal cylinder embedded in porous medium is adopted, as it describes a closer geometric installation to reality. For Model one, an isothermal rock berm base cannot be guaranteed in practice because the cable is a line heat source and cannot uniformly heat up the base. In summary, the equivalent rock berm thermal resistivity under various situations is outlined in Table 3.8.

Table 3.8: Summary of rock berm equivalent thermal conductivity

Packing configuration	**Equivalent thermal conductivity (W.m^{-1}.K^{-1})**	
	without free convection	with free convection
compact	$1.22 \leq \lambda \leq 1.47$	$6.47 \leq \lambda \leq 7.79$
loose	$0.99 \leq \lambda \leq 1.18$	$5.25 \leq \lambda \leq 6.25$

3.3 FEA modelling technique

In this sub section, a standard FEA modelling process used in this thesis is presented, based on the numerical modelling package: COMSOL Multiphysics [140]. Construction of a model includes the following main steps (but not limited to):

Step 1. Physics selection and Geometry building
Step 2. Material specification, Heat source allocation, and Boundary condition
Step 3. Meshing and Solving

3.3.1 Physics selection and Geometry building

As previously explained in Section 2.4, the electrical stress-limited rating analysis requires an interaction between the thermal and electric fields through the dielectric electrical conductivity (2.9) on page 17. Therefore, the FEA model includes two fundamental physical modules: Heat Transfer (*ht*) and Electric Currents (*ec*).

Within the *ht* module, temperature T is the dependent variable with a governing equation as:

$$\rho C_p \frac{\partial T}{\partial t} + \mathbf{u} \cdot \rho_m C_p \nabla T = \nabla \cdot (k \nabla T) + Q_h \tag{3.1}$$

Where; ρ_m is the mass density [kg.m^{-3}], C_p the specific heat capacity [J.kg^{-1}.K^{-1}], **u** the velocity vector of the fluid if included [m.s^{-1}], t the time [s], k the general thermal conductivity [W.m^{-1}.K^{-1}], and Q_h is the rate of heat generation per unit volume [W.m^{-3}]. Under steady state analyses where fluid (causing convection if it moves) is not included, $\partial T/\partial t = 0$ and $\mathbf{u} = 0$.

Within the *ec* module, electric field potential Φ is the dependent variable which is calculated through following governing equations:

$$\nabla \cdot J = Q_j \tag{3.2}$$

$$J = \sigma E + \frac{\partial D}{\partial t} + J_e \tag{3.3}$$

$$E = -\nabla \Phi \tag{3.4}$$

Where; J is the induced electric current density [A.m^{-3}], J_e the externally generated current source [A.m^{-3}], Q_j the rate of charge generation per unit volume [C.m^{-3}], σ the general electrical conductivity [S.m^{-1}]. E the general electric field strength [V.m^{-1}], D the electric flux density [C.m^{-3}], and Φ is the electric field potential [V]. Under a steady state analyses in this study, $\partial D/\partial t = J_e = 0$. Note that the above two physical modules are coupled through the dielectric conductivity calculation (2.9).

In terms of model geometry, cables with specified dimensions (Table 3.1 and Table 3.2) are enclosed by a surrounding backfill box, which represents the ambient environment. Ideally, the overall model size should be as small as possible to save computational time, but still fully represent the physics in reality (e.g thermal transfer mechanism). As an example in the literature [85], Figure 3.2 below shows the geometry layout of a typical 2D slice cable model.

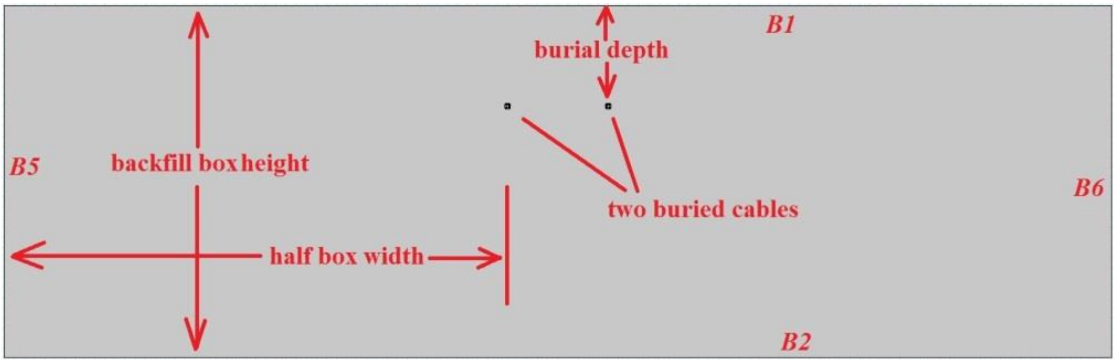

Figure 3.2: Geometric outline of 2D HVDC bipole cable installation

In Figure 3.2, the half box width is supposed to be big enough to assume no heat flux crosses the side boundaries B5 and B6 (at least 10m far away from the cable centre [83]). The backfill box height is at least 7m with an isothermal bottom boundary [141]. However, an improved bottom boundary setting is derived in Section 3.3.2. Note that a specific cable crossing geometry is presented in Chapter 6.

3.3.2 Material specification, Heat source allocation, and Boundary condition

The material specification for the FEA modelling is straightforward with data presented in Table 3.1 and Table 3.2. If partial drying out is under consideration, (2.71) on Page 35 is typed into the backfill thermal resistivity box to reflect this situation. In addition, for a thermal-electric model in Chapter 4, (2.9) is typed into the dielectric electrical conductivity box to represent its dependency on local temperature and electrical field strength, with values taken from Table 2.1 on Page 22.

For the heat source allocation under ac applications, (2.65) and (2.68) in Section 2.5.1 are used to specify the conductor Joule loss and sheath loss. Instead of the analytical calculation of dielectric loss in (2.67), the following continuous function is applied due to the fact that the electric field is stronger closer to the cable core, causing greater dielectric loss and hence more heat generation.

$$q(r) = \frac{\varepsilon_0 \varepsilon_r \omega tan\delta {U_0}^2}{r^2[\ln(r_i) - \ln(r_c)]^2} \tag{3.5}$$

Where; q is the heat flux due to dielectric losses [W.m^{-2}], U_0 is the system phase voltage [V], r is the radius where the function is evaluated [m], r_c is the outer radius of the conductor [m], and r_i is the outer radius of the insulation [m]. A full derivation can be found in [83].

Under dc applications, (2.48) in Section 2.4.2 is used to specify the conductor Joule loss and the following equation is embedded in the FEA package to calculate the dielectric leakage current loss.

$$q = E^2\sigma \tag{3.6}$$

Where; q is the general heat loss due to leakage current losses [W.m^{-3}], σ the dielectric electrical conductivity [S.m^{-1}], and E is the general electric field stress [V.m^{-1}]. Note that by apply (3.**6**) in FEA modelling, the dielectric leakage current is found only contribute 1% additional heat losses. In Figure 3.3 below, the heat source allocation is illustrated.

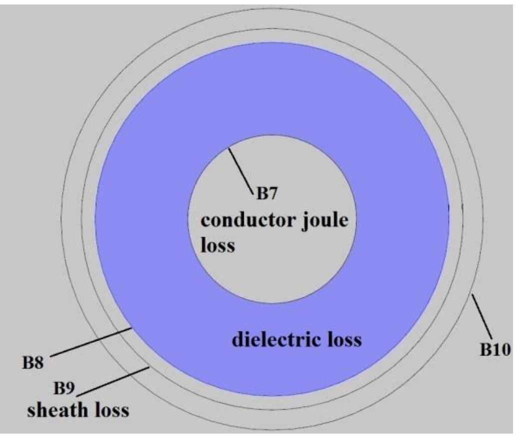

Figure 3.3: Illustration of heat source allocation

In terms of boundary conditions within the cable, B8 and B10 in Figure 3.3 refer to the insulation and serving outer boundaries, with a thermal continuity boundary defined as:

$$-\mathbf{n}_{\mathbf{inner}} \cdot (k\nabla T)_{inner} = \mathbf{n}_{\mathbf{outer}} \cdot (k\nabla T)_{outer} \tag{3.7}$$
$$T_{inner} = T_{outer} \tag{3.8}$$

Where; $\mathbf{n}_{\mathbf{inner}}$ and $\mathbf{n}_{\mathbf{outer}}$ are the normal unit vectors at boundary inner and outer surfaces, and T_{inner} and T_{outer} are the temperature of the boundary inner and outer surfaces [K]. Specially for the thermal-electric modelling, ‘electrical potential’ and ‘ground’ boundaries are defined on B7 and B8 respectively as follows:

$$\Phi = 10^3 U \tag{3.9}$$
$$\Phi = 0 \tag{3.10}$$

Where; Φ is the field potential [V] and U is the nominal operating voltage [kV].

Outside the cable in Figure 3.2, the ground boundary B1 is either isothermal or thermal convection using (2.69). The side boundaries B5 and B6 are thermal insulation specified by the following equation.

$$-n \cdot (-k \nabla T) = 0 \tag{3.11}$$

Where; n is the unit vector normal to the surface, k the general thermal conductivity [W.m^{-1}.K^{-1}], and θ is the general temperature [℃].

For the bottom boundary B2, previous studies [83] have generally adopted a 12 ℃ isothermal condition at 7m depth, which was shown to match well with IEC60287-1-1 [31] in [141]. However, for land cable crossings with a higher total heat generation, the temperature distribution at 7m depth is less likely to be isothermal. This distortion gets stronger with deeper cable burial depth. In order to remove constraints from the arbitrary isothermal bottom boundary, the temperature distribution at 7m depth with the presence of crossing cables is calculated by:

$$T = \theta_{amb} + \sum_{j=1}^{n} \frac{\rho_{bf}}{2\pi} W_{tj} \ln\left(\frac{d_j'}{d_j}\right) \tag{3.12}$$

Where; θ_{amb} is the ambient backfill temperature [℃], W_{tj} the total losses of cable j [W.m^{-1}], ρ_{bf} the backfill thermal resistivity [W.m^{-1}.K^{-1}], d_j the distance from the point under consideration to the actual buried cable j [m], and d'_j is the distance to the image of buried cable j [m]. A full derivation can be found in Appendix One.

The application of (3.12) has been supported by comparison to models either with a much bigger depth (i.e. 25m, 50m) or with an 'infinite elements domain'. The 'infinite elements domain' is used to model unbounded domains through applying a coordinate scaling to a layer of virtual domains with finite size surrounding the physical region of interest. Effectively, this finite virtual domain is stretched out towards infinity [142].

As the crossing maximum temperature difference of the cable conductor at the crossing point between all the three methods (i.e. distributed bottom boundary temperature, 50m-depth modelling, infinite elements domain) is less than 1 ℃, (3.12) is utilized to avoid excessive meshing in the 50m depth modelling and the complex boundary settings for infinite elements domain.

3.3.3 Meshing and Solving

For large scale 3D FEA models, meshing is a key step to guarantee a fast and accurate solution, because each mesh node will be assigned a partial differential equation (PDE) to describe the physics. Higher mesh density is required where the field (thermal/ electrical) gradient is large. Generally, mesh quality is a gross mesh evaluation largely based on its shape and location (e.g. length ratio between the longest and the shorted element edges). In this thesis, triangle (2D) and tetrahedron (3D) meshes are widely used for unstructured grids, with key criterion to be its shape, location and size. For instance, equation below calculates the triangle mesh quality based on its shape (i.e. any distortion to an equilateral shape leads to a mesh quality less than 1) [143]:

$$quality = \frac{4\sqrt{3}A_{tri}}{h_1^2+h_2^2+h_3^2} \tag{3.13}$$

Where; A_{tri} is the triangle area [m^2] and h_1, h_2, h_3 are the side lengths [m]. Figure 3.4 below shows a comparison between coarse and refined meshes, as an example, for 2D slice three-phase cable circuits.

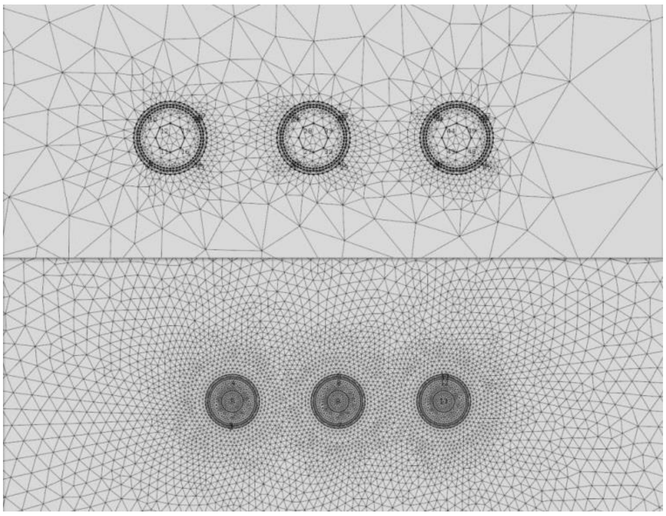

Figure 3.4: Comparison between coarse and refined meshes

In Figure 3.4, two surface meshing strategies are applied and compared. The upper half shows a coarse meshing with average mesh quality of 0.8445, while the lower half shows a refined meshing with mesh quality of 0.9647. However, as the maximum difference in the temperature profile is less than 0.2 ℃ (a safety margin up to 2 ℃ is widely adopted in practice [22]), it implies that an extremely refined mesh (e.g. small size mesh with equilateral shape) for cable conductor and ambient environment is sometimes not necessary. Thus an application of the meshing strategy in upper half can largely save the computation time. Note that a suitable meshing strategy was determined before each test (i.e. refined meshes only applied to thin layers and regions under big field gradient). For instance, the minimum mesh size for the cable sheath and serving layers is 0.002m with 1.1 size growth rate, while all the other components have a minimum mesh size of 0.03m with 1.3 size growth rate (refer to the upper half of Figure 3.4).

As the FEA numerical modelling is widely used in this thesis, it is necessary to explain a bit more about the solving process from a mathematical perspective, for completeness of relevant calculation and reference. As briefly mentioned in Section 2.2, most fundamental physics are mathematically described by partial differential equations (PDEs), with a main variable (e.g. temperature T in thermal analysis or field potential Φ in electrostatic analysis) against location and time. Rather than analytically solve these PDEs for an exact algebraic solution which calculates the variable value at every single point within a continuous application domain, people may only be interested in values at certain key ‘isolated’ points which are adequate to reflect the overall physical profile. Therefore, the concept of discretization is proposed by replacing the continuous information contained in the exact solution of PDEs with discrete values at certain grid points (i.e. mesh nodes in FEA modelling). Thus, discretization equation is defined as an algebraic expression which mathematically links variable values at discrete grid points.

To get discretization equations from PDEs, several mechanisms can be applied such as Taylor-Series Formulation, Control-Volume Formulation, Variation Formulation, and Weighted Residuals Method [144]. However, to simplify the illustration, only the first two are chosen and compared. The following example aims to analyse 1D longitudinal heat conduction under steady state, which has the governing differential equation simplified from (3.1) as:

$$\frac{d}{dx}\left(k\frac{dT}{dx}\right) + Q_h = 0 \tag{3.14}$$

To discretise (3.14) through Taylor-Series Formulation, let's consider three consecutive grid nodes with equal spacing shown in Figure 3.5, and the Taylor-Series expansion around point *n* becomes:

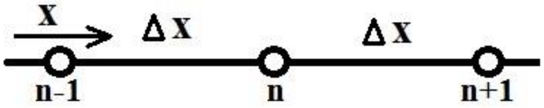

Figure 3.5: Illustration for Taylor-Series Formulation

$$T_{n-1} = T_n + (-\Delta x)\left(\frac{dT}{dx}\right)_n + \frac{1}{2}(-\Delta x)^2\left(\frac{d^2T}{dx^2}\right)_n + \cdots \tag{3.15}$$

$$T_{n+1} = T_n + \Delta x\left(\frac{dT}{dx}\right)_n + \frac{1}{2}(\Delta x)^2\left(\frac{d^2T}{dx^2}\right)_n + \cdots \tag{3.16}$$

When Δx tends to be zero, both (3.15) and (3.16) can be truncated after the third term. Therefore, by adding and subtracting the two equations, following two expressions result:

$$\left(\frac{dT}{dx}\right)_n = \frac{T_{n+1} - T_{n-1}}{2\Delta x} \tag{3.17}$$

$$\left(\frac{d^2T}{dx^2}\right)_n = \frac{T_{n-1} + T_{n+1} - 2T_n}{(\Delta x)^2} \tag{3.18}$$

If the thermal conductivity, *k*, is assumed constant, substituting (3.18) into (3.14) and the discretization equation is derived as:

$$kT_{n-1} - 2kT_n + kT_{n+1} = -(\Delta x)^2 Q_{hn} \tag{3.19}$$

In a short summary, the Taylor-Series Formulation is one of the simplest discretization mechanisms. However, it requires equal spacing between grid nodes which limits its flexibility. In order to truncate higher order elements, this mechanism also requires a small spacing Δx and assumes that the main variable (e.g. temperature *T*) is somewhat like a polynomial in *x*. This is because the Taylor expansion itself is developed in polynomial form and it is better suited to apply to physics with polynomial nature. Otherwise, undesirable formulations may occur (e.g. T varies exponentially with *x*) [144]. Normally, the Taylor-Series Formulation leads to finite difference equations which adopts rectangular meshes and have less meshing freedom for complex geometries.

To discretise (3.14) through Control-Volume Formulation, the differential equation is integrated over each control volume around each grid point and the piecewise profiles expressing the variation of T between the grid points are used to evaluate the required integrals. Let's redraw Figure 3.5 with an integration region around the central point in Figure 3.6.

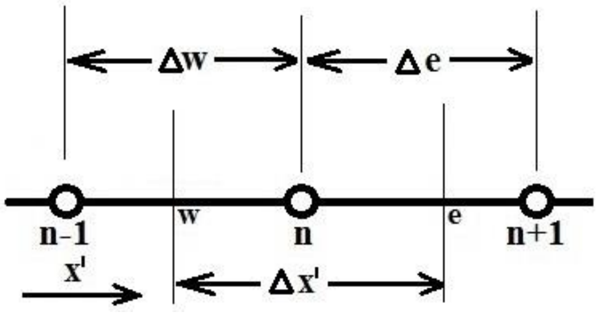

Figure 3.6: Illustration for Control-Volume Formulation

By integrating (3.14) over a control volume (i.e. point w to point e over a length of Δx′) and assuming that temperature T varies linearly with x ′, following expressions are reached:

$$\left(k\frac{dT}{dx}\right)_e - \left(k\frac{dT}{dx}\right)_w + \int_w^e Q_h = 0 \tag{3.20}$$

$$\frac{k_e(T_{n+1}-T_n)}{\Delta e} - \frac{k_w(T_n-T_{n-1})}{\Delta w} + \overline{Q_{hn}}\Delta x' = 0 \tag{3.21}$$

Where; k_e and k_w are the average thermal conductivity over Δe and Δw [W.m^{-1}.K^{-1}], and $\overline{Q_{hn}}$ is the average rate of heat generation around node n over a length of Δx ′[W.m^{-3}]. Rearrange (3.21) and the discretization equation becomes:

$$\left(\frac{k_w}{\Delta w}\right)T_{n-1} - \left(\frac{k_e}{\Delta e} + \frac{k_2}{\Delta w}\right)T_n + \left(\frac{k_e}{\Delta e}\right)T_{n+1} = -\Delta x'\overline{Q_{hn}} \tag{3.22}$$

In (3.22), as the spacings Δe and Δw do not necessarily need to be equal, it gives more freedom in the grid spacing. For example, if the temperature gradient is much high on RHS of node n than its LHS, Δe would be much smaller than Δw. Normally, the Control-Volume Formulation can lead to finite element equations, where triangular meshes become possible for certain complex geometries. Notice that, if $\overline{Q_{hn}}$ = Q_{hn} and $\Delta w = \Delta e$ with sectional middle points at w and e, Δx ′= $\Delta w = \Delta e$ = Δx and (3.22) becomes (3.19). Therefore, for simplicity, (3.19) is used to illustrate the following solving process. Let's first rewrite (3.19) in a general form:

$$BT_{n-1} - MT_n + RT_{n+1} = Q_n \tag{3.23}$$

Where; B, M, R are the variable coefficients for the left, middle, right nodes in Figure 3.5, and Q_n represents the heat generation at the middle node. Theoretically speaking, if the 1D domain (e.g. metal rod) is equally divided into n-1 sections with T_1 and T_n at the start and end nodes, only n-2 independent equations can be derived from (3.23) because T_0 and T_{n+1} do not physically exist. Therefore, to uniquely solve for n discretised temperatures, two more independent equations must be added as boundary conditions. Under a heat conduction problem, boundary temperature and boundary heat flux are normally prescribed, but could not be physically defined at the same node simultaneously. Therefore, let's suppose an entering boundary heat flux inflow, q_{bc}, at the start node and boundary temperature, T_{bc}, at the end node. In Figure 3.6, for the start node *n-1*, assuming point w is in the middle of Δw and $\Delta w = \Delta x$, integrating (3.14) over a half control volume from node *n-1* to point *w* gives:

$$\left(k\frac{dT}{dx}\right)_w - \left(k\frac{dT}{dx}\right)_{n-1} + \int_{n-1}^{w} Q_h = 0 \tag{3.24}$$

By applying Fourier's law [145] to (3.24) and substituting $n = 2$, following equations result:

$$\frac{k_w(T_n - T_{n-1})}{\Delta x} + q_{bc} + \frac{\Delta x}{2} Q_{h1} = 0 \tag{3.25}$$

$$-k_w T_1 + k_w T_2 = -\Delta x\left(q_{bc} + \frac{\Delta x}{2} Q_{h1}\right) \tag{3.26}$$

For the end node, T_n simply equals to T_{bc}. Subsequently in FEA, discretization equations at all grid points are stored in matrix as:

$$\overset{\text{Heat source matrix}}{\begin{bmatrix} -\Delta x\left(q_{bc} + \frac{\Delta x}{2} Q_{h1}\right) \\ Q_2 \\ Q_3 \\ \vdots \\ Q_{n-2} \\ Q_{n-1} \\ T_{bc} \end{bmatrix}} = \overset{\text{Transfer matrix}}{\begin{bmatrix} -k_w & k_w & 0 & 0 & 0 & & 0 & 0 & 0 & 0 \\ 0 & B_2 & M_2 & R_2 & 0 & \cdots & 0 & 0 & 0 & 0 \\ 0 & 0 & B_3 & M_3 & R_3 & & 0 & 0 & 0 & 0 \\ & & \vdots & & & \ddots & & \vdots & & \\ 0 & 0 & 0 & 0 & 0 & & B_{n-2} & M_{n-2} & R_{n-2} & 0 \\ 0 & 0 & 0 & 0 & 0 & \cdots & 0 & B_{n-1} & M_{n-1} & R_{n-1} \\ 0 & 0 & 0 & 0 & 0 & & 0 & 0 & 0 & 1 \end{bmatrix}} \overset{\text{Temperature matrix}}{\begin{bmatrix} T_1 \\ T_2 \\ T_3 \\ \vdots \\ T_{n-2} \\ T_{n-1} \\ T_n \end{bmatrix}} \tag{3.27}$$

Finally, the temperature matrix is solved by right multiplying the heat source matrix with the reciprocal transfer matrix. This approach is called direct solving because, for a linear problem, only one calculation is needed. However, the direct solving can become very memory demanding for large scale non-linear 3D models, as it requires solving equations repeatedly with updated coefficients and all the associated matrixes needs to be fully stored before each repeated calculation. For example, nearly two million matrix entities are required for the 3D cable crossing models.

Apart from the direct solving, iterative solving becomes an alternative which starts from a guessed variable value (i.e. initial condition) and use the discretization equations in some manner to obtain an improved solution. Following successive repetitions of the algorithm, convergence is finally arrived when an approximate solution close enough to the exact one is found within some pre-specified error tolerance or other convergence criterion. The simplest iterative solving is Gauss-Seidel method [144] and a sample application is provided in Section 4.1. Compared to the direct solving, iterative solving requires much less memory because only the solution matrix is stored within iteration. However, a longer calculation time is expected and it can be heavily affected by the initial condition. In this thesis, a direct solver is chosen for a fast computation, as the computer memory is not the primary limit.

3.4 Effect of DC voltage ripple

DC voltage ripple is an unavoidable residual periodic variation in an output dc voltage, which is originally derived from an input ac voltage source. In general, this ripple is due to an incomplete suppression of the alternating waveform within the power supply, and exists within all forms of HVDC converters like line commutated converter (LCC) and voltage source converter (VSC). For the line commutated converter, the ripple is caused by the imperfect rectification of the ac waveform, but is normally filtered on the dc side by a smoothing line reactor and tuned filters [146]. For the voltage source converter, the ripple is caused by the switching of the power-electronic components.

With the dc voltage ripple existing in HVDC cables, there is a concern that this high-frequency ripple may induce current on the cable metal sheath and subsequently limit the cable rating by introducing extra sheath heat loss. In addition, this extra heat loss in sheath can lead to an increased conductor resistance and associated conductor joule loss as well. To remove this concern for this thesis, it is necessary to quantify this induced loss.

In practice, 6 and 12-pulse Bridge rectifier are normally used for high power applications due to a reduced harmonic distortion on both the ac and dc connections [147]. Therefore, the fundamental dc voltage ripple element has a frequency from 300Hz to 600Hz (default 50Hz ac voltage source). Although some high-frequency harmonics may reach frequencies of several kHz, the corresponding ripple magnitude is small. According to [148], ripple factor for a 12-pulse Bridge is around 0.01. In other words, for the nominal HVDC cable in this thesis rated at around 2500A, the effective ripple current is about 25A. Based on a recent publication [149], the loss from induced sheath current is about 3 times as much as the conductor joule loss caused by the effective ripple current. For the MI HVDC cable in this thesis, the 25A effective ripple current gives rise to an extra 0.01W.m^{-1} conductor joule loss ($R_{ac} \approx 1.7\times10^{-5}\Omega\text{.m}^{-1}$). Therefore, an extra sheath loss of around 0.03W.m^{-1} is suggested, which is negligible compared to a much greater steady state conductor loss of around 25W.m^{-1}.

In terms of electrical stress-limited rating calculation, the introduction of sheath loss will lead to a conservative solution. This is because when the extra sheath loss is included, the conductor electrical resistance, R_{dc}, increases due to a higher conductor temperature. Therefore, to keep a constant maximum temperature difference across the insulation ($I_{stress}^2 \times R_{dc} \times T_1 = const$), the stress-limited rating is reduced.

Similarly for the mechanical pressure-limited rating calculation, the introduction of sheath loss also leads to a conservative solution. This is because with the extra sheath loss, a higher temperature rise results and leads to a bigger thermal expansion mismatch between the dielectric layer and the sheath layer. Therefore, higher interfacial pressure develops, which reduces the mechanical pressure-limited rating.

3.5 Summary

This chapter firstly summarizes the parameters of two nominal high voltage cables used in the rest of this thesis. Secondly, the FEA numerical modelling procedure is standardized with emphasis on cable heat sources and boundary conditions. Finally, a short discussion over the DC voltage ripple is presented to support some key assumptions in this thesis. The next chapter will address the electrical stress-limited rating development, which follows a thermal-electric constraint.

Chapter 4

Electrical Stress-limited Rating

As introduced in Section 2.3, the main challenge of the electrical stress-limited rating is to simultaneously determine both the dielectric thermal and electric field distributions, owing to the dielectric electrical conductivity being dependent upon temperature and electrical stress. In Chapter 4, a detailed derivation of the electrical stress-limited rating method is presented, which is subsequently demonstrated through FEA modelling. More importantly, this rating method complements the existing IEC thermal-limited rating to deliver an overall thermal-electric consideration.

4.1 Electric field distribution within cable insulation

Before deriving the electrical stress-limited rating, three dielectric electric field distribution calculations are compared, following distinct mechanisms, namely: analytical approximation (2.24), numerical iteration (2.34) and FEA modelling. As (2.34) is a numerical approach, a solving strategy is firstly proposed.

To solve (2.34), the stress dependence γ is set to zero for the initial estimation of $E_{r(0)}$, because the value of γ is very small (around 0.03, Table 2.1) and it has a smaller effect than the temperature dependence. Subsequently, (2.34) is calculated through Gauss-Seidel iterative method with the term, E_r, in its denominator being approximated by (2.24):

$$E_{r(n+1)} = \frac{U r^{s-1} e^{-\gamma E_{r(n)}}}{\int_{R_i}^{R_o} r^{s-1} e^{-\gamma E_r} dr} = A \cdot r^{s-1} e^{-\gamma E_{r(n)}} \tag{4.1}$$

Until certain convergence requirement of E_r is achieved ($E_{r(n+1)}$ - $E_{r(n)}$ < convergence limit, e.g. 0.1kV.mm^{-1}). Table 4.1 summarizes the parameters of a testing annulus quoted from [73], and

Table **4.2** shows a comparison between various calculation strategies.

Table 4.1: Parameter summary of the testing annulus

Parameter	**Value**	**Unit**
dielectric annulus inner radius	23.2	mm
dielectric annulus outer radius	42.4	mm
stress dependent coefficient (γ)	0.03	mm.kV^{-1}
temperature dependent coefficient (α)	0.1	℃$^{-1}$
reference electrical conductivity	1×10^{-16}	S.m^{-1}
dielectric annulus thermal resistivity	6	K.m.W^{-1}
dielectric annulus relative permittivity	3.5	-
voltage across the annulus	450	kV
annulus temperature drop	5 - 20	℃

Table 4.2: Stress calculation under various strategies

Electric field stress (kV.mm^{-1})			
Dielectric temperature drop (^{0}C)	Eoll’s equation (2.24)	Jero’s equation (4.1)	FEA modelling
at *r* = 23.2mm, close to the conductor screen			
5	24.23	24.23	24.23
10	20.57	20.52	20.51
15	17.35	17.11	17.11
20	14.53	14.02	14.03
at *r* = 32.8mm, middle of the dielectric			
5	23.40	23.40	23.39
10	23.52	23.54	23.54
15	23.48	23.58	23.59
20	23.27	23.52	23.53
at *r* = 42.4mm, close to the dielectric screen			
5	22.81	22.80	22.82
10	25.97	25.94	25.97
15	29.38	29.19	29.14
20	33.00	32.53	32.40

From

Table **4.2**, it can be seen that the analytical calculation (Eoll’s equation) gives a slightly bigger difference compared to the other two. Therefore, Equation (4.1) is chosen as the default numerical calculation for the rest of this thesis, as it has a minimum difference compared to the FEA modelling. Figure 4.1 below plots data from

Table **4.2**.

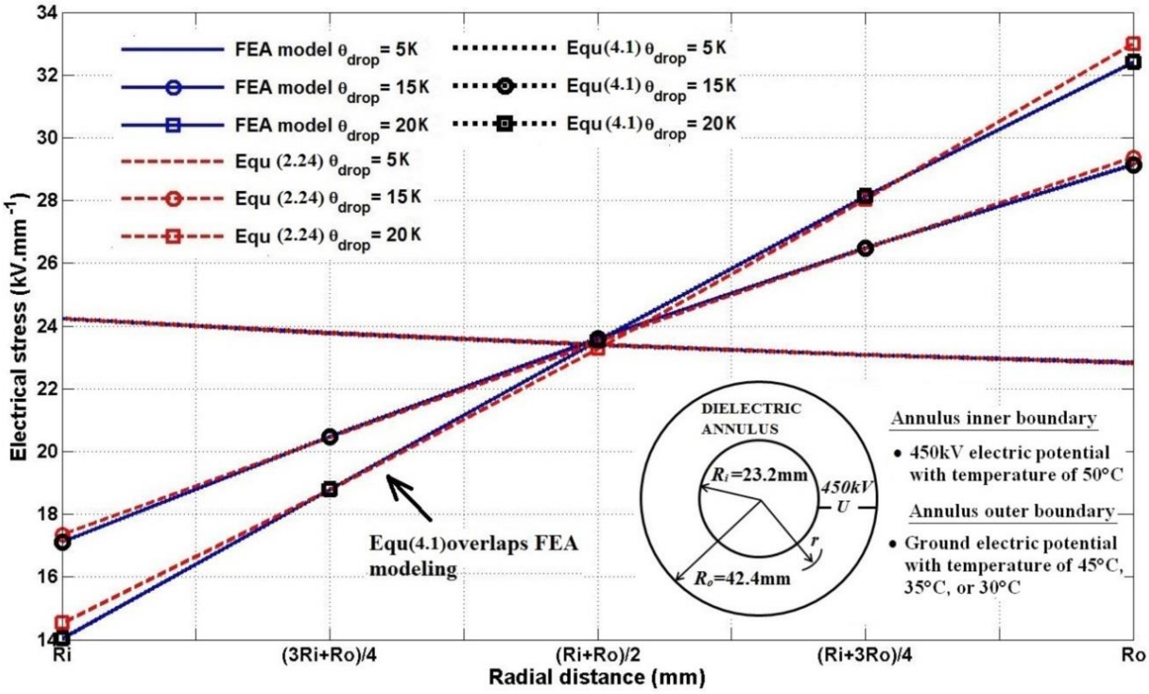

Figure 4.1: Electrical stress distribution under various temperature drops

In Figure 4.1, a point with almost constant electrical stress (less than 0.6% variation, presumably due to numerical errors), regardless of dielectric temperature drop θ_{drop}, is found to be physically located in the middle of the insulation layer. This observation has also been previously mentioned, [73], which considers the macroscopic space charge effect, and will be applied later for deriving an analytical approximation of the electrical stress-limited rating. In addition, it is observed from

Table **4.2** and Figure 4.1 that this constant stress at r = 32.8mm might be approximated by the dielectric mean field stress $U/(R_o\text{-}R_i)$ [150] (Refer to Section 4.3.3 for a detailed test).

4.2 Derivation of electrical stress-limited rating equation

By regarding the annular cable insulation as a bulk resistor, the dielectric electrical stress, E_r, can be calculated according to Ohms law as:

$$E_r = \frac{i\rho_r}{2\pi r} \tag{4.2}$$

$$i = \frac{U}{R_{eq}} \tag{4.3}$$

Where; ρ_r is the dielectric electrical resistivity defined in (2.13), R_{eq} the equivalent electrical resistance of the insulation under a particular loading condition [Ω.m^{-1}], and i is the dielectric leakage current [A]. By substituting (2.13), (4.3) into (4.2):

$$E_r = \frac{U\rho_o\, e^{-\alpha\theta_r}\, e^{-\gamma E_r}}{2\pi r R_{eq}} \tag{4.4}$$

As R_{eq} is constant under a certain loading condition, only two unknowns E_r and θ_r exist. To solve (4.4), at least two reference points satisfying the equation are required as the 'boundary condition'. In general, the maximum long-term design stress value, E_{max}, (taken here as 30kV.mm^{-1} [73]) at the insulation outer radius, R_o, is chosen to be the first reference point. Although the choice of the second reference point is free, it is reasonable to choose the 'constant' middle point (refer to Figure 4.1) at $r = (R_i+R_o)/2$ because the local electrical stress, $E_{(Ro+Ri)/2}$, can be calculated either numerically or analytically from (2.24) or (4.1).

For the purpose of method development, the two reference points are represented in the form of (E_{ref1}, Θ_{ref1}, r_{ref1}), and (E_{ref2}, θ_{ref2}, r_{ref2}), where E_{ref1} and E_{ref2} are the electrical stresses and θ_{ref1} and θ_{ref2} are the temperatures at radius r_{ref1} and r_{ref2}. By substituting the two reference points into (4.4) and rearranging the equation, the following two expressions are derived:

$$\frac{2\pi E_{ref1} r_{ref1}}{U\rho_o e^{-\gamma E_{ref1}}} = \frac{e^{-\alpha\theta_{ref1}}}{R_{eq}} \tag{4.5}$$

$$\frac{2\pi E_{ref2} r_{ref2}}{U\rho_o e^{-\gamma E_{ref2}}} = \frac{e^{-\alpha\theta_{ref2}}}{R_{eq}} \tag{4.6}$$

Dividing (4.5) by (4.6) leads to:

$$\frac{E_{ref1} r_{ref1}}{E_{ref2} r_{ref2}} e^{\gamma(E_{ref1}-E_{ref2})} = e^{\alpha(\theta_{ref2}-\theta_{ref1})} \tag{4.7}$$

As the dielectric leakage current loss is normally neglected for dc cables [31], the temperature difference between the two reference points is the product of the heat flux (resulting from the conductor joule loss W_c) and equivalent thermal resistance between the points. Assume r_{ref1} is larger than r_{ref2}, therefore E_{ref1} is stronger than E_{ref2}, θ_{ref2} is higher than θ_{ref1} under a dc voltage and the following equation holds:

$$\theta_{ref2} - \theta_{ref1} = \frac{W_c \rho_t}{2\pi} ln\left(\frac{r_{ref1}}{r_{ref2}}\right) \tag{4.8}$$

Where; ρ_t is the thermal resistivity of the insulation [K.m.W^{-1}]. By substituting (4.8) into (4.7) and rearranging the equation for W_c, we obtain:

$$W_c = \frac{2\pi}{\alpha \rho_t \, ln\left(\frac{r_{ref1}}{r_{ref2}}\right)} \left[\gamma\left(E_{ref1} - E_{ref2}\right) + ln\left(\frac{E_{ref1} r_{ref1}}{E_{ref2} r_{ref2}}\right)\right] \tag{4.9}$$

Once the conductor joule loss, W_c, is uniquely evaluated through (2.15), the electrical stress-limited current rating, I_{stress}, satisfying (E_{ref1}, r_{ref1}), (E_{ref2}, r_{ref2}) can be calculated through the following equations:

$$I_{stress} = \sqrt{\frac{W_c}{R_{dc}}} \tag{4.10}$$

$$R_{dc} = \frac{\rho_{20}}{A}\left[1 + \alpha_{20}(\theta_c - 293.15)\right] \tag{4.11}$$

$$\theta_c = W_c(T_1 + T_2 + T_3 + T_4) + \theta_{amb} \tag{4.12}$$

Where; ρ_{20} is the conductor electrical resistivity at 20 ℃ [Ω.m], α_{20} the temperature coefficient of electrical resistivity at 20 ℃ [K^{-1}], and A is the cross-sectional area of the cable conductor [m^2].

4.3 Proposed solution techniques and verification

Up to this point, an analytical calculation for the stress-limited rating, I_{stress}, has been proposed. Based on calculating E_{ref2} of the second reference point, a numerical solution and an analytical approximation of I_{stress} can be obtained separately.

4.3.1 Analytical approximation (Method 1)

Referring to

Table **4.2**, Figure 4.1 and [73], it is found that a point with almost constant electrical stress is located in the middle of the insulation, regardless of various loading conditions (including load off). Therefore, by assuming that the constant point is located exactly at $r = (R_i+R_o)/2$, the constant stress can be either analytically calculated through (2.24) referring to the load-off situation ($W_c = 0$) or approximated by the dielectric mean field stress:

$$E_{const} = \frac{U\delta(R_i+R_o)^{\delta-1}}{e^{\delta-1}(R_o^{\delta}-R_i^{\delta})} \approx \frac{U}{R_o-R_i} \tag{4.13}$$

$$\delta = \frac{\gamma U}{\gamma U + R_o - R_i} \tag{4.14}$$

Where; E_{const} is the constant electrical stress at $r = (R_i+R_o)/2$ [kV.mm^{-1}]. Thus by setting this constant point to be the second reference point (E_{ref2}, r_{ref2}), the 'boundary condition' becomes:

$$r_{ref1} = R_o \tag{4.15}$$
$$E_{ref1} = E_{max} \tag{4.16}$$
$$r_{ref2} = (R_i + R_o)/2 \tag{4.17}$$
$$E_{ref2} = E_{const} \tag{4.18}$$

Substituting the two reference points (E_{ref1}, r_{ref1}), (E_{ref2}, r_{ref2}) into (4.9), a final analytical approximation for W_c is derived as:

$$W_c = \frac{2\pi}{\alpha \rho_t \ln\left(\frac{2R_O}{R_O+R_i}\right)} \left[\gamma(E_{max} - E_{const}) + \ln\left(\frac{2E_{max}R_O}{E_{const}(R_i+R_O)}\right)\right] \tag{4.19}$$

Note that the accuracy and applicability of (4.19) largely depends on the validation of the 'constant middle point' assumption, which requires a development of non-destructive experiments on direct dielectric field stress probing. In cases where the assumption doesn't hold, the following numerical solution (Method 2) can still be applied as an alternative. One may argue that the joule loss, W_c, can be directly calculated backwards through (2.24) by substituting (E_{ref1}, r_{ref1}). However this idea is dropped because according to Figure 4.1, the field stress evaluation by (2.24) is much more accurate at r_{ref2} rather than r_{ref1}.

4.3.2 Numerical solution (Method 2)

To obtain a more accurate solution, a numerical iteration is required by combining (4.9) with the electrical stress calculation (2.34). According to (2.34), the local electrical stress, E_r, is defined as a function of dielectric temperature drop, θ_{drop}, only. Thus the electrical stress of the second reference point, E_{ref2}, can be calculated by providing W_c throughout the following equation:

$$\theta_{drop} = \frac{W_c \rho_t}{2\pi} \ln \frac{R_o}{R_i} \tag{4.20}$$

A closed numerical iteration for the calculation of W_c is suggested in the following flow diagram:

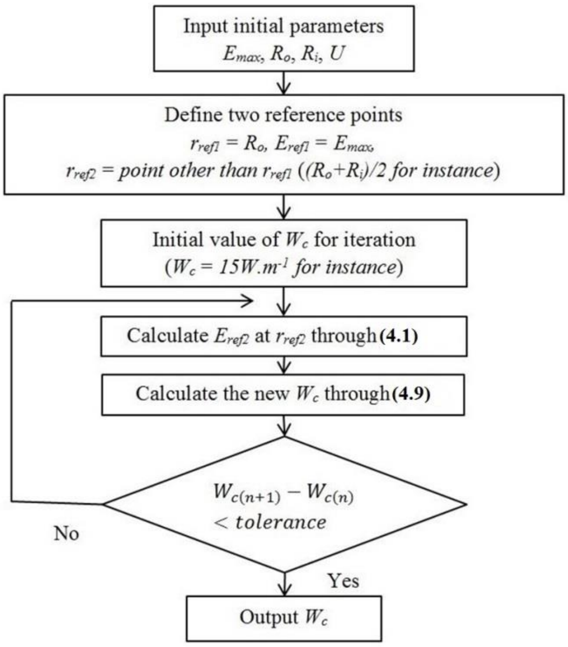

Figure 4.2: Flow diagram for the numerical calculation of joule losses W_c

Once W_c is obtained after the iteration, (4.10) - (4.12) are applied to calculate the electrical stress-limited rating, I_{stress}.

4.3.3 Verification of electrical stress-limited rating calculation

To verify the applicability and accuracy of both the analytical approximation and numerical solution, the HVDC bipole cable circuit from Table 3.2 (D_i = 101mm, γ = 0.03mm.kV^{-1}) is in a horizontally flat formation buried at 10m depth on land (10m pole-pole separation, 12°C ambient temperature) to simulate the real practice. The overall layout and boundary condition settings are shown in Figure 3.2 and Figure 3.3. By setting the maximum dielectric electrical stress, E_{max}, as the controlling parameter (0.1kV.mm^{-1} stress variation margin), results of the corresponding rating calculations are summarized in Table 4.3.

Table 4.3: Electrical stress-limited rating under various E_{max}

Target E_{max} in kV.mm^{-1} at R_o	27	28.5	30	31.5	33
I_{stress} in A (FEA)	1525	1687	1820	1939	2050
I_{stress} in A (Method 1, Eoll's analytical calculation)	1561	1719	1852	1966	2067
I_{stress} in A (Method 1, mean stress approximation)	1532	1692	1829	1947	2049
I_{stress} in A (Method 2)	1521	1681	1817	1936	2044

From Table 4.3, it can be seen that both the Method 1 (analytical) and Method 2 (numerical) show a good agreement with FEA modelling solutions (within 2.5% and lead to less than 2°C temperature variation). As the Method 1 (i.e. mean stress approximation) is analytical and more applicable in practice, it is used to calculate the stress-limited rating for the remainder of this thesis. One practical benefit from applying Method 1 and 2 is that preliminary design calculations could be undertaken quickly for a range of cable configurations.

Figure 4.3 below shows typical dielectric stress evolutions within a thermal loading cycle, carrying Method 1 ratings. It verifies that during a field transition between 'ac type' (cold) and 'dc type' (hot), the dielectric stress maximum moves outwards or inwards between R_i and R_o respectively due to (2.9). As a typical thermal cycle test lasts only 24 hours [151], a further study shows that it may take up to 150 hours before reaching a steady state.

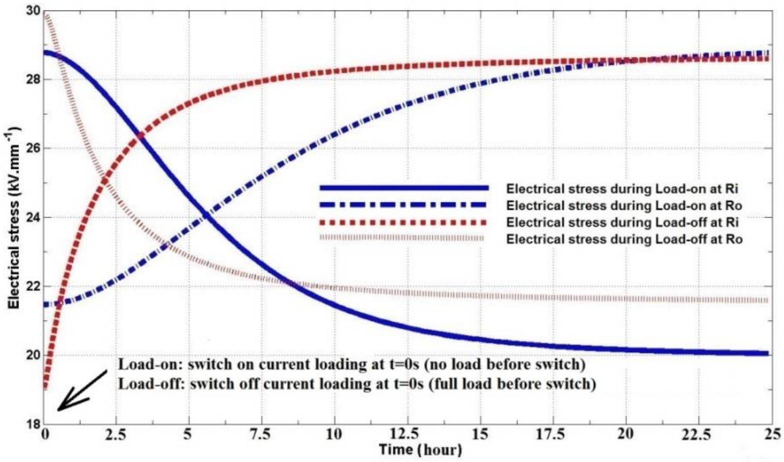

Figure 4.3: Stress evolution during a loading cycle (heating up/ cooling down)

Another key application of Method 1 is to help run sensitivity analysis of the rating to the two conductivity coefficients in (2.9). Understanding the sensitivity of the algorithm to its input parameters is important, as exact values for a given cable design may not be known at early stages of a project. In Table 4.4 below, either the maximum dielectric stress or the rating is constant and the values of the two conductivity coefficients vary between 50% and 150% from the default value.

Table 4.4: Sensitivity analysis of the two conductivity coefficient

	α is the variable (γ = 0.03)					γ is the variable (α = 0.1)				
Variation	50% 0.05	75% 0.075	100% 0.1	125% 0.125	150% 0.15	50% 0.015	75% 0.023	100% 0.03	125% 0.038	150% 0.045
E_{max} = 30kV.mm^{-1} is constant										
Rating (A)	2397	2057	1829	1664	1537	1718	1779	1829	1884	1930
Rating = 1829A is constant										
E_{max} (kV.mm^{-1})	25.7	27.8	30	32.4	34.7	31.6	30.7	30	29.5	29.1

From Table 4.4, it can be seen that the stress-limited rating is more sensitive to the temperature dependency coefficient, α, than the electric field dependency coefficient γ. By varying the value of coefficient α from 50% to 150% of its original value, up to 860A (47%) rating variation is observed, while changing coefficient γ causes a smaller rating variation of 212A (12%). In terms of E_{max}, a similar trend is found, in that the dielectric electrical stress is more sensitive to coefficient α rather than γ. Therefore, it is suggested to design/ choose dielectric materials with low-value α and high-value γ for a better electrical performance.

Table 4.4 also emphasizes the importance of obtaining measured values of α and γ for a given cable system. Although the range tested is relatively large, an error of more than 2% in the rating calculation (as a result of the input data) would not be acceptable, even for an initial scoping study. A method for the experimental determination of parameters α and γ can be found in [152].

4.4 Applications of electrical stress-limited rating

Under practical operations, the current rating requirement must be set to guarantee both the thermal and electrical safety of the cable. Therefore the developed electrical stress-limited rating should be combined with the existing thermal-limited rating (2.2) to provide an overall thermal-electric consideration. For all the tests in this section, both the thermal-limited rating, $I_{thermal}$, and the stress-limited rating, I_{stress}, of the nominal cable are calculated by IEC60287 and Method 1 respectively, with the lower value being named the cable thermal-electric rating I_{TE}. Unless otherwise stated, the thermal and electrical limits are maximum 50^0C conductor temperature and 30kV.mm^{-1} (0.1kV.mm^{-1}stress variation margin) at the outer radius of the insulation. Under such operating conditions, the dielectric leakage current loss can be safely disregarded [79]. To investigate the applicability of the cable thermal-electric rating, 3 testing categories are chosen for different cable installations and operating conditions.

- Submarine HVDC cable (steady state)
- HVDC cable on land (steady state)
- HVDC cable under polarity reversal (transient)

4.4.1 Electrical stress-limited rating for submarine HVDC cable

The rating of submarine sections of HVDC cable from Table 3.2 (D_i = 101mm, γ = 0.03mm.kV^{-1}) is frequently stress-limited, as the thermal environment is often less onerous for the cable than that of the land sections. It assumes:

- Seafloor is isothermal at 12^0C and backfill thermal resistivity is 0.7 K.m.W^{-1}.
- Cable burial depth is between 1m and 3m and the pole-pole configuration is either touching, or separated at least 10m [28].

Therefore, the operating voltage, U, is the controlling parameter varying from 400kV to 550kV, while the bipole circuit with 10m pole-pole separation is buried at an average of 2m below the seafloor to simulate the real practice. The overall layout and boundary condition settings are shown in Figure 3.2 and Figure 3.3. Table 4.5 and Figure 4.4 show the test results.

Table 4.5: Electrical stress-limited rating under various operating voltages

U (kV)	375	400	425	450	475	500	525
$I_{thermal}$ (A)	2210	2210	2210	2210	2210	2210	2210
I_{stress} (A)	2463	2360	2253	2141	2024	1899	1766

$I_{thermal\text{-}electric}$ (A)	2210	2210	2210	2141	2024	1899	1766
FEA (A)	2210	2210	2210	2145	2031	1900	1770
Capacity per pole (MW)	829	884	939	963	965	950	927

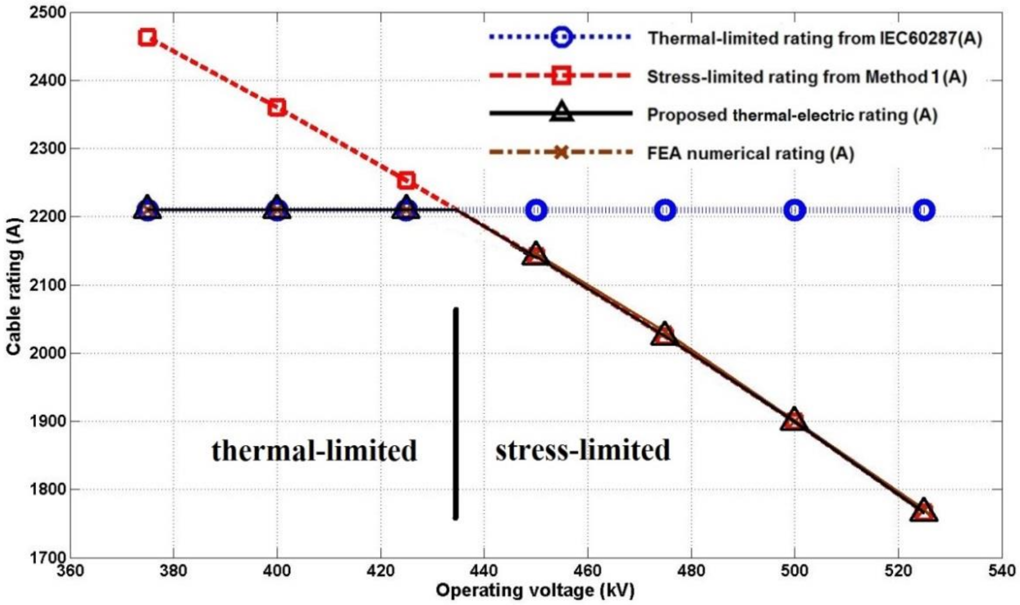

Figure 4.4: Rating plot under various operating voltages

As shown in Table 4.5 and Figure 4.4, the thermal-electric rating agrees well with the FEA modelling solution within a maximum rating difference less than 0.5%. Secondly, two distinct current rating domains are found, depending upon the operating voltage. When the operating voltage is below a critical value for this design (between 425kV to 450kV), the thermal performance limits the rating, while the stress performance becomes the main rating constraint as the voltage goes above 450kV. This finding suggests that the IEC60287 is still applicable when the operating voltage is under the critical value, while it loses its applicability when the critical value is exceeded. Thirdly, it can be shown that a dielectric failure could occur through excessive electrical stressing before the normal upper thermal limit is exceeded, even if no latent defect is present within the cable insulation.

Moreover, from a system operator’s perspective, it is of great value to show, in Figure 4.5, the relationship between the transmission capacity and operating voltage.

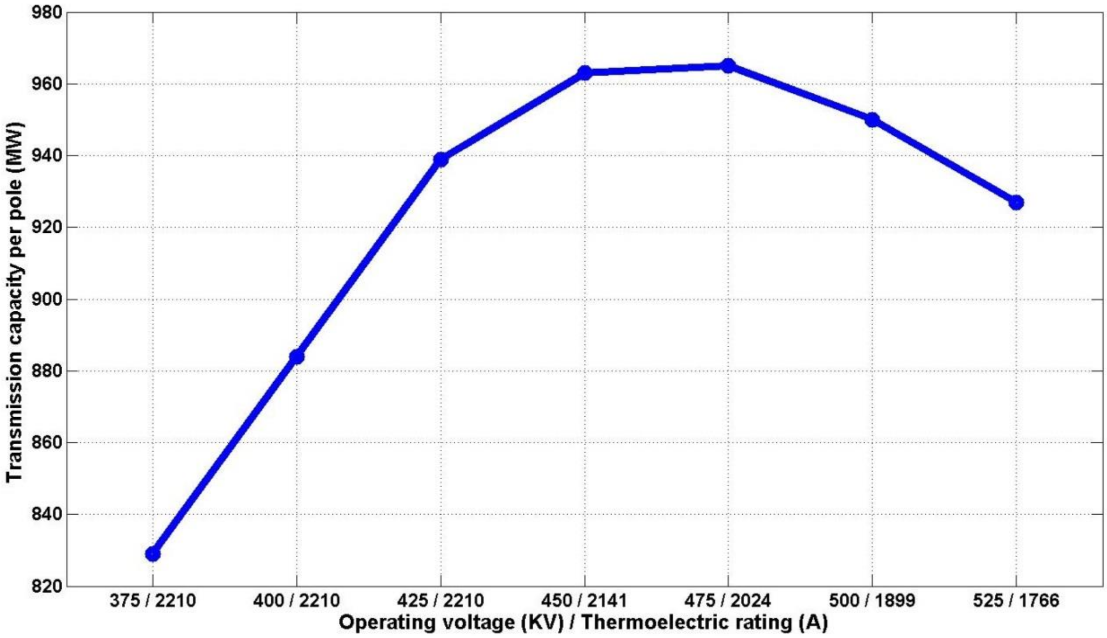

Figure 4.5: Transmission capacity plot at various operating voltages

From Figure 4.5, the HVDC submarine cable under test has a peak transmission capacity up to 970MW which is achieved by gradually increasing the operating voltage from 375kV to 475kV. However beyond this critical voltage level, the power transmission capacity decreases as a result of the reduced stress-limited loading.

Finally, another parameter requiring further explanation is the maximum long-term design dielectric breakdown stress, being 30kV.mm^{-1} in this thesis. Unlike the strictly defined thermal limit where material degradation occurs, the maximum dielectric breakdown stress is a statistical approximation which only guarantees a dielectric safety over a certain period with prescribed survival probability. Therefore, 30kV.mm^{-1} is a satisfactory value suggested by many prior researchers for general MI paper insulations which are designed for steady state operations up to 40 years with an acceptable survival probability. For a more accurate value, the following survival function is generally used, following a Weibull distribution [153]:

$$P(t,E) = exp\left[-\left(\frac{t}{t_0}\right)^a\left(\frac{E}{E_0}\right)^b\right] \tag{4.21}$$

Where; a, b are the Weibull parameters for a particular insulation or particular lengths of, say, a cable sample of particular dimensions. The time t_0 and stress E_0 represent the ‘average’ survival time, t_0, for particular samples of a cable at a stress of E_0. Sample breakdown data for paper insulation can be found in [154].

4.4.2 Electrical stress-limited rating for HVDC cable on land

The rating of directly buried land HVDC cable from Table 3.2 (D_i = 101mm, γ = 0.033mm.kV^{-1}) is complicated, because changes in the cable installation can affect both the thermal-limited and electrical stress-limited rating calculations through the parameter T_4 in (2.2) and (4.12). The model has a land installation shown in Table 3.3 with isothermal ground surface and ambient temperature both at 12 ℃ to simulate the real practice. The overall layout and boundary condition settings are shown in Figure 3.2 and Figure 3.3. Note that in reality, the circuit burial depth normally less than 5m and a rare10m depth chosen in this section is mainly for research purpose only.

Note that the lower one between the thermal-limited rating and the electrical stress-limited rating is named as the thermal-electric rating, I_{TE}. Results are shown in Table 4.6 and plotted in Figure 4.6.

Table 4.6: Thermal-electric rating under various land installations

Separation (m) **Burial depth (m)**		5	10	20
0.5	$I_{thermal}$ (A)	2125	2127	2128
	I_{stress} (A)	1914	1915	1916
	I_{TE} (A)	1914	1915	1916
	FEA (A)	1910	1910	1910
1	$I_{thermal}$ (A)	1997	2006	2008
	I_{stress} (A)	1901	1902	1902
	I_{TE} (A)	1901	1902	1902
	FEA (A)	1898	1895	1895
2	$I_{thermal}$ (A)	1876	1899	1905
	I_{stress} (A)	1885	1889	1890
	I_{TE} (A)	1876	1889	1890
	FEA (A)	1879	1884	1887
4	$I_{thermal}$ (A)	1751	1793	1812
	I_{stress} (A)	1867	1873	1876
	I_{TE} (A)	1751	1793	1812
	FEA (A)	1755	1798	1818
10	$I_{thermal}$ (A)	1597	1648	1689
	I_{stress} (A)	1839	1849	1856
	I_{TE} (A)	1597	1648	1689
	FEA (A)	1595	1644	1681

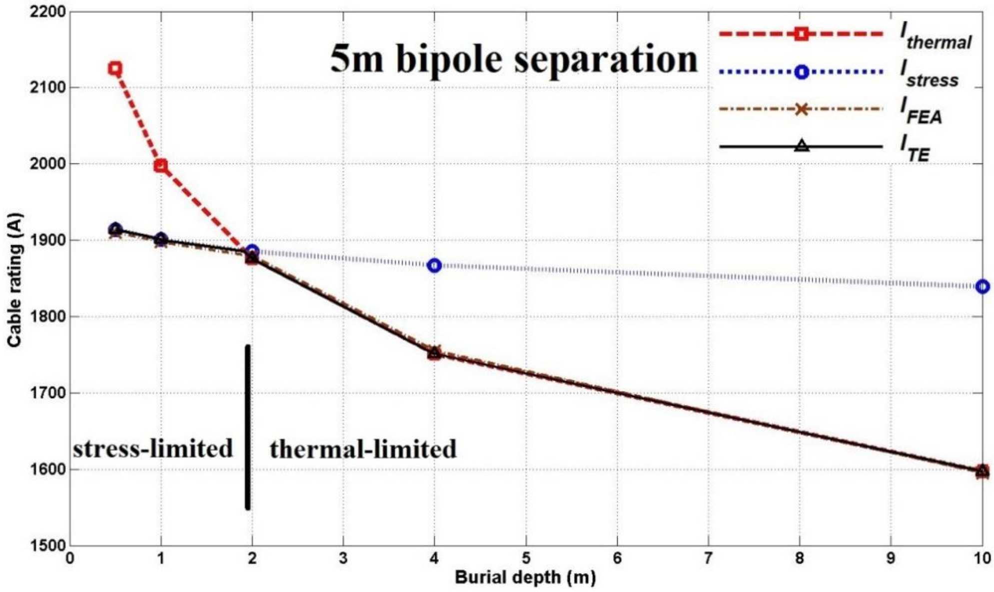

Figure 4.6: Rating plot under various burial depths (5m pole-pole separation)

In Figure 4.6, the circuit rating under various burial depths is plotted for a separation of 5m. It shows that the cable thermal-electric ratings agree well with FEA modelling solutions with a maximum rating difference less than 1% throughout the range of burial depths considered. Both the thermal-limited and electrical stress-limited ratings decrease with an increasing burial depth. However, the stress-limited rating is only slightly impacted by the burial depth due to the small impact of T_4 on the result of (4.11). More importantly, it has been found that the stress-limited rating dominates for shallower burial depths (less than 2m), whereas the deeper burial depths remain thermal-limited. In terms of practical operation, it suggests that the conventional IEC rating calculation is still applicable for most directly buried HVDC land cables. In Figure 4.7 below, the simulation is repeated but with an increased bipole separation of 20m.

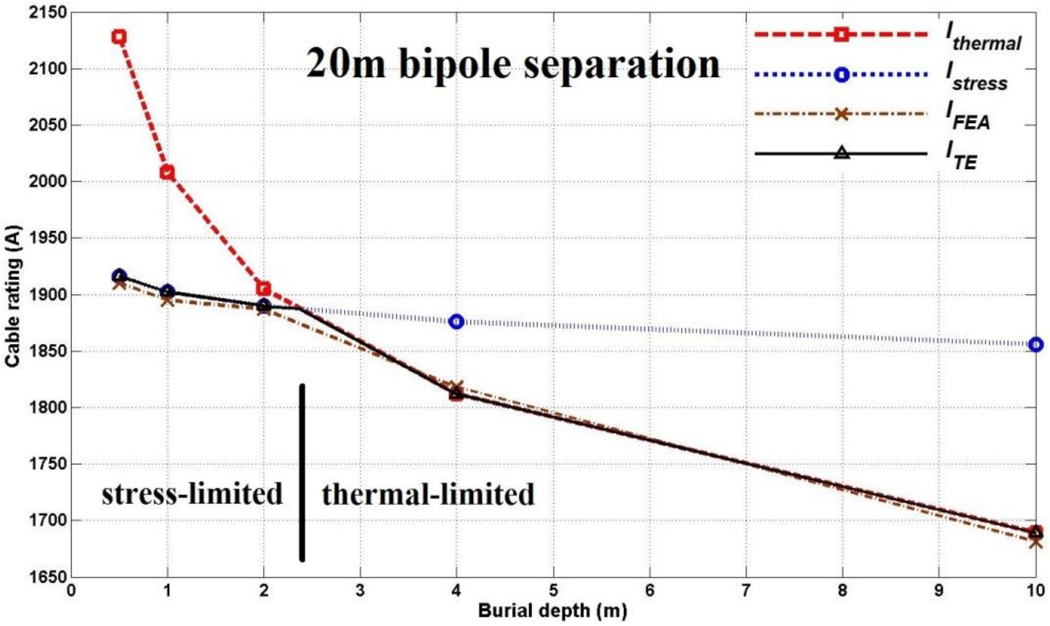

Figure 4.7: Rating plot under various burial depths (20m pole-pole separation)

From Figure 4.7, similar conclusions to Figure 4.6 can be drawn and it shows that the bipole separation has little effect on the thermal-electric rating (less than 1% variation) as long as the rating is stress-limited. In addition, the transition boundary moves to a slightly greater depth of 2.3m.

Considering an overall cable circuit including both the submarine and land sections, the rating limit can often come from the land cables, which are often thermal-limited under nominal installations and operating conditions.

4.4.3 Electrical stress-limited rating under polarity reversal

Many HVDC trading links use line commutated converters, so polarity reversals are required for changing the power flow direction. High transient electrical stress occurs near the cable conductor immediately after a polarity reversal due to the existence of space charges. As the inversion time is normally less than 120s [46], while the electrical time constant of large HVDC cables are several thousand minutes as R-C circuits, the principle of stress superposition applies. A simplified sample calculation of the cable dielectric time constant is provided as follows:

$$R_{eq} \approx \frac{1}{2\pi}\int_{R_i}^{R_o}\frac{\rho_{eq}}{r}dr = \frac{\rho_{eq}}{2\pi}\ln\left(\frac{R_o}{R_i}\right) \tag{4.22}$$

$$C = \frac{\varepsilon_r}{18\ln\left(\frac{D_i}{D_c}\right)}10^{-9} \quad [31] \tag{4.23}$$

$$\tau = CR_{eq} \approx \frac{10^{16}}{2\pi}\ln\left(\frac{50.5}{30.25}\right)\cdot\frac{3.5}{18\ln\left(\frac{101}{50.5}\right)}10^{-9} \approx 310000s\ (86\ hrs) \tag{4.24}$$

Where; R_{eq} is the equivalent electrical resistance of the cable insulation [Ω.m^{-1}], ρ_{eq} the equivalent electrical resistivity of the cable insulation [Ω.m], C the equivalent insulation electrical capacitance [F], ε_r the relative dielectric permittivity, D_i the cable insulation outer diameter [mm], D_c the cable conductor outer diameter [mm], and τ is the cable insulation time constant [s]. Note that during the transient, only the dielectric electrical resistivity is changing with time, while the capacitance remains constant.

Denoting E_{trans} the transient dielectric electrical stress [kV.mm^{-1}] and E_{pre} the preload steady state dielectric electrical stress [kV.mm^{-1}], the following equations hold:

$$E_{trans} = E_{pre} + E_{geom} \tag{4.25}$$

$$E_{geom}(r) = \frac{U}{r\ln(\frac{R_o}{R_i})} \tag{4.26}$$

Where; E_{geom} is the geometric electrical stress [kV.mm^{-1}] and r is the radius where the function is evaluated [mm]. The applicability of (4.26) is verified by the fact that the permittivity of the dielectric is substantially constant throughout the operating temperature range of most paper insulated HVDC cables, which is less than 50^{0}C. As the maximum E_{trans} is normally found at R_i close to the cable conductor, substitute (4.26) into (4.25), then E_{pre} at R_i can be calculated by:

$$E_{pre}(R_i) = E_{trans}(R_i) + \frac{2U}{R_i\ln(\frac{R_o}{R_i})} \tag{4.27}$$

Note that the factor 2 in (4.27) comes from the fact that the operating voltage is actually changing from U to $-U$ during a polarity reversal. Therefore, the E_{trans} at R_i can be chosen as the first reference point (E_{ref1}, r_{ref1}) to calculate the required preload current, while the second reference point (E_{ref2}, r_{ref2}) remains the same as before. In the polarity reversal test, special considerations are given to the effects of various inversion times (10s, 60s and 120s) on the accuracy of the preloading calculation. We consider here a land bipolar cable circuit from Table 3.2 (D_i = 101mm, γ = 0.033mm.kV^{-1}) with 3m burial depth, 10m pole-pole separation, 500kV operating voltage and 12°C ambient temperature. The overall layout and boundary condition settings are shown in Figure 3.2 and Figure 3.3. The voltage polarity reversal transient is simulated by a ‘step’ function with linear-ramp front, which starts at t = 0s. Generally, the weak point of the dielectric during transients is the oil gap, while the kraft paper has much higher transient breakdown strength. Therefore a typical value of the maximum permissible E_{trans} is between 40kV.mm^{-1} and 50kV.mm^{-1} [48], determined by the breakdown stress of the oil gap [155]. For demonstration, a minimum value of 40kV.mm^{-1} is chosen, with results from the FEA modelling given in Table 4.7. Moreover, the field evolution under a 120s polarity reversal is plotted in Figure 4.8. Note that the actual transient electric field evolvement consists of two aspects as: 1. displacement current generated during the polarity reversal; 2. space charge relocation due to the field dependency coefficient of the dielectric electrical conductivity. As an initial study on this transient process, only the space charge relocation effect (i.e. charge relocation) is included to show a rough trend of field evolvement. The displacement current effect will be examined in the future work. However, it won't affect the key maximum E_{trans} during the polarity reversal as the superposition still applies.

Table 4.7: Maximum transient stress under various polarity reversals

	Maximum E_{trans} at R_i near conductor (kV.mm^{-1})	
Inversion time (s)	Preloading=1837A	Reduced preloading=1236A
120	44.35	39.88
60	44.81	39.91
10	45.21	39.94

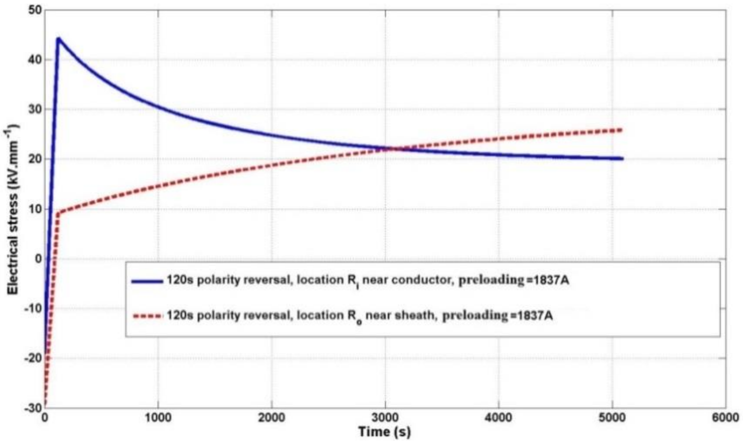

Figure 4.8: Dielectric electrical stress evolvement under 120s polarity reversal

From Figure 4.8, it can be shown that both stress curves change linearly with the changing operating voltage during the polarity reversal. However, a higher electrical stress is induced at R_i near the conductor immediately after the transient and the cable rating is stress-limited. These observations agree well with the theory in [22] and demonstrate the application of the stress superposition (4.25). After the polarity reversal (t = 120s and onwards), the stress at R_o starts to increase and gradually surpasses the decreasing stress at R_i. Finally, a steady state dc field occurs with the highest stress at the insulation outer radius R_o. Figure 4.9 below shows how the average peak transient stress at R_i changes with various preloading and Figure 4.10 shows the application of a reduced preloading.

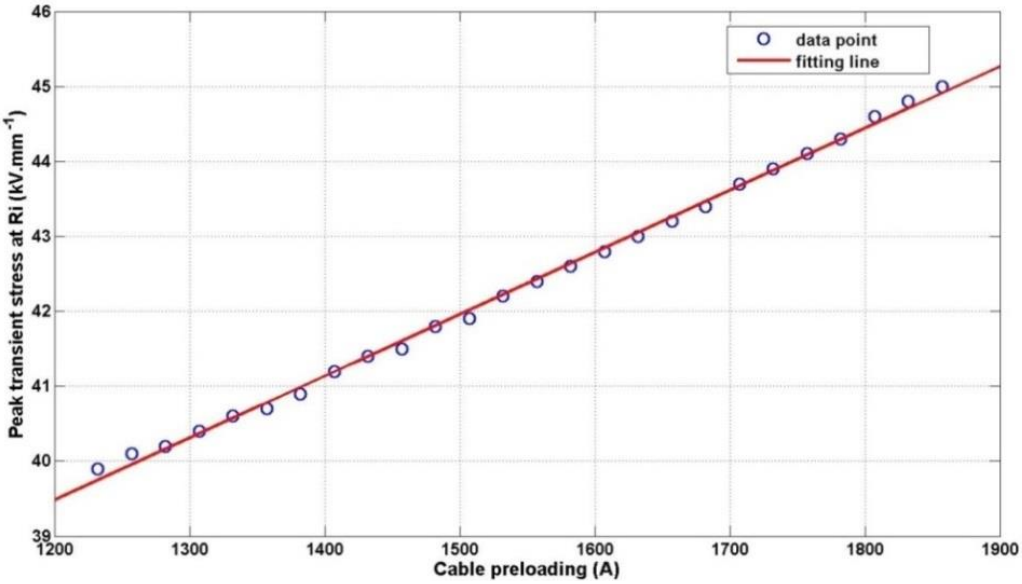

Figure 4.9: Peak transient stress plot under various cable reloadings

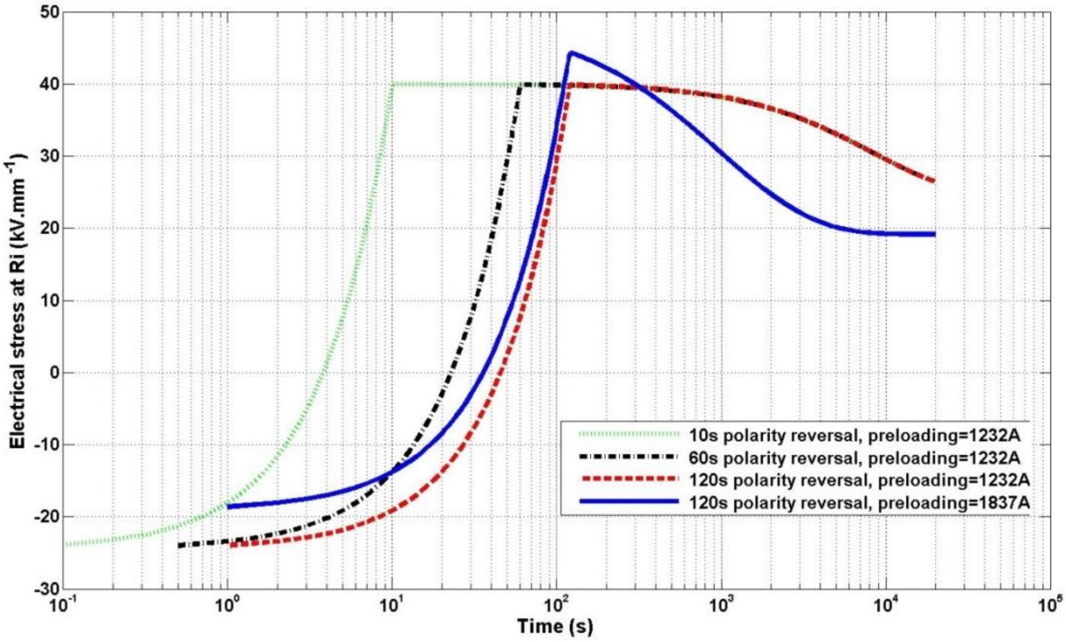

Figure 4.10: Dielectric electrical stress plot for various polarity reversal durations

According to Table 4.7 and Figure 4.10, the maximum electrical stress requirement (40kV.mm^{-1}) is satisfied by reducing the preloading accordingly. Further, the calculation is more accurate and valuable for faster polarity reversals as it relies on the applicability of the stress superposition. As the dielectric design is a statistical approach, knowledge of time durations for various stress levels is of great importance, which is summarized in Table 4.8 below:

Table 4.8: Duration above various stress levels

	Duration over certain stress levels (s)				
Stress levels (kV.mm^{-1})	30	32.5	35	37.5	40
120s polarity reversal					
Preloading =1837A	958	690	484	319	185

Preloading =1800A (2% drop)	1138	815	556	369	209
Preloading =1745A (5% drop)	1451	1027	704	450	243
10s polarity reversal					
Preloading =1837A	960	698	498	336	205
Preloading =1800A (2% drop)	1139	816	586	386	234
Preloading =1745A (5% drop)	1459	1037	719	469	264

From Table 4.8, a short polarity reversal (10s) gives longer overstress durations than a long polarity reversal (120s). Moreover, although the peak transient stress is almost proportional to the cable preloading, decreasing the preloading will prolong the highly stressed duration as a side effect. In Figure 4.10, this finding is also supported with a lower preloading (red dashed line) leading to a slower field relaxation, while a faster relaxation is observed with a higher preloading (blue solid line). To further examine this trend, Figure 4.11 below shows the electric stress evolution under various preloading, under a polarity reversal duration of 60s:

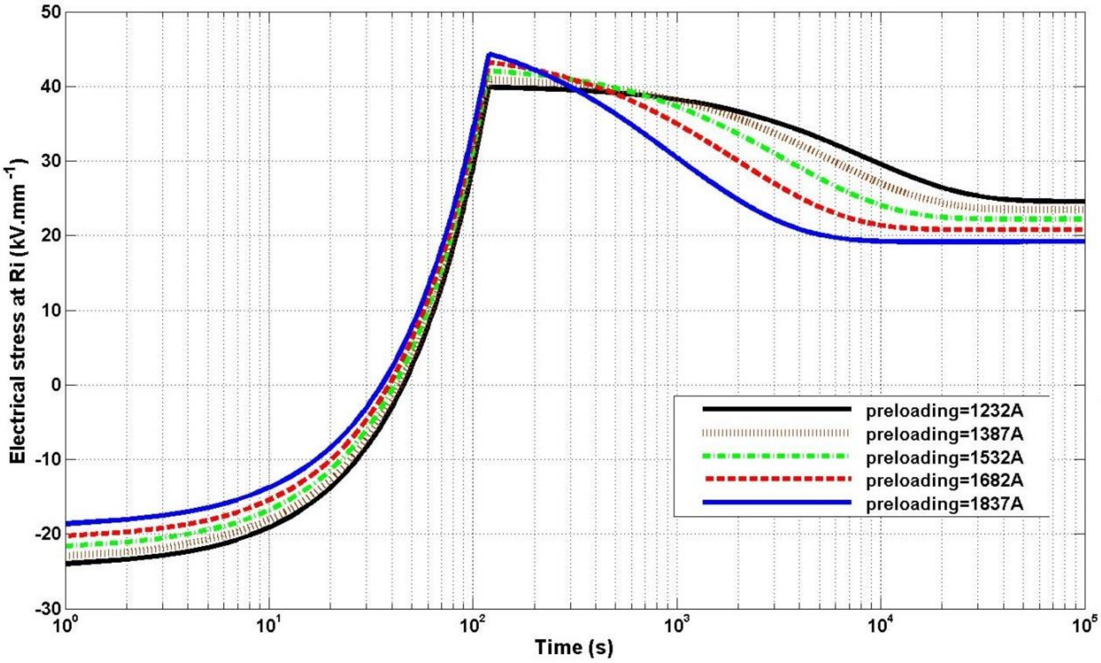

Figure 4.11: Dielectric electrical stress plot for various preloadings

A possible physical reason accounting for this relaxation trend is that, under a bigger preloading, more energy is stored just after the polarity reversal which leads to a higher transient temperature and thus electrical conductivity (i.e. faster charge transportation and relocation). Consequently, the field relaxation is faster at the conductor screen as shown in Figure 4.11.

In practice, it will be important to consider the most appropriate values of transient dielectric breakdown strength. If higher transient stresses can be tolerated, without an increase in risk to the cable, then the amount of preload reduction required is much smaller. This means that the polarity reversal can be allowed regardless of the temperature of the cable. To achieve this safely, a much more advanced knowledge of charge transfer within MI insulation systems will be required.

4.5 Summary

This chapter presents the electrical stress-limited rating method for HVDC cables, which considers the possibility of the maximum dielectric stress as the current rating constraint. The applicability and accuracy of the analytical method has been successfully demonstrated by numerical FEA modelling.

Based on the study, it has been found that for steady state evaluation, two distinct rating domains (thermal-limited and stress-limited) are identified, where the domain boundary is determined by operating voltages and the installation thermal environment.

Secondly, the IEC calculation is broadly applicable for operating voltage levels at which the cable is thermal-limited. Shallow buried cables are generally electrical stress-limited. However, the circuit starts to switch to thermal-limited for deeper burial depths, where the IEC rating becomes applicable again.

Finally, for transient evaluation under polarity reversals, the cable is generally stress-limited where the stress superposition holds. The maximum transient stress requirement during polarity reversals can be satisfied by reducing the preload current. However, if a better understanding of the charge transport behaviour can be gained, it may be possible to permit higher levels of transient stress for short times. This would need to be investigated thoroughly to avoid increasing risks to the cable asset.

Chapter 5

Mechanical Pressure-limited Rating

As introduced in Section 2.4, the main challenge of developing the mechanical pressure-limited rating is to calculate cable internal pressure under three coupled physical disciplines: electrical circuit theory, thermodynamics and theory of elasticity. To illustrate the derivation process and its applications, this chapter is divided into following three main sections:

- Technical approach and key assumptions
- Thermal-mechanical pressure calculation
- Mechanical pressure-limited rating and applications

5.1 Technical approach and key assumptions

To derive an analytical calculation of cable internal pressure applicable for both the microscopic cavity creation and the macroscopic cavity creation, a coupled physics approach is required, which combines elasticity theory, thermodynamics and electrical circuit theory. As the three fundamental physics have distinct application domains and units, it is necessary to mathematically formulate the overall physical interaction and coordinate various unit systems.

Before a current loading, the cable is assumed to have a uniformly distributed temperature profile with value the same as ambient. Once the cable conductor starts to carry dc current, the conductor joule loss develops as the only internal heat source (negligible dielectric leakage current loss under dc applications [156]). Mathematically, the joule loss can be analytically calculated through the electrical circuit theory, by providing current loading and conductor dc resistance (i.e. Equation (2.48) on Page 31).

Once the cable reaches its steady state, the initial uniformly distributed temperature profile has evolved to a graded temperature distribution with the highest temperature at the cable centre, and gradually decreases outwards in the radial direction. Mathematically, the detailed radial temperature distribution can be analytically calculated through the one dimensional thermal network analogy in thermodynamics, by providing heat source, series thermal resistance and ambient temperature (i.e. Equation (2.50) on Page 31).

At the same time, the temperature variation between the initial load-off state and the continuous load-on state causes a volumetric thermal expansion of each cable component to various extent (i.e. Equation (2.52), (2.53) on page 31), which is physically observed as layer-to-layer boundary displacement. Mechanically, this boundary displacement due to the above thermal-electric interaction is defined as mechanical strain in the theory of elasticity (i.e. Equation (2.55), (2.60) on page 32).

Finally, the internal mechanical stress distribution is analytically calculated in theory of elasticity, which mathematically links mechanical stress and strain through material Young's modulus and Poisson's ratio (i.e. Equation (2.56), (2.61) on page 33). To make the calculation mathematically valid, external compressive pressure is added as the boundary condition, and no radial layer-to-layer delamination is suggested to be the continuous condition. Therefore, by formulating and combining the physical processes above, a mathematical calculation can be derived which takes the electrical conductor current as input variable and will output mechanical stress as result.

The model consists of three concentric layers representing the cable conductor (outer radius r_c), insulation (outer radius r_i) and metallic sheath (outer radius r_s). In Figure 5.1 below, P_1 is the absolute value of the interfacial pressure between conductor and insulation, P_2 the pressure magnitude between insulation and sheath, and P_3 is the absolute value of the external compressive pressure (e.g. pressure tapes). By default, each layer is subjected to compressive pressures (with negative sign) on both inner and outer surfaces.

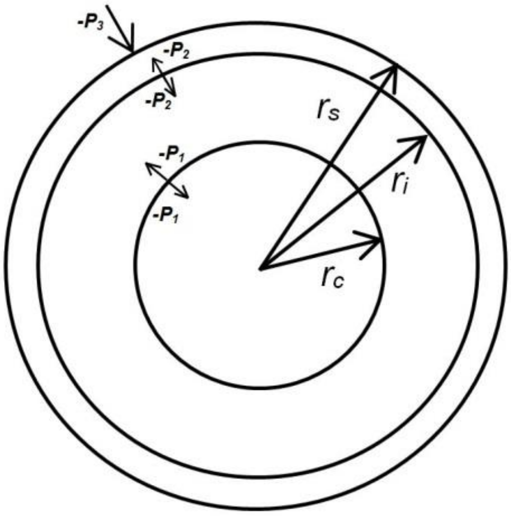

Figure 5.1: Three layer cable cross section

Before deriving the pressure calculation step by step, several assumptions are made as follows:

- Both Kraft paper and impregnant are incompressible
- Thermal expansion coefficients are constant over the temperature range studied [22]

For MI-type HVDC cables, it is important to properly model the insulation layer, which is a combination of Kraft paper and high viscosity impregnant (mineral oil T2015). Thus, two extremes are considered in this thesis. At 'low temperature' (e.g. 20 ℃ or lower), the insulation is regarded as isotropic and elastic solid with equivalent thermal and mechanical properties, because the impregnant viscosity remains high under low temperatures.

However, at ‘high temperature’ (e.g. 50 ℃ or higher), the insulation is assumed to have a uniform pressure distribution with incompressible Kraft paper and impregnant ‘liquid’. This assumption is based on the fact that Kraft paper normally has porosity from 35% to 55% (paper density 650 – 1000 kg.m^{-3}, fibre density 1500 kg.m^{-3} [22]), and the thermal expansion of the impregnant is, at least, 30 times greater than that of paper (α_{Vo} = 6.4 $\times 10^{-4}$ K^{-1} [157], α_{Vp} = 1.92 $\times 10^{-5}$ K^{-1} [158]). It means that at the nominal operating temperatures around 50 ℃, the impregnant volumetric percentage will increase after thermal expansion. Also with a greater mobility, it is able to transport between paper layers through dielectric butt gaps. Thus, Pascal’s law applies which states that the pressure exerted anywhere in a confined incompressible fluid is transmitted equally in all directions [159].

5.2 Thermal-Mechanical pressure calculation

In this sub section, the analytical calculation of the cable internal pressure is derived under both the ‘low temperature’ and ‘high temperature’ analyses. By quantifying the pre-existing dielectric cavity (Equation (5.49)), the method is believed applicable to both the microscopic cavity creation and macroscopic cavity creation mechanisms. To start with, several key equations in Section 2.4 are briefly restated, for a clear illustration.

Joule loss

$$W_c = I^2 R_{dc} \tag{5.1}$$

Annulus temperature rise distribution (inner radius R_i, outer radius R_o)

$$\theta_{rise}(r) = \theta(r) - \theta_{amb} = I^2 R_{dc}\left[\frac{\rho_t}{2\pi}\ln\left(\frac{R_o}{r}\right) + T_{total}\right] \tag{5.2}$$

Plane stress analysis

$$u(r) = (1+v)\frac{\alpha_L}{r}\int_a^r \theta_{rise}(r)rdr + K_1 r + \frac{K_2}{r} \tag{5.3}$$

$$\sigma_r(r) = \frac{-\alpha_L E_Y}{r^2}\int_a^r \theta_{rise}(r)rdr + \frac{E_Y}{1-v^2}\left[K_1(1+v) - \frac{K_2(1-v)}{r^2}\right] \tag{5.4}$$

$$\sigma_\theta(r) = \frac{\alpha_L E_Y}{r^2}\int_a^r \theta_{rise}(r)rdr - \alpha_L E_Y \theta_{rise}(r) + \frac{E_Y}{1-v^2}\left[K_1(1+v) + \frac{K_2(1-v)}{r^2}\right] \tag{5.5}$$

Plane strain analysis

$$u(r) = \frac{(1+v)\alpha_L}{(1-v)r}\int_a^r \theta_{rise}(r)rdr + K_1 r + \frac{K_2}{r} \tag{5.6}$$

$$\sigma_r(r) = \frac{-\alpha_L E_Y}{(1-v)r^2}\int_a^r \theta_{rise}(r)rdr + \frac{E_Y}{1+v}\left[\frac{K_1}{1-2v} - \frac{K_2}{r^2}\right] \tag{5.7}$$

$$\sigma_\theta(r) = \frac{\alpha_L E_Y}{(1-v)r^2}\int_a^r \theta_{rise}(r)rdr - \frac{\alpha_L E_Y \theta_{rise}(r)}{1-v} + \frac{E_Y}{1+v}\left[\frac{K_1}{1-2v} + \frac{K_2}{r^2}\right] \tag{5.8}$$

Please refer to either Section 2.4 or ‘Symbols and Abbreviations’ for the variable definition.

As the integral of ‘ $\theta_{rise}(r)\cdot r$ ’ appears in (5.3) to (5.8), it is thus calculated in advance (i.e. through integration by parts) to help understand the mathematical derivatives in the following sub sections:

$$\int_a^r \theta_{rise}(r)rdr = \frac{I^2 R_{dc}\rho_t}{4\pi}\left[a^2\ln(a) - r^2\ln(r) + \frac{r^2-a^2}{2}\right] + \frac{I^2 R_{dc}}{2}(r^2-a^2)\left[\frac{\rho_t}{2\pi}\ln(R_o) + T_{total}\right] \tag{5.9}$$

In addition, the strain calculation on different cable layers in the following sub sections is expressed in a general form for both plane stress analysis and plane strain analysis, shown as below:

$$u_j(r) = CI^2 + DP_1 + FP_2 + GP_3 \tag{5.10}$$

Where; the subscript *j* refers to the cable layer where the radial strain is calculated, and *C, D, F, G* are constant coefficients for variable I^2, P_1, P_2, P_3. Note that these coefficients are uniquely defined at different radial locations of different cable cross sectional layers.

5.2.1 Low temperature analysis

Under the 'low temperature' analysis, the insulation is assumed to be isotropic and elastic with equivalent mechanical and thermal properties.

Step 1. Plane stress/ strain analysis for the cable conductor

For the cable conductor, it is subject to its own thermal expansion and compressive pressure, $-P_1$, at its outer radius (i.e. $r = r_c$). Therefore, its radial strain, u_c, is a function of I^2 and P_1 only, and the coefficients *F*, *G* in (5.10) are zero.

By applying the boundary condition (i.e. $-P_1$ at $r = r_c$) to the radial stress calculation (5.4) with its temperature integral term calculated through (5.9), coefficient K_1 in (5.4) can be firstly expressed as a function of I^2 and P_1. Note that K_2 must be zero to mathematically eliminate the singularity when the radius, *r*, goes to zero [82]. Then, substitute K_2 into the radial strain calculation (5.3) and calculate again the temperature integral term using (5.9), an expression of the conductor radial strain, u_c, at its outer radius, r_c, is finally derived for plane stress analysis as follows:

Plane stress analysis (cable conductor)

$$u_c(r_c) = C_1 I^2 + D_1 P_1 \tag{5.11}$$

$$C_1 = R_{dc}\alpha_{Lc} r_c (T_1 + T_2 + T_3 + T_4) \tag{5.12}$$

$$D_1 = -\frac{(1-v_c)r_c}{E_c} \tag{5.13}$$

Similarly, follow the same procedure above but replace (5.3), (5.4) from the plane stress analysis with corresponding plane strain analysis equations (5.6), (5.7), the conductor radial strain, u_c, at its outer radius, r_c, is thus derived for plane strain analysis as follows:

Plane strain analysis (cable conductor)

$$u_c(r_c) = C_2 I^2 + D_2 P_1 \tag{5.14}$$

$$C_2 = R_{dc}\alpha_{Lc} r_c (1 + v_c)(T_1 + T_2 + T_3 + T_4) \tag{5.15}$$

$$D_2 = -\frac{(1+v_c)(1-2v_c)r_c}{E_c} \tag{5.16}$$

Step 2. Plane stress/ strain analysis for the cable insulation

For the cable insulation, it is subject to its own thermal expansion, compressive pressure, $-P_1$, at its inner radius (i.e. $r = r_c$), and compressive pressure, $-P_2$, at its outer radius (i.e. $r = r_i$). Therefore, its radial strain, u_i, is a function of I^2, P_1, P_2, and the coefficient G in (5.10) is zero.

By applying the boundary condition (i.e. $-P_1$ at $r = r_c$ and $-P_2$ at $r = r_i$) to the radial stress calculation (5.4) with its temperature integral term calculated through (5.9), both coefficients K_1 and K_2 in (5.4) can be firstly expressed as a function of I^2, P_1 and P_2. Then, substitute K_1 and K_2 into the radial strain calculation (5.3) and calculate again the temperature integral term using (5.9), an expression of the insulation radial strain, u_i, at either its inner radius, r_c or outer radius, r_i, is finally derived for plane stress analysis as follows:

Plane stress analysis (cable insulation)

$$u_i(r_c) = C_3 I^2 + D_3 P_1 + F_1 P_2 \tag{5.17}$$

$$C_3 = \frac{-r_c}{r_c^2 - r_i^2}\left\{\frac{\alpha_{Li} R_{dc} \rho_i}{2\pi}\left[r_c^2 \ln(r_c) - r_i^2 \ln(r_i) + \frac{r_i^2 - r_c^2}{2}\right] + \alpha_{Li} R_{dc} (r_i^2 - r_c^2)\left[\frac{\rho_i \ln(r_i)}{2\pi} + T_3 + T_4\right]\right\} \tag{5.18}$$

$$D_3 = -\frac{r_c^3(1 - v_i) + r_c r_i^2 (1 + v_i)}{E_i(r_c^2 - r_i^2)} \tag{5.19}$$

$$F_1 = \frac{2 r_c r_i^2}{E_i(r_c^2 - r_i^2)} \tag{5.20}$$

$$u_i(r_i) = C_4 I^2 + D_4 P_1 + F_2 P_2 \tag{5.21}$$

$$\begin{aligned} C_4 = {} & \frac{\alpha_{Li}(1 + v_i)}{r_i}\left\{\frac{R_{dc} \rho_i}{4\pi}\left[r_c^2 \ln(r_c) - r_i^2 \ln(r_i) + \frac{r_i^2 - r_c^2}{2}\right] + \frac{R_{dc}(r_i^2 - r_c^2)}{2}\left[\frac{\rho_i \ln(r_i)}{2\pi} + T_3 + T_4\right]\right\} - \\ & \frac{r_i^2(1 - v_i) + r_c^2(1 + v_i)}{r_c^2 - r_i^2}\left\{\frac{\alpha_{Li} R_{dc} \rho_i}{4\pi r_i}\left[r_c^2 \ln(r_c) - r_i^2 \ln(r_i) + \frac{r_i^2 - r_c^2}{2}\right] + \frac{\alpha_{Li} R_{dc}}{2 r_i}(r_i^2 - r_c^2)\left[\frac{\rho_i \ln(r_i)}{2\pi} + T_3 + T_4\right]\right\} \end{aligned} \tag{5.22}$$

$$D_4 = \frac{-2 r_i r_c^2}{E_i(r_c^2 - r_i^2)} \tag{5.23}$$

$$F_2 = \frac{r_i^3(1 - v_i) + r_i r_c^2 (1 + v_i)}{E_i(r_c^2 - r_i^2)} \tag{5.24}$$

Similarly, follow the same procedure above but replace (5.3), (5.4) from the plane stress analysis with corresponding plane strain analysis equations (5.6), (5.7), the insulation radial strain, u_i, at either its inner radius, r_c or outer radius, r_i, is thus derived for plane strain analysis as follows:

Plane strain analysis (cable insulation)

$$u_i(r_c) = C_5 I^2 + D_5 P_1 + F_3 P_2 \tag{5.25}$$

$$\begin{aligned} C_5 = {} & \frac{-r_c}{r_c^2 - r_i^2}\left\{\frac{(1 + v_i)\alpha_{Li} R_{dc} \rho_i}{2\pi}\left[r_c^2 \ln(r_c) - r_i^2 \ln(r_i) + \frac{r_i^2 - r_c^2}{2}\right] + \alpha_{Li} R_{dc} (1 + v_i)(r_i^2 - \right. \\ & \left. r_c^2)\left[\frac{\rho_i \ln(r_i)}{2\pi} + T_3 + T_4\right]\right\} \end{aligned} \tag{5.26}$$

$$D_5 = -\frac{(1 + v_i)\left[r_c^3(1 - 2v_i) + r_c r_i^2\right]}{E_i(r_c^2 - r_i^2)} \tag{5.27}$$

$$F_3 = \frac{2(1 - v_i^2) r_c r_i^2}{E_i(r_c^2 - r_i^2)} \tag{5.28}$$

$$u_i(r_i) = C_6 I^2 + D_6 P_1 + F_4 P_2 \tag{5.29}$$

$$C_6 = \frac{\alpha_{Li}(1+v_i)}{r_i(1-v_i)}\left\{\frac{R_{dc}\rho_i}{4\pi}\left[r_c^2\ln(r_c) - r_i^2\ln(r_i) + \frac{r_i^2-r_c^2}{2}\right] + \frac{R_{dc}(r_i^2-r_c^2)}{2}\left[\frac{\rho_i\ln(r_i)}{2\pi} + T_3 + T_4\right]\right\} - \frac{r_i^2(1-2v_i)+r_c^2}{r_c^2-r_i^2}\left\{\frac{(1+v_i)\alpha_{Li}R_{dc}\rho_i}{(1-v_i)4\pi r_i}\left[r_c^2\ln(r_c) - r_i^2\ln(r_i) + \frac{r_i^2-r_c^2}{2}\right] + \frac{(1+v_i)\alpha_{Li}R_{dc}}{(1-v_i)2r_i}(r_i^2 - r_c^2)\left[\frac{\rho_i\ln(r_i)}{2\pi} + T_3 + T_4\right]\right\} \tag{5.30}$$

$$D_6 = -\frac{2r_ir_c^2(1-v_i^2)}{E_i(r_c^2-r_i^2)} \tag{5.31}$$

$$F_4 = \frac{(1+v_i)[r_i^3(1-2v_i)+r_ir_c^2]}{E_i(r_c^2-r_i^2)} \tag{5.32}$$

Step 3. **Plane stress/ strain analysis for the cable sheath**

For the cable sheath, it is subject to its own thermal expansion, compressive pressure, -P_2, at its inner radius (i.e. $r = r_i$), and external compressive pressure, -P_3, at its outer radius (i.e. $r = r_s$). Therefore, its radial strain, u_s, is a function of I^2, P_2, P_3, and the coefficient D in (5.10) is zero.

By applying the boundary condition (i.e. -P_2 at $r = r_i$ and -P_3 at $r = r_s$) to the radial stress calculation (5.4) with its temperature integral term calculated through (5.9), both coefficients K_1 and K_2 in (5.4) can be firstly expressed as a function of I^2, P_2 and P_3. Then, substitute K_1 and K_2 into the radial strain calculation (5.3) and calculate again the temperature integral term using (5.9), an expression of the sheath radial strain, u_s, at its inner radius, r_i, is finally derived for plane stress analysis as follows:

Plane stress analysis (cable sheath)

$$u_s(r_i) = C_7I^2 + F_5P_2 + G_1P_3 \tag{5.33}$$

$$C_7 = \frac{-r_i}{r_i^2-r_s^2}\left\{\frac{\alpha_{Ls}R_{dc}\rho_s}{2\pi}\left[r_i^2\ln(r_i) - r_s^2\ln(r_s) + \frac{r_s^2-r_i^2}{2}\right] + \alpha_{Ls}R_{dc}(r_s^2 - r_i^2)\left[\frac{\rho_s\ln(r_s)}{2\pi} + T_3 + T_4\right]\right\} \tag{5.34}$$

$$F_5 = -\frac{r_i^3(1-v_s)+r_ir_s^2(1+v_s)}{E_s(r_i^2-r_s^2)} \tag{5.35}$$

$$G_1 = \frac{2r_ir_s^2}{E_s(r_i^2-r_s^2)} \tag{5.36}$$

Similarly, follow the same procedure above but replace (5.3), (5.4) from the plane stress analysis with corresponding plane strain analysis equations (5.6), (5.7), the insulation radial strain, u_s, at its inner radius, r_i, is thus derived for plane strain analysis as follows:

Plane strain analysis (cable sheath)

$$u_s(r_i) = C_8I^2 + F_6P_2 + G_2P_3 \tag{5.37}$$

$$C_8 = \frac{-r_i}{r_i^2-r_s^2}\left\{\frac{(1+v_s)\alpha_{Ls}R_{dc}\rho_s}{2\pi}\left[r_i^2\ln(r_i) - r_s^2\ln(r_s) + \frac{r_s^2-r_i^2}{2}\right] + \alpha_{Ls}R_{dc}(1+v_s)(r_s^2 - r_i^2)\left[\frac{\rho_s\ln(r_s)}{2\pi} + T_3 + T_4\right]\right\} \tag{5.38}$$

$$F_6 = -\frac{(1+v_s)[(1-2v_s)r_i^3+r_ir_s^2]}{E_s(r_i^2-r_s^2)} \tag{5.39}$$

$$G_2 = \frac{2(1-v_s^2)r_ir_s^2}{E_s(r_i^2-r_s^2)} \tag{5.40}$$

Step 4. **Cable internal mechanical stress calculation**

As any radial delamination is to be avoided (i.e. continuous condition), the radial strains on both sides of an interface should compensate with each other. In other words, the radial strain $u_c(r_c)$

should equal to $u_i(r_c)$ at the conductor-insulation interface, and $u_i(r_i)$ should equal to $u_s(r_i)$ at the insulation-sheath interface. Therefore, by equalling (5.11) to (5.17) at $r = r_c$ and (5.21) to (5.33) at $r = r_i$, following simultaneous equations are derived for the plane stress analysis.

Plane stress analysis

$$\begin{cases} (C_1 - C_3)I^2 + (D_1 - D_3)P_1 - F_1P_2 = 0 & (5.41) \\ (C_4 - C_7)I^2 + (F_2 - F_5)P_2 - G_1P_3 + D_4P_1 = 0 & (5.42) \end{cases}$$

Similarly, by equalling (5.14) to (5.25) at $r = r_c$ and (5.29) to (5.37) at $r = r_i$, following simultaneous equations are derived for the plane strain analysis.

Plane strain analysis

$$\begin{cases} (C_2 - C_5)I^2 + (D_2 - D_5)P_1 - F_3P_2 = 0 & (5.43) \\ (C_6 - C_8)I^2 + (F_4 - F_6)P_2 - G_2P_3 + D_6P_1 = 0 & (5.44) \end{cases}$$

Therefore, both P_1 and P_2 can be uniquely calculated as function of I^2 and P_3, by solving the above simultaneous equations. As examples, the pressure P_2 is calculated as follows.

Plane stress analysis

$$P_2 = \left(\frac{C_3D_4 - C_1D_4 + C_7D_3 - C_7D_1 - C_4D_3 + C_4D_1}{D_1F_5 + D_3F_2 - D_4F_1 - D_3F_5 - D_1F_2}\right) I^2 + \left(\frac{D_3G_1 - D_1G_1}{D_1F_5 + D_3F_2 - D_4F_1 - D_3F_5 - D_1F_2}\right) P_3 \tag{5.45}$$

Plane strain analysis

$$P_2 = \left(\frac{C_5D_6 - C_2D_6 + C_8D_5 - C_6D_5 - C_8D_2 + C_6D_2}{D_2F_6 + D_5F_4 - D_6F_3 - D_2F_4 - D_5F_6}\right) I^2 + \left(\frac{D_5G_2 - D_2G_2}{D_2F_6 + D_5F_4 - D_6F_3 - D_2F_4 - D_5F_6}\right) P_3 \tag{5.46}$$

5.2.2 High temperature analysis

Under the 'high temperature' analysis, the insulation consists of Kraft paper and impregnant with distinct thermal expansion coefficients. As the impregnant oil has a much greater thermal expansion and its viscosity drops with an increasing temperature, a uniform pressure distribution is assumed across the insulation layer. Therefore, P_1 equals to P_2.

Denote ϕ as the Kraft paper porosity, thus for a unit length of cable insulation, its volumetric variation, ΔV_+, is given by:

$$\Delta V_+ = \left[\phi\alpha_{Vo} + (1-\phi)\alpha_{Vp}\right] 2\pi \int_{r_c}^{r_i} \Delta\theta(r) r dr = C_9 I^2 \tag{5.47}$$

$$\begin{gathered} C_9 = \left[\alpha_{vo}\phi + \alpha_{vp}(1-\phi)\right]\left\{\frac{R_{dc}\rho_i}{2}\left[r_c^2 \ln(r_c) - r_i^2 \ln(r_i) + \frac{r_i^2 - r_c^2}{2}\right] + \right. \\ \left. R_{dc}\pi\left(r_i^2 - r_c^2\right)\left[\frac{\rho_i \ln(r_i)}{2\pi} + T_3 + T_4\right]\right\} \end{gathered} \tag{5.48}$$

Where; the temperature integral term in (5.47) is calculated through (5.9).

To represent the effect of pre-existing cavities, the initial dielectric thermal contraction, ΔV_-, due to a temperature difference between the cavity-free temperature, θ_{vf}, and ambient is quantified as:

$$\Delta V_- = \left[\phi\alpha_{Vo} + (1-\phi)\alpha_{Vp}\right]\pi\left(r_i^2 - r_c^2\right)\left(\theta_{amb} - \theta_{vf}\right) = F_7 \tag{5.49}$$

Therefore, to maintain a volumetric equilibrium, the dielectric thermal expansion needs to be compensated by its initial thermal contraction and also the volumetric allowance due to the deformation of both the conductor and sheath, which leads to:

$$\Delta V_{+} + \Delta V_{-} = \{\pi[r_i + u_s(r_i)]^2 - \pi[r_c + u_c(r_c)]^2\} - \left(\pi r_i^2 - \pi r_c^2\right) \tag{5.50}$$

For plane stress analysis, substitute (5.11) (i.e. $u_c(r_c)$), (5.33) (i.e. $u_s(r_i)$), (5.47), (5.49) into (5.50) and assume P_1 equals to P_2 (i.e. uniform pressure), a quadratic equation of P_2 is derived:

Plane stress analysis

$$\begin{aligned}\left(F_5^2 - D_1^2\right) \cdot {P_2}^2 + 2[(r_iF_5 - r_cD_1) + (C_7F_5 - C_1D_1)I^2 + F_5G_1P_3] \cdot P_2 + \Big[(C_7^2 - C_1^2)I^4 + \\ 2\left(r_iC_7 - r_cC_1 - \tfrac{C_9}{2\pi}\right)I^2 + 2C_7G_1P_3I^2 + 2r_iG_1P_3 + G_1^2P_3^2 - \tfrac{F_7}{\pi}\Big] = 0\end{aligned} \tag{5.51}$$

Similarly for plane strain analysis, substitute (5.14) (i.e. $u_c(r_c)$), (5.37) (i.e. $u_s(r_i)$), (5.47), (5.49) into (5.50) and assume P_1 equals to P_2 (i.e. uniform pressure), a quadratic equation of P_2 becomes:

Plane strain analysis

$$\begin{aligned}(F_6^2 - D_2^2) \cdot {P_2}^2 + 2[(r_iF_6 - r_cD_2) + (C_8F_6 - C_2D_2)I^2 + F_6G_2P_3] \cdot P_2 + \Big[(C_8^2 - C_2^2)I^4 + \\ 2\left(r_iC_8 - r_cC_2 - \tfrac{C_9}{2\pi}\right)I^2 + 2C_8G_2P_3I^2 + 2r_iG_2P_3 + G_2^2P_3^2 - \tfrac{F_7}{\pi}\Big] = 0\end{aligned} \tag{5.52}$$

Therefore, P_2 can be calculated for either plane stress analysis or plane strain analysis, by solving the corresponding quadratic equation above. In addition, both radial and circumferential stresses within each cable layer become available with three uniquely defined boundary stresses P_1, P_2 and P_3. As the pre-existing cavities have been considered through (5.49), this analytical pressure calculation is believed applicable to both microscopic and macroscopic cavity creations.

5.3 Mechanical pressure-limited rating and applications

In this sub section, the mechanical pressure-limited rating is derived and demonstrated for the 'high temperature' analysis only. This is because that the determination of the dielectric equivalent mechanical properties (i.e. Young's modulus, Poisson's ratio) under the 'low temperature' analysis requires extra lab experiment designs (e.g. tensile test), which is out of the scope of this thesis.

5.3.1 Mechanical pressure-limited rating derivation

To link the two cavity creation mechanisms and quantify the correlated effect on cable rating calculations, 'cavity creation threshold' is introduced to develop the so-called mechanical pressure-limited rating.

According to the microscopic cavity creation mechanism, the reoccurrence of pre-existing cavities becomes significant when the dielectric pressure drops to a certain level, P_{cct} (due to impregnant contraction under cable cooling). Therefore, by setting P_2 equal to P_{cct}, the mechanical pressure-limited rating has its minimum value as:

Plane stress analysis

$$I_{pressure} = f_1^{-1}(P_{cct}, P_3) \tag{5.53}$$

Plane strain analysis

$$I_{pressure} = f_2^{-1}(P_{cct}, P_3) \tag{5.54}$$

It is suggested that this minimum rating reflects a critical moment during cable cooling when the dielectric breakdown becomes more likely to occur, due to the cavity reoccurrence. Note that the value of P_{cct} varies from manufacturer to manufacturer based on specific dielectric designs, which is out of the scope of this thesis. However, the future work on identifying P_{cct} is stated in Chapter 7.

According to the macroscopic cavity creation mechanism, the cavity creation threshold effectively refers to the yield of the metallic sheath. As aluminium and lead are ductile materials, Tresca's (maximum shear stress) yield criterion is well recognized [160]. Under Tresca's criterion, yield is caused by the slippage of crystal planes along the maximum shear stress surface and it can be quantified by a uniaxial tensile test. Mathematically, it requires the maximum shear stress to be less than the yield stress. Normally, the maximum shear stress in the complex 3D stress system is defined as the maximum stress difference between any two of the three principal stresses (i.e. σ_θ, σ_r, and σ_r), depending on the relative values and signs. As σ_θ and σ_r normally have opposite signs (Poisson's effect) and σ_z has its magnitude in between according to (2.63), the maximum shear stress is calculated between σ_θ and σ_r.

.

$$|\sigma_\theta - \sigma_r| \leq \sigma_y \tag{5.55}$$

Where; plastic deformation occurs above the material yield stress σ_y [N.m^{-2}]. For an annulus under plane stress analysis, substituting the radial stress expression (5.4) and circumferential stress expression (5.5) into (5.55) gives:

Plane stress analysis

$$\left|\frac{1}{r^2}\left\{\alpha_L E I^2 R_{dc} r_{ai}^2 \left[\frac{\rho}{2\pi}\ln\left(\frac{r_{ai}}{r_{ao}}\right) - \frac{\rho}{4\pi} - T_{total}\right] + \frac{2EK_2}{1+v}\right\} + \frac{\alpha_L E I^2 R_{dc}\rho}{4\pi}\right| \leq \sigma_y \tag{5.56}$$

Similarly, for an annulus under plane strain analysis, substituting the radial stress expression (5.7) and circumferential stress expression (5.8) into (5.55) gives:

Plane strain analysis

$$\left|\frac{1}{r^2}\left\{\frac{\alpha_L E I^2 R_{dc} r_{ai}^2}{1-v} \left[\frac{\rho}{2\pi}\ln\left(\frac{r_{ai}}{r_{ao}}\right) - \frac{\rho}{4\pi} - T_{total}\right] + \frac{2EK_2}{1+v}\right\} + \frac{\alpha_L E I^2 R\rho}{4\pi(1-v)}\right| \leq \sigma_y \tag{5.57}$$

From (5.56) and (5.57), the maximum sheath stress is found to be at the annulus inner radius $r = r_{ai}$. Therefore, for the sheath layer, applying -P_2 at sheath inner radius ($r = r_i$) from (5.51) and -P_3 at sheath outer radius ($r = r_s$) to (5.4) as the boundary conditions, K_2 in (5.56) can be identified. Substitute this K_2 into (5.56) and rearrange the equation at sheath inner radius r_i, for cable loading I, the mechanical pressure-limited rating under plane stress analysis has its maximum value as:

Plane stress analysis

$$I_{pressure} = \sqrt{\frac{(1+v_s)r_i^2\sigma_y - 2E_sK_2}{(1+v_s)r_i^2\alpha_{Ls}E_sR_{dc}\left[\frac{\rho_s}{2\pi}\ln\left(\frac{r_i}{r_s}\right) - T_3 - T_4\right]}} \tag{5.58}$$

$$\begin{aligned} K_2 = \frac{r_i^2 r_s^2}{(1-v_s)(r_i^2-r_s^2)} \langle \left(\frac{v_s^2-1}{E_s}\right) P_2 - \{ \frac{(1-v_s^2)\alpha_{Ls}R_{dc}\rho_s}{4\pi r_s^2}\left[r_i^2\ln(r_i) - r_s^2\ln(r_s) + \frac{r_s^2-r_i^2}{2}\right] + \\ \frac{(1-v_s^2)\alpha_{Ls}R_{dc}}{2r_s^2}\left(r_s^2 - r_i^2\right)\left[\frac{\rho_s\ln(r_s)}{2\pi} + T_3 + T_4\right] \} I^2 + \frac{1-v_s^2}{E_s}P_3 \rangle \end{aligned} \tag{5.59}$$

Similarly, applying -P_2 at sheath inner radius ($r = r_i$) from (5.52) and -P_3 at sheath outer radius ($r = r_s$) to (5.7) as the boundary conditions, K_2 in (5.57) can be identified. Substitute this K_2 into (5.57) and rearrange the equation at sheath inner radius r_i, for cable loading I, the mechanical pressure-limited rating under plane strain analysis has its maximum value as:

Plane strain analysis

$$I_{pressure} = \sqrt{\frac{(1+v_s)r_i^2\sigma_y - 2E_sK_2}{\frac{1+v_s}{1-v_s}r_i^2\alpha_{Ls}E_sR_{dc}\left[\frac{\rho_s}{2\pi}\ln\left(\frac{r_i}{r_s}\right) - T_3 - T_4\right]}} \tag{5.60}$$

$$\begin{aligned} K_2 = \frac{r_i^2 r_s^2}{r_i^2-r_s^2} \langle \left(-\frac{1+v_s}{E_s}\right) P_2 - \{ \frac{(1+v_s)\alpha_{Ls}R_{dc}\rho_s}{(1-v_s)4\pi r_s^2}\left[r_i^2\ln(r_i) - r_s^2\ln(r_s) + \frac{r_s^2-r_i^2}{2}\right] + \\ \frac{(1+v_s)\alpha_{Ls}R_{dc}}{(1-v_s)2r_s^2}\left(r_s^2 - r_i^2\right)\left[\frac{\rho_s\ln(r_s)}{2\pi} + T_3 + T_4\right] \} I^2 + \frac{1+v_s}{E_s}P_3 \rangle \end{aligned} \tag{5.61}$$

Where; E_s is the sheath Young's modulus [N.m^{-2}], v_s the sheath Poisson's ratio, α_{Ls} the sheath linear thermal expansion coefficient [℃$^{-1}$], ρ_s the sheath thermal resistivity [K.m.W^{-1}], T_3 the cable serving thermal resistance [K.W^{-1}], and T_4 is the ambient environment thermal resistance [K.W^{-1}]. Note that as the current loading, I, appears on the right hand side of (5.58) and (5.60), through the dependency in K_2, an iterative solution is required.

5.3.2 Mechanical pressure-limited rating application

In this part, a full application of (5.60) is presented to demonstrate the relationship between the two cavity creation mechanisms and their correlated effect on cable ratings. To start with, the nominal directly buried land HVDC cable is assumed monopole with parameters and installation environment summarized in Table 3.2 (D_i = 103mm) and Table 3.3 (1m burial depth and 12℃ ambient temperature) respectively to simulate the real practice. The overall layout and boundary condition settings are shown in Figure 3.2 and Figure 3.3. Before conducting the tests, a brief rating comparison between plane stress analysis and plane strain analysis is plotted in Figure 5.2 below.

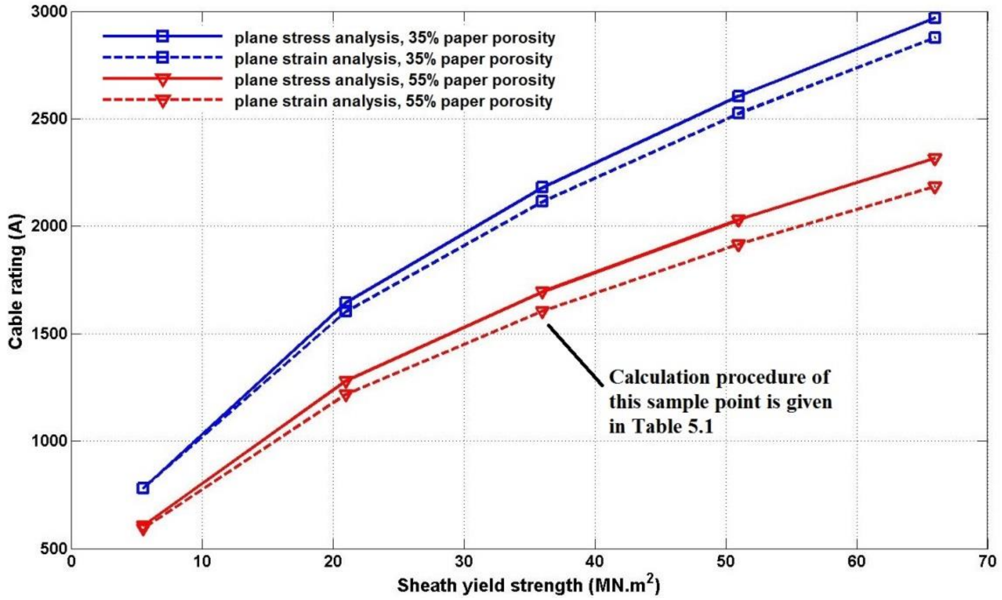

Calculation procedure of this sample point is given in Table 5.1

Figure 5.2: Cable rating plot against various yield stresses and paper porosities

From Figure 5.2, it can be seen that the plane strain analysis generally gives a more conservative solution compared to the plane stress analysis (up to 6% rating difference at higher sheath yield strengths). A possible explanation of the difference is that when an infinitesimal element is subject to a vertical stress (z-direction), it has a tendency to get either elongated or shortened vertically. However, as all the neighbouring elements simultaneously show the same tendency, an extra resistive stress (either tension or contraction in x-y surface) develops called ‘constraint effect’ [161]. Therefore, together with the original radial and circumferential stresses, the resultant stress distribution under plane strain analysis has three elements to consider, rather than the two under plane stress analysis. Moreover, as all the cables examined in this thesis are fully buried, the plane strain analysis is more appropriate because the longitudinal cable movement is largely constrained by ambient backfill friction. Therefore, the equations for plane strain analysis are applied to the test cases which follow.

Table 5.1 below summarizes the calculation procedure of the sample point in Figure 5.2.

Table 5.1: Sample point calculation procedure

First level constants (Cable parameter)							
r_c	3.025×10^{-2}	r_i	5.15×10^{-2}	r_s	5.55×10^{-2}	R_{dc}	7.71×10^{-6}
T_1	0.5081	T_2	0	T_3	0.0434	T_4	0.67
E_c	1.25×10^{11}	E_s	1.6×10^{10}	ν_c	0.35	ν_s	0.44
α_{Lc}	1.7×10^{-5}	α_{Ls}	2.9×10^{-5}	α_{Vo}	6.4×10^{-4}	α_{Vp}	1.92×10^{-5}
ρ_c	2.5×10^{-3}	ρ_i	6	ρ_s	2.83×10^{-2}	P_3	1×10^{6}
ϕ	0.55	θ_{amb}	12	θ_{vf}	12	σ_y	3.6×10^{7}
Second level calculation (Cable internal pressure)							
C_2	6.54×10^{-12}	C_8	1.18×10^{-11}	C_9	1.4×10^{-11}	D_2	-9.8×10^{-14}
F_6	3.68×10^{-11}	F_7	0	G_2	-3.74×10^{-11}	P_2	3.5×10^{6}
Third level calculation (Cable mechanical pressure-limited rating)							
K_2	5.7×10^{-6}	$I_{pressure}$	1611				

Note that all the parameters are defined in 'Symbols and Abbreviations' and have been presented in SI unit form for the sample calculation. Based on the calculation results in Table 5.1, both (5.38) and (5.52) are simplified as follows, by comparing the power order of each equation component.

$$C_8 = r_i(1 + v_s)\alpha_{Ls}R_{dc}(T_3 + T_4) \tag{5.62}$$

$$F_6^2 \cdot P_2{}^2 + 2r_iF_6 \cdot P_2 + \left[2\left(r_iC_8 - r_cC_2 - \frac{C_9}{2\pi}\right)I^2 + 2r_iG_2P_3 - \frac{F_7}{\pi}\right] = 0 \tag{5.63}$$

By applying the above simplifications, the sample calculation is repeated and shown in Table 5.2.

Table 5.2: Simplified calculation procedure

Second level calculation (Cable internal pressure)							
C_2	6.54×10^{-12}	C_8	1.18×10^{-11}	C_9	1.4×10^{-11}	D_2	-9.8×10^{-14}
F_6	3.68×10^{-11}	F_7	0	G_2	-3.74×10^{-11}	P_2	3.5×10^{6}
Third level calculation (Cable mechanical pressure-limited rating)							
K_2	5.7×10^{-6}	$I_{pressure}$	1610				

Through a comparison between Table 5.2 and Table 5.1, it can be seen that the final mechanical pressure-limited rating generally remains the same despite the largely reduced equation complexity. Therefore, the simplifications are applied to all of the remaining tests in this chapter.

To examine the effect of cable properties on rating calculations, two types of parameters are tested:

- Intrinsic parameters: paper porosity, sheath yield stress
- Extrinsic parameters: burial depth, cavity-free temperature

It is suggested that the intrinsic parameter test can provide useful information for cable designs in terms of fundamental material properties, and the extrinsic parameter test will examine the relationship between the two cavity creation mechanisms because the cavity-free temperature, θ_{vf}, determines the creation of pre-existing cavity.

For the intrinsic parameter test, Kraft paper porosity is varied from 0.35 to 0.55 based on the density ratio between the paper product and pure fibre. The sheath yield stress is varied from 5.5 MN.m^{-2} (pure lead) to 66 MN.m^{-2} (lead alloy) [162]. Further, a nominal burial depth of 1000mm is assumed and the cable has a cavity-free temperature of 12℃ (i.e. no pre-existing cavities). The current rating is thus plotted against the yield strength under various paper porosities in Figure 5.3 with data presented in Table 5.3.

Table 5.3: Pressure-limited rating test (A) on paper porosity and sheath yield strength

σ_y \ ϕ	35%	40%	45%	50%	55%
5.5 MPa	807	742	691	649	614
21 MPa	1612	1482	1380	1296	1225
36 MPa	2117	1947	1812	1702	1610
51 MPa	2524	2321	2160	2029	1919
66 MPa	2874	2642	2459	2310	2184

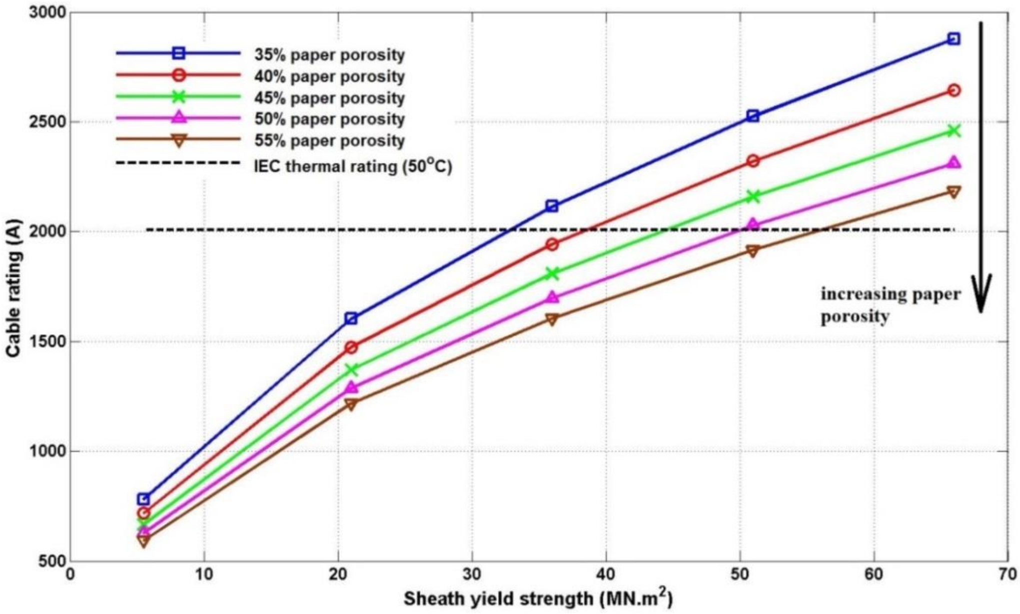

Figure 5.3: Pressure-limited rating plot against various yield stresses and paper porosities

In Figure 5.3, it is clear to see that the mechanical pressure-limited rating increases with increasing sheath yield strength, but decreases with increasing paper porosity. This is reasonable because enhancing yield stress and reducing paper porosity both effectively increase the thermal expansion allowance per unit impregnant volume. In addition, Figure 5.3 shows that a significant part of the curves are below the IEC thermal-limited rating reference, which implies that for those cases, the rating limiting factor is the mechanical yield rather than the normal thermal constraint. As cable manufacturers tend to use lead alloy for a better mechanical property instead of pure lead, an average sheath yield stress of 36 MN.m^{-2} was chosen for the rest of tests.

For the extrinsic parameter test, the sheath yield strength is set at 36 MN.m^{-2}. The burial depth firstly varies from 500mm to 4000mm with a cavity-free temperature equal to the ambient of 12 ℃ (i.e. no pre-existing cavities). The result is shown in Figure 5.4 with data in Table 5.4.

Table 5.4: Pressure-limited rating test (A) on paper porosity and burial depth

L ***ϕ***	35%	40%	45%	50%	55%
0.5m	2248	2073	1933	1819	1722
1m	2118	1947	1812	1702	1610
1.5m	2051	1884	1752	1644	1554
2m	2008	1842	1712	1606	1517
3m	1951	1788	1660	1557	1470
4m	1914	1753	1627	1524	1439

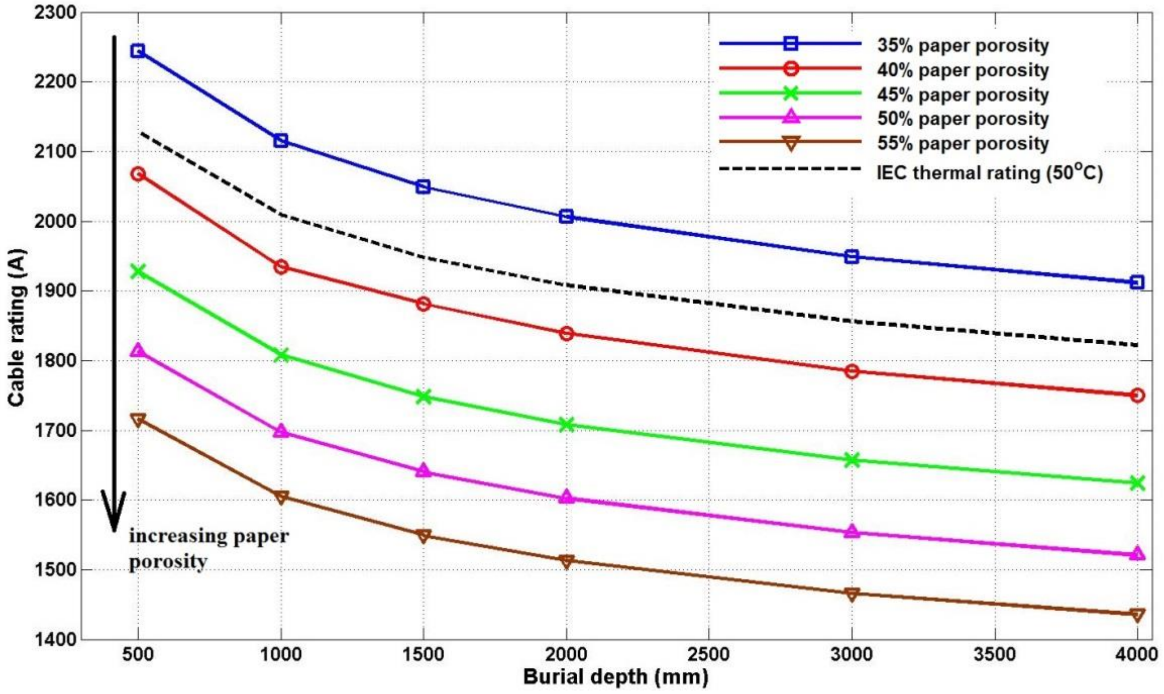

Figure 5.4: Pressure-limited rating plot against various burial depths and paper porosities

In Figure 5.4, it is found that the mechanical pressure-limited rating drops with increasing burial depth. A possible explanation is that as the equivalent ambient thermal resistance, T_4, increases with an increasing burial depth, a bigger temperature rise results for the same current loading (compared to the load-off isothermal temperature profile). In other words, greater dielectric thermal expansion is induced by the same amount of loading change. Therefore, with a limited thermal expansion allowance, the mechanical pressure-limited rating drops. In addition, it is observed that changing the burial depth has a big effect on ratings (up to 12% rating variation compared to the mean value), which is almost comparable to the effect from paper porosity (14% rating variation). Similar to Figure 5.3, a large part of the curves are below the IEC thermal-limited rating, which is of concern.

Finally, the mechanical pressure-limited rating is tested against the cavity-free temperature, θ_{vf}, which varies from 12 ℃ to 28 ℃, with burial depth of its nominal value of 1000mm. Results are shown in Figure 5.5 with data presented in Table 5.5.

Table 5.5: Pressure-limited rating test (A) on paper porosity and cavity-free temperature

θ_{vf} \ ϕ	35%	40%	45%	50%	55%
12	2118	1947	1812	1702	1610
16	2299	2134	2005	1901	1814
20	2468	2307	2182	2082	1999
24	2627	2469	2347	2249	2169
28	2778	2622	2502	2406	2328

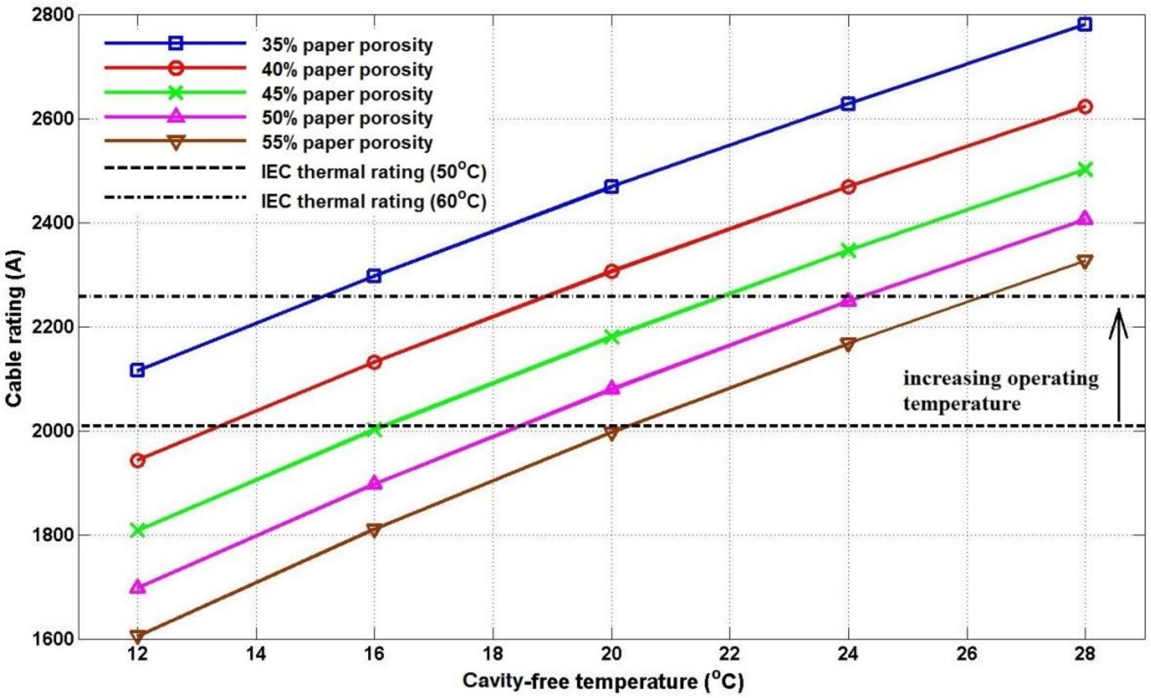

Figure 5.5: Pressure-limited rating against various cavity-free temperatures

In Figure 5.5, it is clear that the mechanical-pressure limited rating decreases with dropping cavity-free temperature as expected. It verifies the previous analyses that as manufacturers aim to eliminate pre-existing cavities in insulation (equivalent to reducing the cavity-free temperature), the dielectric free expansion allowance is also reduced. Therefore, the microscopic cavity creation becomes weaker while the macroscopic cavity creation becomes dominant. For cable ratings, this relationship is reflected by the part of curves below the IEC thermal-limited rating reference, in the lower left corner of Figure 5.5.

Practically speaking, the IEC60287 thermal-limited rating is still widely applicable because the majority of the curves in Figure 5.5 remain above the thermal-limited rating of 50 ℃. This means that the maximum temperature will be the major limiting factor for those cases. However, for future cable designs with an increased maximum operating temperature, e.g. 60 ℃, the mechanical pressure-limited rating is more likely to be lower than the normal IEC thermal-limited rating. In addition, for practical operation with an escalated local ambient temperature such as cable crossings, the free expansion allowance is effectively reduced and the mechanical pressure-limited rating can be more demanding.

5.4 Summary

This chapter presents the analytical calculation of cable internal pressure under various conditions (plane stress/ strain, low/ high temperature), which requires a combination between various physics: electrical circuit theory, thermodynamics and theory of elasticity. It is believed that the developed calculation is applicable to both the microscopic and macroscopic cavity creation mechanisms.

In addition, a novel mechanical pressure-limited rating method is proposed, with the two mechanisms together specifying the upper and lower boundaries of this rating. Throughout the application of the mechanical pressure-limited rating, a correlated effect from the two cavity creation mechanisms on MI-type HVDC cable rating is demonstrated. It has been proved that releasing the constraint from one mechanism will enhance any constraint due to the other one.

Practically speaking, to avoid rating limitation, it is suggested to shallow bury the cable where possible and select designs with high sheath yield strength and low paper porosity, where the normal IEC thermal-limited rating calculation can still hold. However, it is strongly advised to calculate the mechanical pressure-limited rating for modern MI-type HVDC cables with low dielectric pre-existing cavities and higher operating temperatures.

Chapter 6

HVDC Cable Crossing Ratings

With the growing complexity of underground cable systems, cable crossings are inevitably found in power transmission and distribution (T&D) networks. It is critical to accurately rate such cables because dangerously high temperatures can occur at crossing points, resulting in premature ageing of the cable insulation and potentially a catastrophic failure.

At present, the rating method widely recognized for cable crossings is IEC60287-3-3 [33] (Equation (2.73) on Page 36), which assumes an isothermal ground surface condition and homogeneous backfill thermal resistivity. Although these assumptions have already been shown to affect the accuracy of IEC60287-1-1 rating calculations for directly buried cables [83], less consideration has been given to cable crossings. In addition, for most submarine cable crossings protected by a rock berm, IEC60287-3-3 is inapplicable due to a failure of the 'image' theory, i.e. rock berm raised on seafloor.

Therefore, this chapter develops a numerical modelling method to evaluate high voltage cable crossing ratings. Firstly, the impact of idealistic assumptions within the IEC calculation is examined through HVAC cable crossings on land. Subsequent, the developed modelling method is extended to submarine HVDC cable crossings to demonstrate its broad applicability, where the IEC method doesn't apply.

6.1 Cable crossing on land

Many conventional land buried transmission cables operate under ac voltages and use XLPE insulation, which benefits from a high operating temperature (90 ℃) and controllability (i.e. circuit breaker). To compare the numerical modelling method to IEC60287-3-3, it is better to present testing results in terms of cable rating rather than temperature. Therefore, a numerical modelling procedure for rating cable crossings is firstly suggested. Note that as the purpose of Section 6.1 is to benchmark the applicability of FEA modelling through a comparison to IEC calculation, only the thermal rating is considered.

6.1.1 Numerical modelling procedure for rating cable crossings

The suggested numerical modelling procedure for rating the cable crossings requires the building of a 3D model and the application of a range of possible de-rating factor (DF) combinations. Subsequently, the optimum solution is interpolated where both crossing cable circuits are operating at their maximum permissible temperatures.

To build the land cable crossing model, general FEA modelling techniques in Section 3.3 are used and expanded into a full-scale 3D model as follows in Figure 6.1.

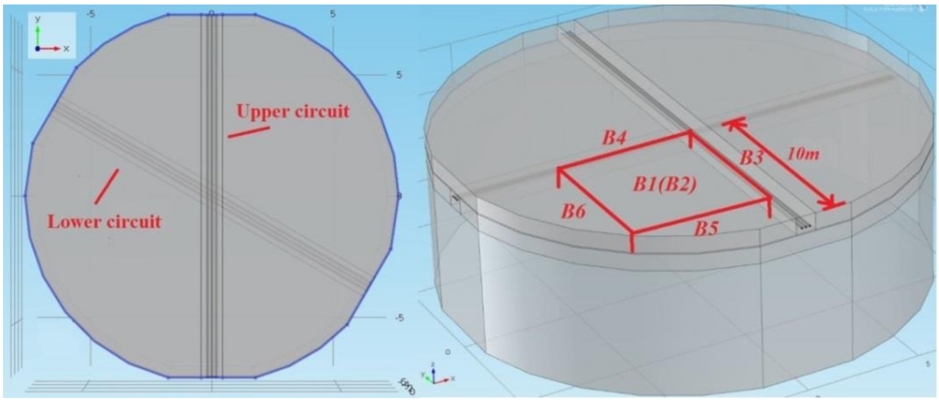

Figure 6.1: Geometric outline of a 3D land cable crossing

In Figure 6.1, the key parameter is the cable length which implicitly determines the overall size of the backfill box. Therefore, a test on the minimum half cable length is conducted in Figure 6.2.

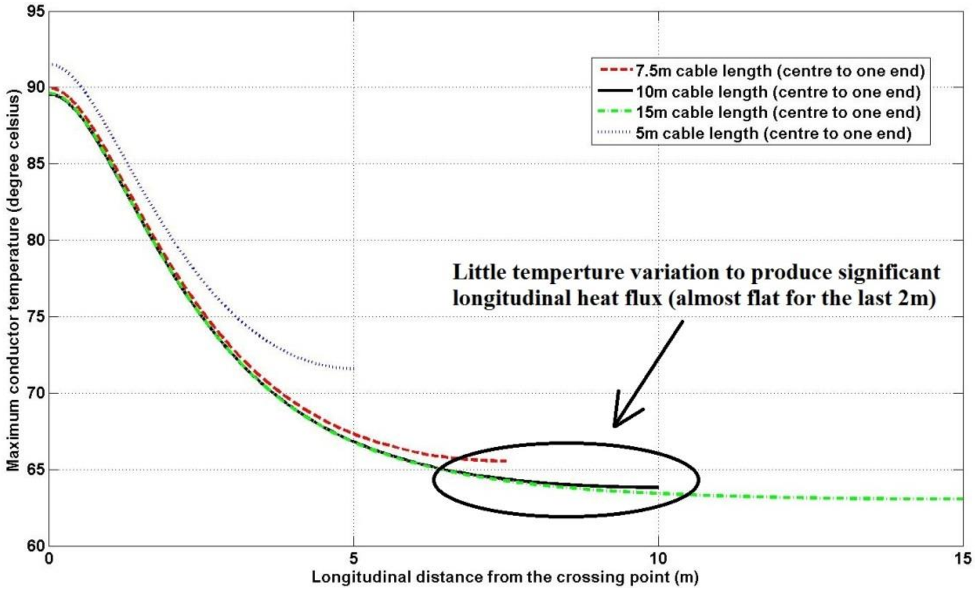

Figure 6.2: Longitudinal conductor temperature plot for various cable lengths

From Figure 6.2, it is suggested that a minimum half cable length of 10m is adequate to support a thermal insulation condition at cable ends and suggest a maximum temperature offset less than 0.5 ℃ at the crossing point (compared to the 15m one).

For the boundary condition setting, the ground boundary B1 is either isothermal or thermal convective defined in (2.69). Normally for the full-scale model with a cylindrical backfill box, the cylinder wall is thermal insulating. Once two circuits are crossing at 90 °, only a quarter model (red frame in Figure 6.1) is built due to two symmetric planes along x and y axis respectively. Therefore, boundaries B5/ B6 are defined as thermal insulating, and B3/ B4 are defined as thermal symmetric (Equation (3.11)). For the bottom boundary B2, a distributed temperature calculation is performed using (3.12) and Figure 6.3 illustrates its application.

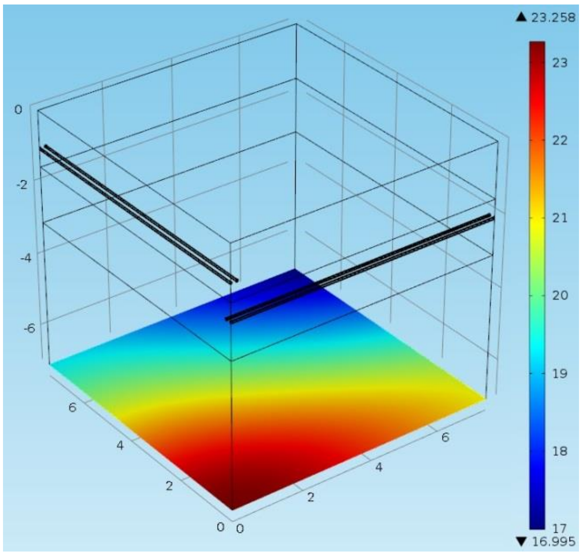

Figure 6.3: Illustration of the bottom boundary temperature distribution

To mesh the 3D crossing model, special technique (i.e. sweep meshing along the cable length) is applied which effectively prevents an excessive mesh insertion. The technique is demonstrated in Figure 6.4 below.

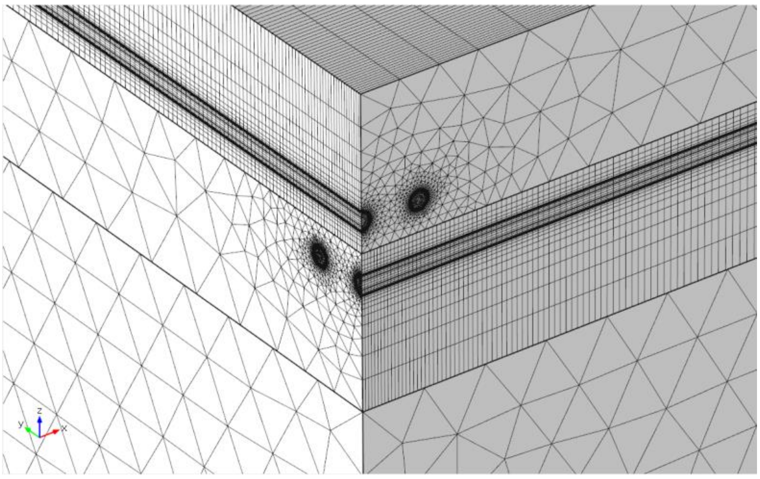

Figure 6.4: Illustration of the meshing strategy

In Figure 6.4, the whole model has been vertically divided into three layers with distinct meshing strategies applied to different layers. The bottom vast backfill box adopts free tetrahedron mesh and the top two layers adopt 2D surface triangle meshing swept along the cable length. Note that the identity pair option is enabled, through interpolation, to allow discontinuous mesh across two overlapping boundaries in different connecting parts of an assembly [140]. Further, the space between two adjacent sweep layers follows a geometric progression to have a higher layer separation towards the cable end (i.e. 120 total layers with an element growing ratio of 5, illustrated in Figure 6.4). This is possible due to a decreasing longitudinal temperature gradient away from the crossing point. Overall, applying this approach prevents excessive mesh density, which is important in ensuring a computationally efficient model. Once the model is built and solved, the optimum solution is interpolated, as shown in Figure 6.5 below.

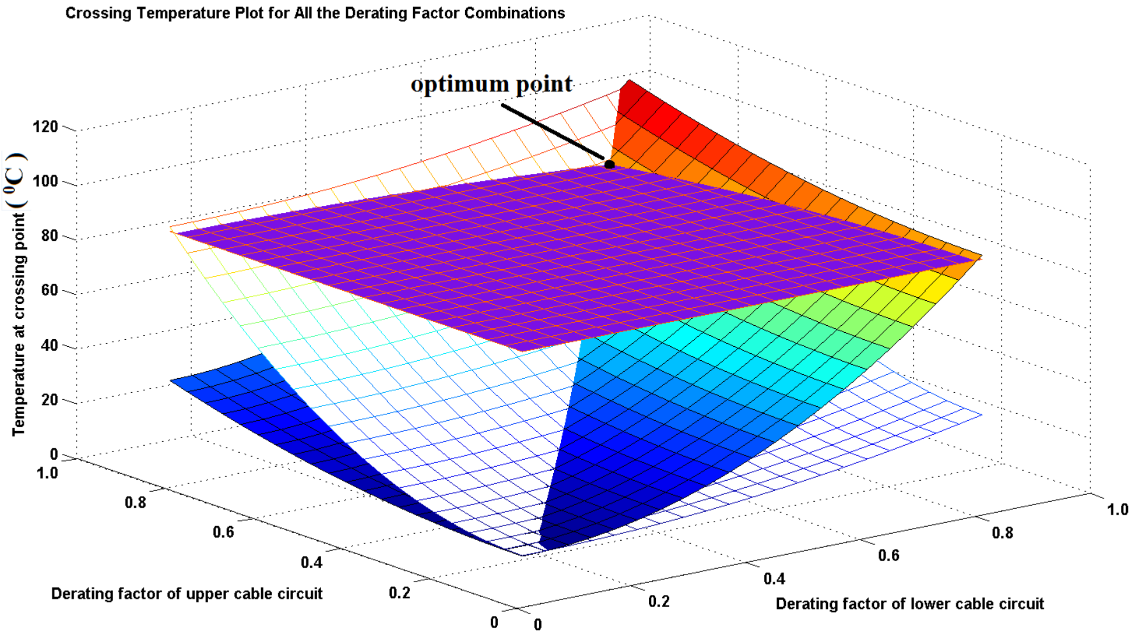

Figure 6.5: Demonstration of numerical procedure for de-rating factor calculation

In Figure 6.5, a total of 441 DF combinations are solved with each DF value stepping from 0 to 1 in 0.1 interval. The curved surface plot (filled) represents the temperature of the lower cable at the crossing point, whilst the curved mesh plot (unfilled) represents the upper central cable. The purple flat surface plot is 90^{0}C isothermal and the intersection of these three surfaces is the optimum point. In addition, Figure 6.5 demonstrates that only one optimum DF combination allows both cables to operate at their maximum permissible temperature, which agrees with the result uniqueness of IEC60287.

The general numerical modelling procedure to calculate the de-rated crossing rating is:

Step 1. Build 3D FEA model with specified conditions in Comsol
Step 2. Export model into .m file which can be amended in Matlab
Step 3. Add loop function into the .m file for DF value sweep
Step 4. Run the .m file through Matlab Livelink and record data at crossing point
Step 5. Analyse temperature data and interpolate the optimum DF combination

Note that this procedure relies upon a reasonable range being specified for the de-rating factors. In other words, choosing a small range around the optimum point greatly reduces the number of iterations required. However, if the optimum point does not fall within the range specified, the calculation of the de-rating factor will fail. In general, adding more points to the interpolation leads to a more accurate result, but at the expense of greater computational time.

6.1.2 Test and analysis

In this sub section, full details of all the steady state FEA tests are presented and the implications of the results are discussed. The parameters of the land HVAC three-phase XLPE cable circuit and ambient environment are described in Table 3.1 and Table 3.3. In order to determine the impact of idealistic assumptions within the IEC calculation, 3 key aspects are examined:

1. Ground surface boundary condition, burial depth and vertical spacing
2. Backfill thermal condition (wet/ drying-out)
3. Cable circuit phase spacing/ crossing angle

The above 3 aspects are assumed to potentially affect the calculation accuracy of IEC60287-3-3. In detail, ratings are calculated from both the IEC method and the FEA modelling and subsequently compared with each other for a discussion. In Table 6.1 below, the testing conditions are briefly summarised.

Table 6.1: Condition summary for steady state tests

	Backfill	Phase spacing (mm)	Crossing angle (^{0})
Test 1	wet	170	90
Test 2	partial dry-out	170	90
Test 3	partial dry-out	170/310/450/590	90
Test 4	partial dry-out	170	60/70/80/90

1) Ground condition/ burial depth and vertical spacing

As previous research has shown that the ground surface condition can strongly affect the rating calculation for single buried cable [83], it is necessary to examine its impact on the crossing rating and to see how it changes with different circuit installation layouts. Therefore, Figure 6.6 and Figure 6.7 below plot the cable thermal ratings when both circuits are either shallow or deeply buried (U = upper circuit, L = lower circuit).

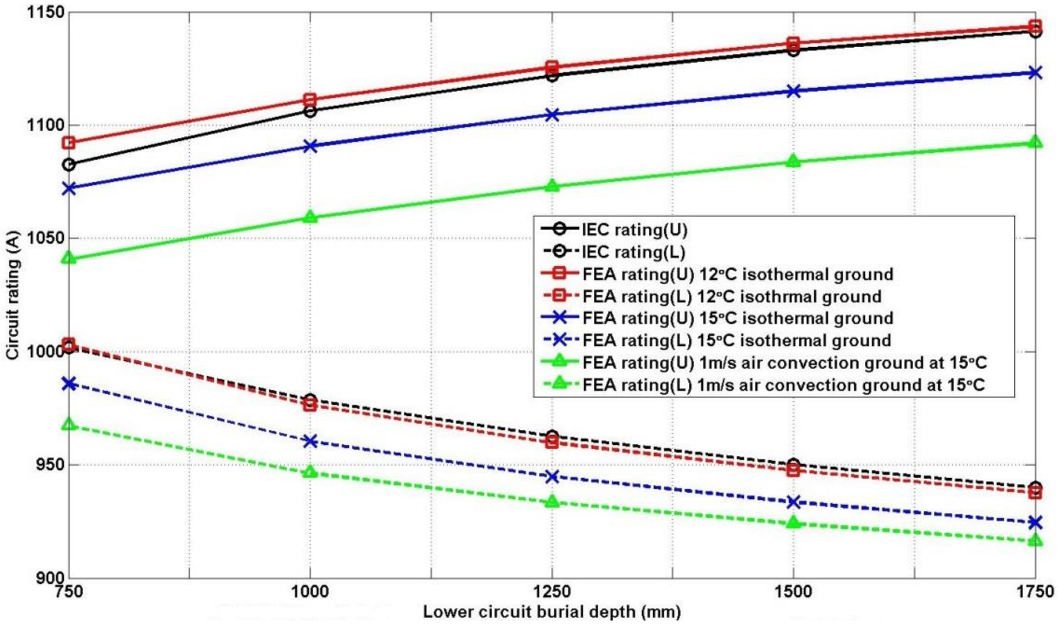

Figure 6.6: Ratings under various ground boundary conditions (500mm upper cable burial depth)

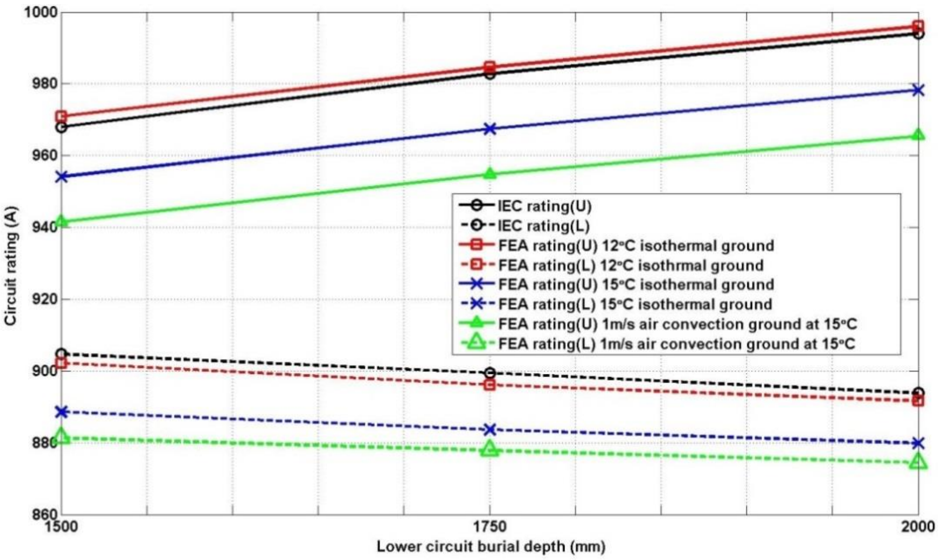

Figure 6.7: Ratings under various ground boundary conditions (1000mm upper cable burial depth)

The results of Figure 6.6 and Figure 6.7 imply that the isothermal ground boundary condition can impose a strong effect on the crossing rating. For instance, the IEC method overrates the crossing by 30A compared to the FEA modelling (3.5% of the FEA rating) when an air convective ground condition is presented. Although this rating difference between IEC and FEA solutions becomes smaller with increased circuit burial depth and vertical spacing, the effect of ground surface condition still cannot be fully mitigated.

2) Wet/ drying-out backfill

The second part examines the effect of backfill thermal resistivity on the cable crossing rating. In IEC60287-3-3, homogeneous backfill is assumed with a constant thermal resistivity, in order to simplify both the internal (i.e. cable - cable) and external (i.e. crossing - ambient) heat transfers. However, previous work has shown that an accurate rating solution requires careful modelling of wet and dry backfill regions [87]. Therefore, Figure 6.8 shows the rating plot with partial drying-out of the backfill. Note that the upper circuit is buried at 500mm.

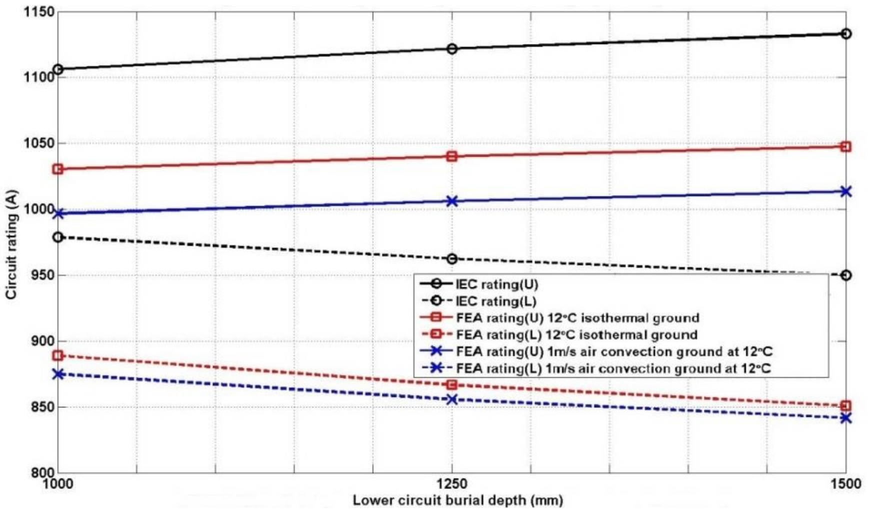

Figure 6.8: Ratings under various ground boundary conditions with partial drying-out backfill

By comparing Figure 6.8 to Figure 6.6, it is shown that the crossing rating changes considerably when the backfill partial drying-out is included. Under a 12^0C isothermal ground boundary, the IEC60287-3-3 overrates the crossings by 70A compared to FEA modelling (7% of the FEA solution). More dangerously, this increases to 110A (11% of the FEA solution) under an air convection ground surface boundary.

In some cases, backfill partial drying out can have an even bigger impact on the solution than the ground condition (e.g. deeply buried crossing), because several dry regions may merge together which leads to poor heat dissipation around the crossing point. Figure 6.9 indicates a merged drying out region.

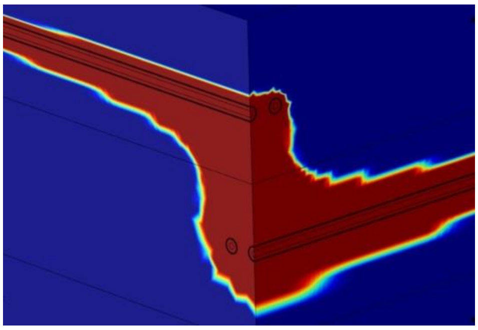

Figure 6.9: Backfill partial drying-out region distribution (inner red region has ρ_{dry} = 3 K.m.W^{-1} and outer blue region has ρ_{wet} = 1.2 K.m.W^{-1})

3) Cable circuit phase spacing/ crossing angle

According to IEC60287-3-3, bigger phase (core-to-core) spacing leads to an increased rating, by mitigating the mutual heating effect. To numerically verify this, Figure 6.10 plots the current rating as a function of phase spacing for both upper and lower circuits. Note that the burial depths of the upper and the lower circuits are 500mm and 1000mm respectively.

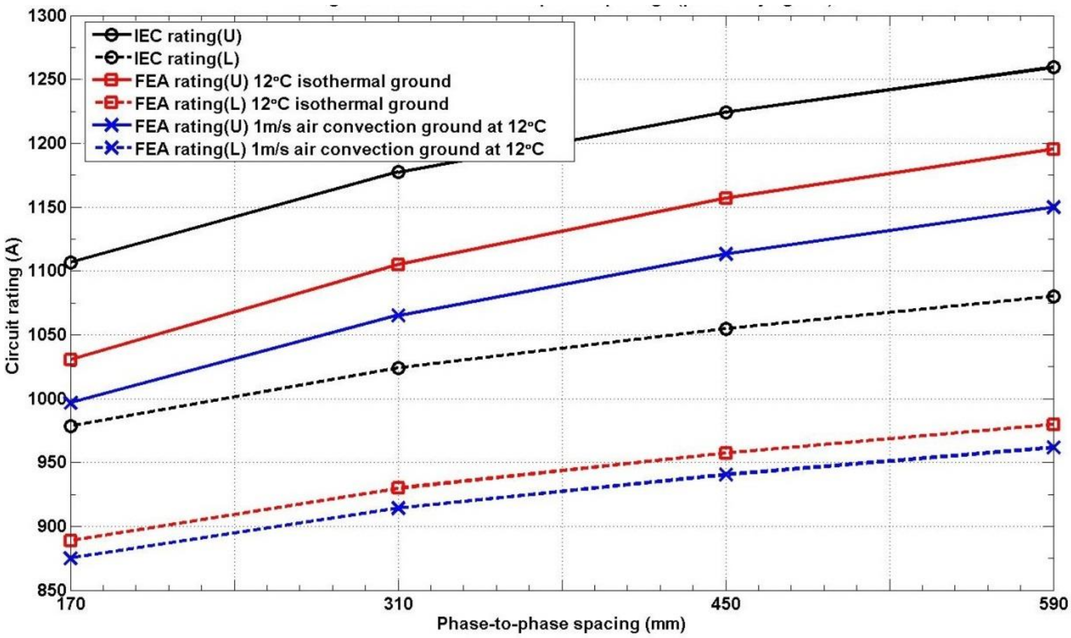

Figure 6.10: Ratings under various ground conditions and phase spacings

In Figure 6.10, both the IEC and FEA calculations show a very similar trend of rating variation against various phase spacings, which verifies that an increased rating is obtained with bigger phase spacing. In addition, the phase spacing is not the main reason causing a rating difference between the two comparing calculations. In fact, it is the various ground surface conditions that leads to the rating offset.

In general, cable crossings are preferred to be installed at right angle to minimize the mutual heating. However, due to practical limitations, cables crossing at other angles are inevitable and it is necessary to examine its effect on the rating calculation. Note that the upper and the lower circuits are buried at 500mm and 1000mm respectively. In Figure 6.11 below, circuit rating is plotted against various crossing angles.

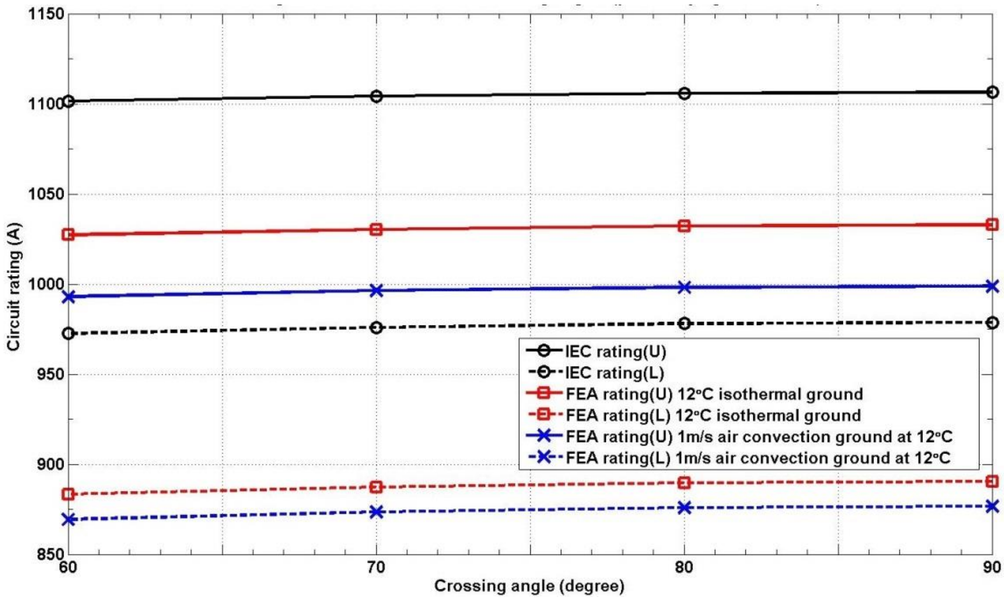

Figure 6.11: Ratings under various ground conditions and crossing angles

In Figure 6.11, both the IEC and FEA calculations indicate very little rating variation (< 10A, 1% of the IEC rating) against various crossing angles from 60° to 90°. Similar to Figure 6.10, the main reason causing a rating difference between two comparing calculations is the ground surface condition. Practically speaking, little rating loss is observed from the change of crossing angle, which may be safely neglected provided it is in the region of 60^0 to 90^0.

In a short summary, these tests reveal that the ground surface and the backfill thermal resistivity assumptions in IEC60287-3-3 strongly affect the crossing rating calculation. The use of an FEA numerical modelling method is particularly beneficial where the crossing is shallowly buried and partial drying of the surrounding backfill is likely to occur. Also it has been shown that the crossing angle has little effect on rating calculation, which gives much flexibility to cable installations in field.

6.2 Submarine cable crossing

In this section, the developed FEA numerical modelling method is extended to evaluate submarine HVDC cable crossing ratings. In general, it is taken for granted that no extra rating considerations are required for submarine HVDC cable crossings because dc cables produce much less heat losses than ac cables (e.g. negligible dielectric and sheath losses). Moreover, the low subsea ambient temperature and low-thermal-resistivity surrounding backfill are assumed to effectively take away the mutual heat generated at the crossing point. Finally, no backfill drying out is expected as a ready supply of water exists and the maximum cable temperature is below 50 ℃ (for the mass impregnated paper insulated cables).

However, based on the work presented in this thesis, practical situations can be much more complicated because it is actually either the maximum dielectric stress or cable internal pressure that limits the submarine dc cable rating rather than the normal thermal constraint. A closer examination of submarine cable crossing designs reveals that practical crossing installations heavily depend on both local seabed configurations and cable protection requirements. In some cases, two layers of different material are used to vertically separate the crossing circuits [94], which leave the assumption of effective mutual heat removal in doubt. Therefore, to examine all the uncertainties above, the developed 3D FEA numerical modelling method will be applied to evaluate the submarine HVDC cable crossing ratings under various crossing installations.

6.2.1 Submarine HVDC cable crossing installation/ demonstration

When designing submarine cable crossings, the possibility of thermal interference between two crossing cables is under consideration but with little detailed guidelines in the literature. In [90], a minimum vertical separation of 30cm - 45cm is believed adequate to minimize the thermal interference, and larger separation designs are normally unfavourable due to installation difficulties.

When installing submarine cable crossings, a combined strategy of rock placement and concrete mattress laying is normally adopted for the best mechanical protection. The vertical separation is achieved by pre-installing concrete mattress over the existing circuit. After laying the new circuit, a rock placement is deployed and covers the whole geometry as an overall protection. This is a preferred method as the separation is guaranteed if the mattresses are correctly placed, and the new cable is laid on target. Based on the following common design criteria, four proposed crossing installations have been modelled and studied.

- Submarine cable burial depth is normally between 0.5m and 2m, reaching a BPI (Burial Protection Index) requirement of 1 for most seabed types.
- A minimum vertical separation is between 30cm to 45cm, applying to most pipeline/ pipeline, pipeline/ cable and cable/ cable crossings [90].

- Concrete mattress is the most commonly used separation medium with a typical thickness varying from 150mm to 450mm [99].
- A typical rock berm cross-section is in trapezoid shape with height from 0.6m to 1.5m, base length from 5m to 15m and side slope of either 3:1 or 4:1 [94].

Installation one – fully buried single cable crossing

Installation one comprises two fully buried single submarine cables at the same burial depths. At the crossing point, the upper cable is lifted up and laid on a pre-installed concrete mattress above the seafloor. Subsequently, a rock berm is post-installed over the whole crossing to provide an overall protection. Detailed installation parameters are summarized in Table 6.2 with a visual illustration in Figure 6.12.

Table 6.2: Parameter summary for installation one

Parameter	**Value**	**Unit**
Cable length (in model)	30	m
Cable burial depth (away from crossing)	0.5/ 1/ 2	m
Concrete mattress width	9	m
Concrete mattress depth	6	m
Concrete mattress thickness	150	mm
Rock berm base width	6.7	m
Rock berm base depth	12	m
Rock berm height	720	mm
Rock berm side slope	4:1	-

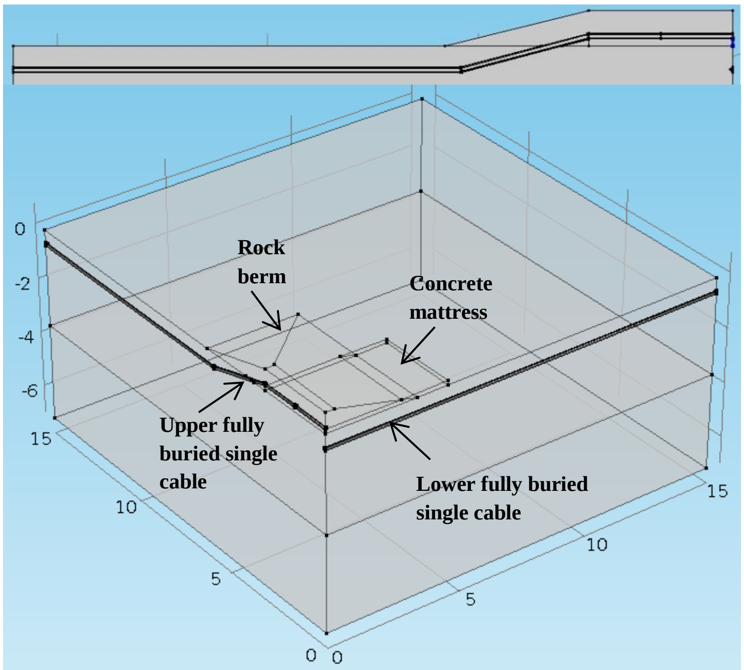

Figure 6.12: Illustration of installation one

Installation two – fully buried bundled bipole cable crossing

Installation two comprises two fully buried bipole cables at the same burial depth. At the crossing point, the upper circuit is lifted up and laid on a pre-installed concrete mattress above the seafloor. Similar to Installation One, a rock berm is post-installed over the whole crossing to provide an overall protection. Detailed installation parameters are summarized in Table 6.3, with a visual illustration in Figure 6.13.

Table 6.3: Parameter summary for installation two

Parameter	**Value**	**Unit**
Cable length (in model)	30	m
Cable burial depth (away from crossing)	0.5/ 1/ 2	m
Concrete mattress width	20	m
Concrete mattress depth	6	m
Concrete mattress thickness	150	mm
Rock berm base width	15	m
Rock berm base depth	15	m
Rock berm height	1400	mm
Rock berm side slope	4:1	-

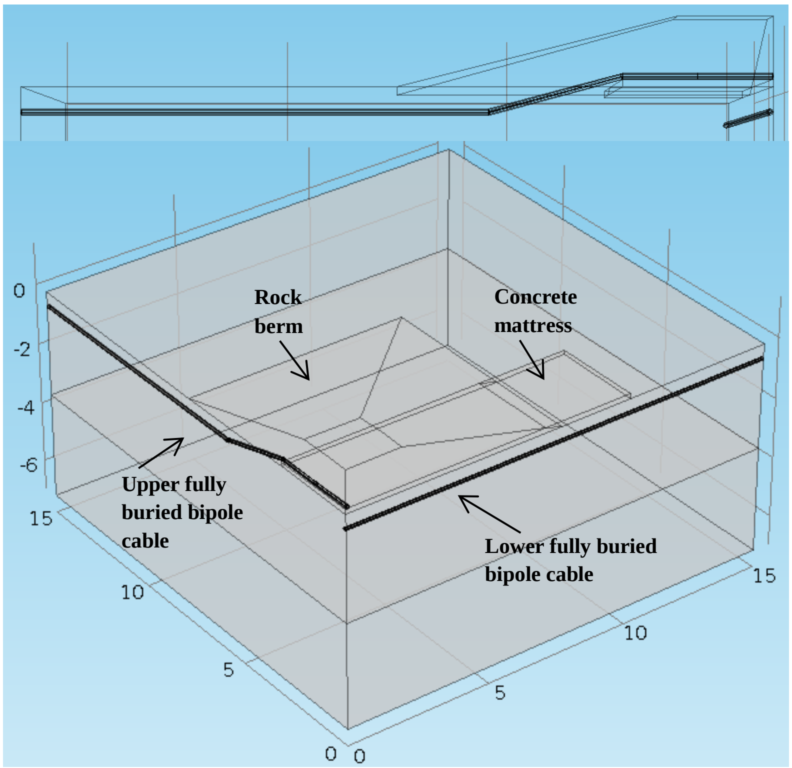

Figure 6.13: Illustration of installation two

Installation three – partially buried single cable crossing

Installation three consists of one fully buried single submarine cable and one unburied single cable laid on seabed. At the crossing point, the unburied cable is slightly lifted up and laid on a pre-installed concrete mattress above the seafloor. Overall, a rock berm is post-installed over the whole crossing to provide a final protection. Detailed installation parameters are summarized in Table 6.4, with a visual illustration in Figure 6.14.

Table 6.4: Parameter summary for installation three

Parameter	Value	Unit
Cable length (in model)	30	m
Cable burial depth (away from crossing)	0.5/ 1/ 2	m
Concrete mattress width	9	m
Concrete mattress depth	6	m
Concrete mattress thickness	150	mm
Rock berm base width	5.5	m
Rock berm base depth	30	m
Rock berm height	600	mm
Rock berm side slope	4:1	-

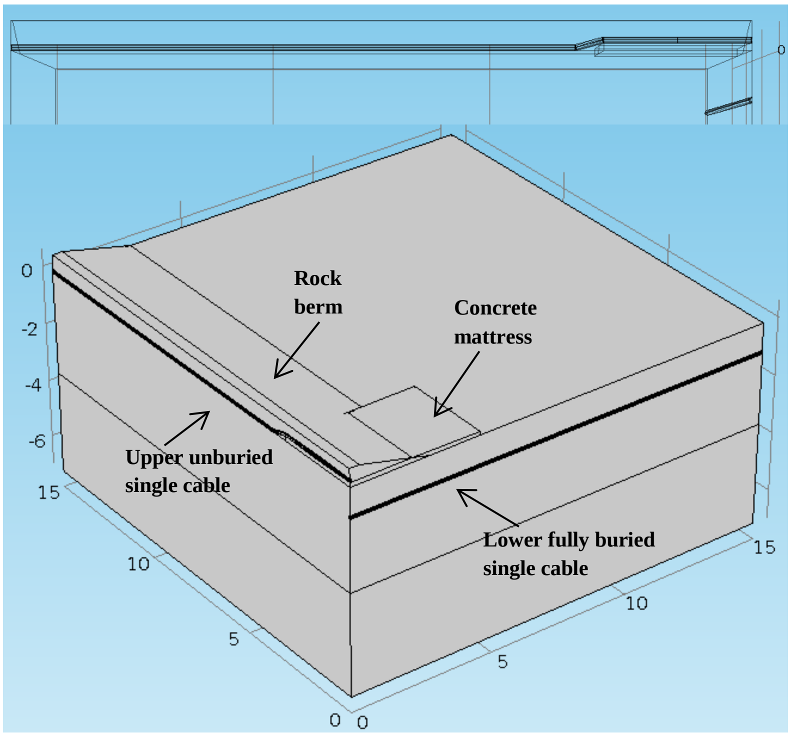

Figure 6.14: Illustration of installation three

Installation four – unburied single cable crossing

Installation four consists of two unburied single submarine cables. At the crossing point, a layer of concrete mattress is placed between two cables as the vertical separator. Subsequently, a rock berm is post-installed over the whole crossing to provide an overall protection. Detailed installation parameters are summarized in Table 6.5, with a visual illustration in Figure 6.15.

Table 6.5: Parameter summary for installation four

Parameter	Value	Unit
Cable length (in model)	30	m
Cable burial depth (away from crossing)	-	m
Concrete mattress width	4	m
Concrete mattress depth	5	m
Concrete mattress thickness	450	mm
Cable rock berm base width	5.5	m
Cable rock berm base depth	30	m
Cable rock berm height	600	mm
Cable rock berm side slope	4:1	-
Crossing rock berm base width	12	m
Crossing rock berm base depth	12	m
Crossing rock berm height	1500	mm
Crossing rock berm side slope	4:1	-

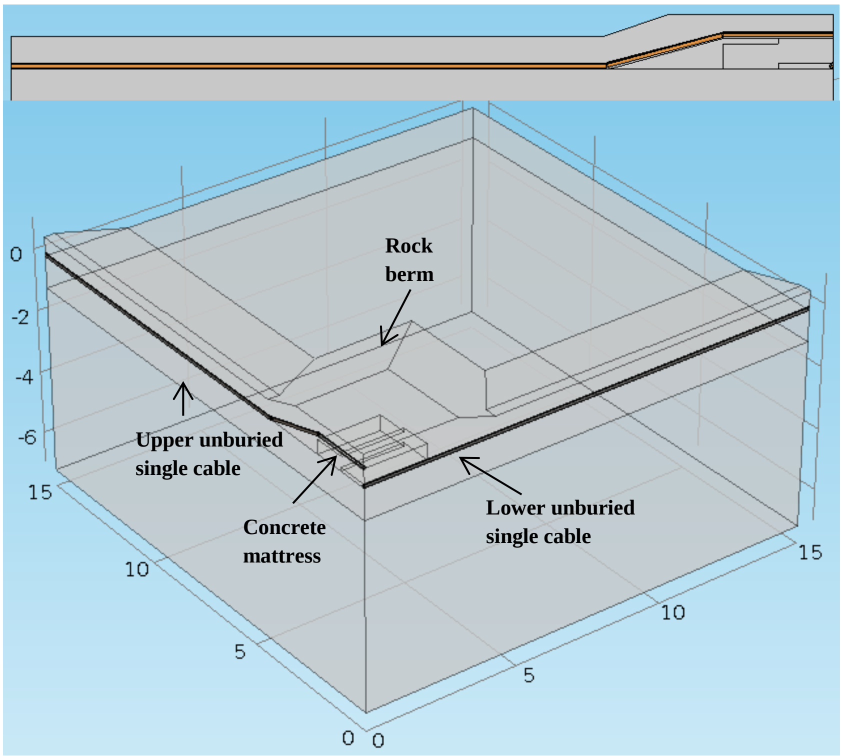

Figure 6.15: Illustration of installation four

6.2.2 Submarine HVDC cable analytical rating calculation

In order to identify the rating limiting factor, relevant theoretical rating calculations for an isolated circuit are summarized in Table 6.6, based on the circuit parameters in Table 3.2 (D_i = 101mm, γ = 0.03mm.kV^{-1}) and the installation environment in Table 3.3. Based on the worst case in Table 3.8, the rock berm has a loose packing configuration (i.e. thermal resistivity of 0.19 K.m.W^{-1} with convection and of 1.01K.m.W^{-1} without convection).

Table 6.6: Analytical rating calculation for isolated cable

Burial depth		**0m**	**0.5m**	**1m**	**2m**
Thermal-limited rating (IEC calculation)					
θ_∞ = 4^{0}C	isolated	3033*	2656	2541	2442
	bundled	-	2374	2217	2089
θ_∞ = 10^{0}C	isolated	2830*	2477	2370	2277
	bundled	-	2214	2067	1948
Electrical stress-limited rating (Developed calculation & FEA)					
θ_∞ = 4^{0}C	isolated	1945*	1944	1936	1928
	bundled	-	1881*	1867*	1848*
θ_∞ = 10^{0}C	isolated	1925*	1922	1914	1907
	bundled	-	1857*	1846*	1830*
Mechanical pressure-limited rating (Developed calculation) **					
θ_∞ = 4^{0}C	isolated	-	3080	2929	2799
	bundled	-	-	-	-
θ_∞ = 10^{0}C	isolated	-	2793	2656	2538
	bundled	-	-	-	-

* Due to the inapplicability of IEC60287 (i.e. cable laid on ground is not included) and the developed electrical stress-limited rating (i.e. bundled configuration is not included), values are calculated through FEA modeling.

** For the mechanical pressure-limited rating calculation (high temperature plane strain analysis), 36 MN.m^{-2} sheath yield strength, 45% Kraft paper porosity, and 20 ℃ cavity-free temperature are chosen as a moderate case.

From Table 6.6, it can be seen that $I_{stress} < I_{thermal} < I_{pressure}$ for all the environmental installations under test. In addition, both the thermal-limited rating and the mechanical pressure-limited rating are sensitive to cable burial depth (8% to 13% rating variation between 0.5m and 2m burial depths), while the electrical stress-limited rating varies less than 2%.

As the mechanical pressure-limited rating is the highest among the three rating methods under the calculation, only the thermal-limited rating and the electrical stress-limited rating are compared in the following tests.

6.2.3 FEA modelling/ test of submarine HVDC cable crossing

In this sub section, details of the FEA tests are presented with discussions. To compare, the analytical rating values (thermal-limited or electrical stress-limited) in Table 6.6 are applied to the four suggested crossing installations and the overall thermal-electric profile is monitored through FEA modelling. Four tests are designed and outlined in Table 6.7.

Table 6.7: Summary of the rating combination

	Test one	Test two	Test three	Test four
Upper circuit	$I_{thermal}$	I_{stress}	I_{stress}	$I_{thermal}$
Upper circuit	$I_{thermal}$	I_{stress}	$I_{thermal}$	$I_{thermal}$
Rock berm thermal resistivity ($K.m.W^{-1}$)	0.19	0.19	0.19	0.19/ 1.01

1) **Test one – thermal-limited rating for both circuits**

In test one, the thermal-limited rating is applied to both upper and lower circuits and rock berm free thermal convection is included. Detailed test results are summarized in Table 6.8.

Table 6.8: Maximum temperatures at the crossing point under test one

		Installation One			**Installation Two**			**Installation Three**			**Installation Four**
Lower circuit burial depth		0.5m	1m	2m	0.5m	1m	2m	0.5m	1m	2m	unburied
Ambient temperature		Maximum temperature at crossing point (^{0}C) (upper and lower cable end temperatures 15m away are 49^{0}C ± 0.5^{o}C)									
4^{0}C	U	38.5	35.0	32.2	41.7	35.8	31.2	50.2	49.9	49.6	49.7
	L	53.1	51.3	50.6	61.4	56.7	54.2	52.8	51.1	50.2	63.2
10^{0}C	U	40.1	37.2	34.7	42.9	37.8	33.9	50.2	49.9	49.7	49.8
	L	52.6	51.1	50.5	59.7	55.7	53.5	52.4	50.9	50.2	61.3

From Table 6.8, it can be found that with normal thermal-limited ratings, all the upper circuits can still operate safely and no rating reduction is required. For installations one and two, the upper cable/ circuit temperature at the crossing point is less than 42°C, because this cable section is lifted up and thus benefits a better upwards heat dissipation (i.e. closer to the top isothermal ground boundary). For installations three and four, it seems that the thermal interference from the lower cable/circuit is effectively minimized.

However, all the lower cables/ circuits exceed their upper limit of 50°C at the crossing point (up to 13°C temperature increase), which requires a necessary rating reduction in practical operations. Moreover, it verifies that increasing the vertical spacing does help to mitigate the thermal interference (exclude installation four), but the normal 30cm to 45cm suggestion is overoptimistic in our tests. For instance, at least 200cm vertical separation is required for the installation three

In Figure 6.16 below, sample longitudinal temperature distributions for all four installations are plotted, which refer to a 0.5m lower cable burial depth (installation one, two, three) and 4℃ ambient temperature.

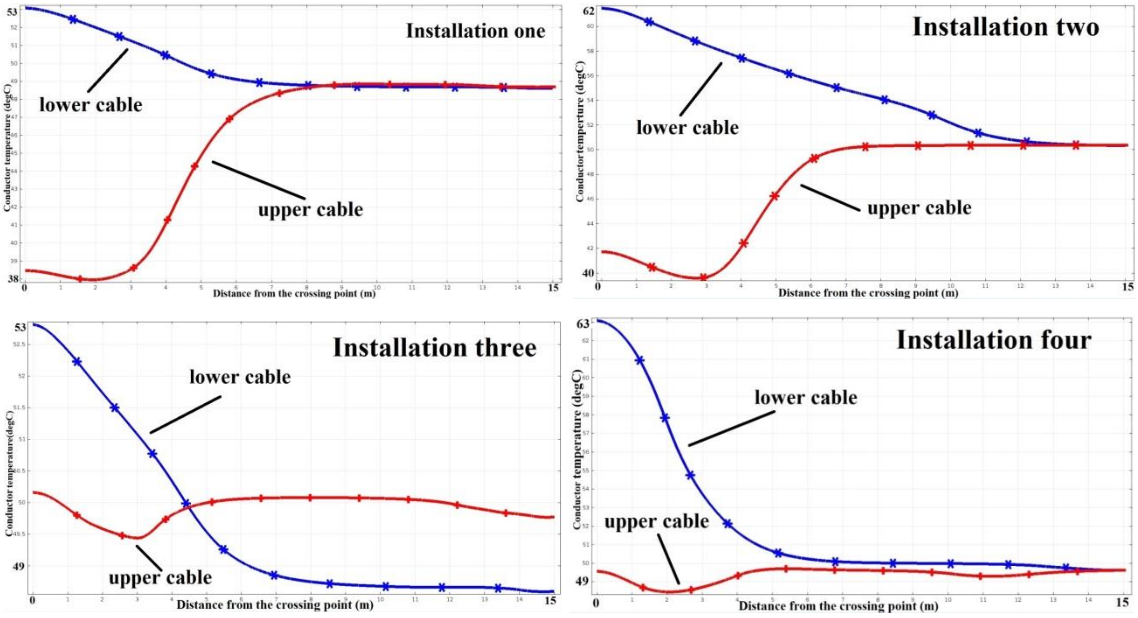

Figure 6.16: Sample longitudinal temperature distribution

In Figure 6.16, the lower cable has an increased maximum temperature at the crossing point due to the thermal interference, which gradually drops towards its cable end 15m away. For the upper cable, the crossing point temperature can be either similar to (installation three and four) or much lower than (installations one and two) its cable end. This is because the surrounding thermal environment at the crossing point is locally changed due to the crossing installation, while the rating remains to be calculated at cable ends.

2) Test two – electrical stress-limited rating for both circuits

In test two, the stress-limited rating is applied to both upper and lower circuits. Detailed test results are summarized in Table 6.9.

Table 6.9: Maximum temperatures at the crossing point under test two

		Installation One	**Installation Two**	**Installation Three**	**Installation Four**
Lower circuit burial depth		0.5m 1m 2m	0.5m 1m 2m	0.5m 1m 2m	unburied
Ambient temperature		Maximum temperature at crossing point (^{0}C)			
4^{0}C	U	21.6 21.3 21.2	26.8 26.0 25.1	21.2 21.1 20.9	20.9
	L	28.5 29.8 31.7	37.9 39.8 42.2	28.2 29.5 31.3	25.4
10^{0}C	U	27.4 27.2 26.8	32.7 32.0 31.2	27.2 27.1 27.0	26.9
	L	34.1 35.6 37.1	43.7 45.7 48.3	33.9 35.3 36.7	31.4

Note that the maximum dielectric stress increase at the crossing point compared with the cable ends (i.e. 30kV.mm^{-1} ±0.05kV.mm^{-1}) is less than 0.5kV.mm^{-1}.

According to Table 6.9, it is found that with stress-limited ratings, all the upper and lower cables/ circuits can still safely operate without exceeding any thermal or electrical limit. Therefore, there is no need to apply any rating reduction. Compared to test one, a big overall temperature decrease is observed, due to an application of the much lower stress-limited ratings. Note that longitudinal temperature distribution plots show a similar trend to test one (refer to Appendix Two).

3) Test three – electrical stress-limited/ thermal-limited rating for upper/ lower circuit

In test three, the stress-limited rating is applied to the upper circuit and the thermal-limited rating is applied to the lower circuit. It simulates a more common case where the existing old lower cable/ circuit is thermal-limited and owned by a third party. Test results are summarized in Table 6.10.

Table 6.10: Maximum temperatures at the crossing point under test three

		Installation One	**Installation Two**	**Installation Three**	**Installation Four**
Lower circuit burial depth		0.5m 1m 2m	0.5m 1m 2m	0.5m 1m 2m	unburied
Ambient temperature		Maximum temperature at crossing point (^{0}C) (lower cable end temperature 15m away is 49^{0}C ±0.5^{o}C)			
4^{0}C	U	22.2 21.7 21.4	28.3 26.8 25.5	21.6 21.3 21.1	21.6
	L	52.4 50.8 50.1	60.0 55.8 53.6	52.0 50.4 49.7	62.3
10^{0}C	U	27.8 27.5 27.0	33.7 32.5 31.3	27.5 27.3 27.1	27.5
	L	52.2 50.7 50.2	58.7 55.2 53.3	51.8 50.4 49.8	60.6

Note that the maximum dielectric stress increase at the crossing point compared with the cable ends (i.e. 30kV.mm^{-1} ±0.05kV.mm^{-1}) is less than 0.5kV.mm^{-1}.

Comparing Table 6.10 to Table 6.8, it is interesting to find that, on one hand, the upper cable temperature significantly decreases (over 15 ℃) with an electrical stress-limited rating. On the other hand, there is only less than 1^{0}C difference of the lower cable maximum temperature even through the upper cable largely reduces its heat losses. Note that longitudinal temperature distribution plots show a similar trend to test one (refer to Appendix Two).

As the big decrease of upper cable heat dissipation (temperature drop over 15^{0}C) only reduces the lower cable maximum temperature by less than 2^{0}C, it is doubtful that what causes an lower cable temperature rise at the crossing point may not be the direct thermal interference from the upper cable, but also the concrete mattress and the bulk rock berm installed above, which block the heat dissipation upwards (demonstrated in Test four).

4) Test four – Thermal blocking effect test for concrete mattress and rock berm

In test four, a sensitivity analysis is designed to examine the thermal effect of the concrete mattress and rock berm on the lower cable temperature rise. To isolate this thermal effect, installation one and two are chosen but without installing the upper cable/ circuit. The lower circuit carries a thermal-limited rating and has a reference temperature of 49°C $\pm 1^{o}$C at its cable end.

Rock berm thermal resistivity is either 0.19 K.m.W^{-1} or 1.01 K.m.W^{-1}, which represents the case with or without thermal convection. Note that a 400mm concrete mattress is normally not necessary for the installation one, thus it is examined here for a research purpose only. The ambient temperature is 4°C based on the worst case scenario (refer to test one/ two). Results are presented in percentage as the crossing point temperature rise above cable end, and are shown in Table 6.11.

Table 6.11: Thermal blocking effect test for concrete mattress and rock berm

temperature rise above cable end		**Installation condition**				
Installation one	Installation two	Lower cable Burial depth	150mm mattress	400mm mattress	0.19K.m.W^{-1} Rock berm	1.01K.m.W^{-1} Rock berm
6.5%	14.6%	0.5m	x		x	
11.5%	33%		x			x
11.5%	22%			x	x	
15%	33.8%			x		x
3%	7.2%	1m	x		x	
5.8%	17.5%		x			x
5.8%	10.5%			x	x	
7.7%	17.8%			x		x
1.4%	3.1%	2m	x		x	
2.5%	8.3%		x			x
2.5%	4.8%			x	x	
3%	8.5%			x		x

According to Table 6.11, it is verified that the installation of concrete mattress and rock berm does contribute to the increased lower cable/ circuit temperature at the crossing point. For bundled bipole cables, the temperature rise can be up to 33% of the temperature at cable end. However, this effect can be minimized by deeply burying the cable. A possible explanation is that most heat of a deeply buried cable is dissipated sideways rather than upwards, thus adding more layers on top will not heavily affect the overall heat dissipation.

By comparing the thermal blocking effect of concrete mattress and that of rock berm, concrete mattress is more preferred for practical crossing design and installations. This is because the work presented here has highlighted the importance of free convection within rock berms as a heat transfer mechanism. Depending on the local seabed conditions, it is possible that the pore spaces in the rock berm could become blocked with fine material. If this occurs, the cable may suddenly experience a more onerous thermal environment (e.g. higher temperature rise caused by nonconvective rock berm than thickened concrete mattress under installation two). This uncertainty will largely complicate the submarine crossing design and operation.

6.3 Summary

This chapter demonstrates the application of FEA numerical modelling method for HV cable crossing rating evaluations, which allows more detailed environmental parameters to be considered. The applicability of the developed modelling method is demonstrated through a comparison to the traditional analytical IEC60287 calculation, for HVAC land cable crossings. Subsequently, the modelling method is applied to submarine HVDC crossings, where the IEC method becomes inapplicable.

6.3.1 HVAC land cable crossing

For HVAC land cable crossings, the ground surface condition and backfill thermal property are found to be the two most important factors which affect the applicability of IEC60287-3-3. Especially when partial drying-out of the backfill is expected, the actual crossing rating can be 10% - 15% less than the IEC calculation results.

Technically speaking, if special backfill, which is not prone to moisture migration, can be installed around deeply buried cables, then drying-out of the backfill is negligible and the IEC60287-3-3 can be safely applied for rating calculations, provided that account is made of the 5% overrating from the assumption of an isothermal ground surface. In addition, when installing cable crossings on land, keeping the crossing at right angle is not necessarily thermally critical, provided sufficient vertical separation is available.

6.3.2 HVDC submarine cable crossing

For HVDC submarine cable crossings, the FEA modelling is the only available method at present to evaluate the rating performance, with its applicability demonstrated in this work. Within the crossing, the upper cable can normally operate under its stand-alone rating, while a de-rating of the lower cable might be required depending on its original rating limiting factor (thermal or electrical).

For the upper cable under a crossing installation, no de-rating is suggested regardless of its stand-alone rating limiting factor. This is because at the crossing point, the upper cable is normally lifted up (closer to the ground or rock berm surface) and thus benefits from a better cooling effect upwards. In addition, the beneath concrete mattress acts as a thermal barrier which mitigates the thermal interference from the lower cable.

For the lower cable which is originally electrical stress-limited, there is no need to de-rate under a crossing installation. This is because the stress-limited rating is generally much lower than the thermal rating, thus the maximum temperature can still be within the thermal limit at the crossing point. However, if the lower cable is originally thermal-limited, it is more likely to exceed its thermal limit due to both the mutual heating and the thermal blocking effect. Therefore, either de-rating the lower circuit or redesigning the physical installation (e.g. arc-shape concrete protective cover) is suggested. One exception would be that the lower cable is deeply buried (at least 2m), but it is very rare in submarine power cable transmission systems.

To clarify, the modelling results and conclusions are applicable for cable crossings under other water environments such as brackish and fresh water. In [163], there is less than 1% difference in thermal conductivity between fresh water (0.611 $W.m^{-1}.K^{-1}$) and brine (0.607 $W.m^{-1}.K^{-1}$). Moreover, people may question the modelling applicability by considering the seafloor scour and sand wave which may alter the thermal environment of the crossing. However, practical experience suggests that all these issues should be largely examined and avoided within the preliminary route and bathymetrical survey before conducting the crossing structure design. Therefore, it is reasonable to expect a stable thermal environment after the crossing is installed. As all the four crossing installations modelled in this work are similar to practical applications [94] [96], the results and conclusions should be widely valid.

Chapter 7

Conclusions

This thesis has documented a series of new current rating methodologies which are applicable to modern high voltage dc cable circuits under various installation conditions. Although the existing IEC thermal-limited rating method works well for most HVAC cables, it is limited to dc cables up to 5kV [31] and becomes inadequate for higher voltages as it fails to include all the limiting factors. This thesis has developed new rating methods for modern HVDC cables, which consider both the electrical and the mechanical constraints. In addition, a finite element analysis modelling technique has been developed originally for HV cable crossing ratings where the applicability of the IEC method is largely limited. All methods have been demonstrated through application to a nominal mass impregnated paper insulated HVDC cable. This chapter points out the research contributions, summarises the key research results, and discusses the future research area for HVDC cable applications.

7.1 Research contribution

The research conducted in this thesis forms a significant contribution to the literature in the field of HVDC cable rating calculations. Throughout the thesis, the mechanism of the inverted dielectric electric field distribution under high dc operating voltages has been fully reviewed, with several simplified numerical methods being developed to calculate this field. By comparing the developed methods to the existing analytical approximation, overall recommendations on the dielectric field calculation is summarised with enhanced accuracy and applicability. More importantly, through demonstrating an electrical constraint on the cable rating calculation (due to a thermal-electric interaction), a novel electrical stress-limited rating method has been developed, which allows a cable rating under this constraint to be calculated either analytically or numerically. Specifically, the analytical format of the stress-limited rating method has been benchmarked by numerical FEA modelling, which is of great value when applied to industrial R&D projects.

A further key contribution to the state of the art has been made by the original development of the mechanical pressure-limited rating method for HVDC cables, which may be used to ensure that there is no dielectric cavity creation during loading cycles. Throughout the development, both microscopic and macroscopic cavity creation mechanisms are comprehensively compared in terms of practical observations, fundamental assumptions, physical understandings, and existing calculations. Subsequently, a joint effect on cable rating calculation by combining these two mechanisms has been proposed for the first time. Following a successful derivation of the cable inner pressure calculation under coupled physics, the novel mechanical pressure-limited rating method has been developed, which allows a cable rating under the mechanical constraint to be calculated. In addition, simplifications have been performed to speed up the calculation process, which is of great value and accepted for practical users.

The third key contribution to the technical state of the art has been made by the development of FEA numerical modelling method to evaluate HV cable crossing ratings, which removes some idealistic assumptions from the traditional IEC method (e.g. isothermal ground surface, homogeneous backfill property) and identifies key environmental factors affecting the rating calculation. In detail, standard modelling techniques for HV cable crossings are developed, covering geometry building, material specification, heat source, boundary setting, meshing strategy, and solving mechanisms. Subsequently, standardised post-processing is suggested to calculate the cable crossing rating through interpolation. More specifically, the complex protection installation for submarine cable crossings has been analysed and modelled for the first time, with preliminary instruction being suggested on crossing design and operation. In general, the developed modelling method delivers a more optimal solution by removing the conservatism of the existing IEC method and successfully fills the gap where the traditional calculation does not apply.

Taken together, these three key contributions offer a significant step forward in the state of the art for HVDC cable circuit rating calculations, by making it possible to calculate ratings following both intrinsic (electrical, mechanical constraints) and extrinsic (environmental thermal constraint) limitations.

7.2 Research result

Through applying the developed electrical stress-limited rating method, it has been found that, under steady state, overly increasing the dc cable operating voltage may result in a reduction in cable transmission capacity. This is because the cable rating can gradually move from a thermal-limited domain to an electrical stress-limited under an increasing operating voltage. Once the rating becomes electrical stress-limited, it rapidly decreases with the increasing voltage. Besides the operating voltage, the cable installation environment is found to be another factor which can change the cable from thermal-limited to electrical stress-limited, such as shallow buried cables. For the transient evaluation, polarity reversals are proved to be a key issue causing a sudden dielectric breakdown, due to an additive superposition of the preload dielectric electric field before reversal and the immediate geometric electric field after reversal. Therefore, the HVDC cable is proved generally electrical stress-limited during the polarity reversal and reducing the preload current is able to lower the maximum transient stress. However, if a better understanding of the charge transport behaviour can be gained, it may be possible to permit higher levels of transient behaviour for short periods without sacrificing the preloading current.

Based on the developed mechanical pressure-limited rating method, it has been found that the microscopic and macroscopic cavity creation mechanisms are interlinked and perform a joint constraint on rating calculation, which specifies the upper and lower boundaries of the mechanical pressure-limited rating to prevent an excessive dielectric cavity creation. It has been demonstrated through the developed mechanical pressure-limited rating that releasing the constraint from one mechanism will enhance any constraint due to the other one. Specifically speaking, reducing the dielectric cavity-free temperature (e.g. modern impregnation process, use of pressure tapes) can largely reduce the reoccurrence of the pre-existing dielectric cavity during the cable cooling. However, at the same time, the cable suffers from a higher possibility to develop a sheath plastic deformation (Tresca’s yielding) during the loading up. Practically speaking, it is suggested to shallow bury the cable and select material designs with high sheath yield strength and low-porosity insulating paper, in order to mitigate the mechanical constraint.

By applying the developed FEA numerical modelling method, the applicability of IEC thermal-limited rating calculation for cable crossings on land is found largely dependent on the verification of an isothermal ground surface condition and a homogeneous backfill thermal property. Therefore, the IEC rating method is suggested to be applied to deeply buried HVDC cable crossings where the backfill drying-out is not expected. However, for submarine cable crossing applications, the developed numerical modelling method is the only applicable method at the moment, because the fundamental assumption (image theory) within the IEC method does not hold. Specifically speaking, the upper cable can still operate safely without any de-rating measure regardless of its stand-alone rating limiting factor, provided that no serious seafloor scour or sand wave is expected. However, for the lower cable which is thermal-limited before a crossing installation, current de-rating is generally required against an onerous thermal environment due to the mutual heating and thermal blocking effect.

Overall, for rating high voltage dc cable circuits, it is recommended to calculate the thermal-limited, electrical stress-limited and mechanical pressure-limited ratings simultaneously and always use the lowest one, where sufficient cable data is available.

7.3 Recommendations for further work

Despite the contribution made by this thesis, a number of areas have been identified which merit further work. In the field of electrical stress-limited ratings, a key issue that has been identified as worthy of further research is experimental exploration of the behaviour of the dielectric materials. Although both the temperature dependency coefficient and the field dependency coefficient of Mass impregnated paper insulation have been standardised, the same coefficients for polymeric insulations are hard to be quantified, where these two coefficients are reported varying with local temperature themselves and weakly being a function of each other. However, if this barrier can be overcome through experimental works, the electrical stress-limited rating method can be easily applied to extruded cables, which are an increasingly being used in hvdc submarine transmission links. Secondly, the accuracy of electrical stress-limited rating method can be improved if the microscopic space charge field can be formularized and integrated into the calculation. This is because the final inverted dielectric field distribution is actually the superposition of geometric Laplace field, macroscopic space charge field and microscopic space charge field, as shown in Figure 2.4 from Section 2.3.1. Therefore, experimental exploration of the microscopic space charge field becomes the primary step.

In terms of the mechanical pressure-limited rating, further research is recommended on enhancing its applicability by crosschecking the primary assumptions in Chapter 5. To achieve that, FEA numerical modelling can be a useful tool which is capable of dealing with coupled physics onto a microscopic level. However, difficulties may arise within the insulation modelling, as it is a mixture of solid Kraft paper and high-viscosity impregnant. Alternatively, experimental verification can be designed onto a macroscopic level by measuring the overall cable thermal expansion in mechanical domain. Secondly, novel lab experiments performing joint pressure and partial discharge monitoring are of great value to determine the cavity creation threshold during cable cooling. If this threshold pressure is identified, a complete range of mechanical pressure-limited rating is advised, which can largely minimize the dielectric cavity creation.

Finally for submarine hvdc cable crossing rating, it is recommended to expand work into designs of submarine crossing installation, as the crossing protection (rock berm) and separator (concrete mattress) can largely affect the overall thermal performance. Especially for the lower circuit of a crossing, a carefully designed installation is able to provide sufficient heat dissipation and thus reserves the transmission capacity without thermally de-rating the circuit. Although this further work is not totally academic oriented, it has much more practical significance by fulfilling industrial economic and commission concerns. More importantly, it has potential to become a successful model which delivers practical benefits from theoretical researches.

Appendices

Appendix One

Appendix One contains the derivation of the surface temperature distribution equation at arbitrary depth with consideration of present cables.

For cable cross sections, the radial heat transfer is given by (A1- 1) [164] in cylindrical coordinates:

$$\frac{1}{r}\frac{\partial}{\partial r}\left(\frac{r}{\rho_{bf}}\frac{\partial\theta}{\partial r}\right)+\frac{1}{r^2}\frac{\partial}{\partial\emptyset}\left(\frac{1}{\rho}\frac{\partial\theta}{\partial\emptyset}\right)+Q_h=c\frac{\partial\theta}{\partial t} \quad \text{(A1- 1)}$$

Where; Q_h is the heat generated per unit volume [W.m^{-3}], ρ_{bf} the backfill thermal resistivity [K.m.W^{-1}], θ the temperature [℃], c the constant, and t is the time [s].

Considering a single cable directly buried in uniform backfill. If the diameter of the cable is negligible compared to its burial depth, it will be reasonable to represent the cable as a filament heat source laid in an infinite medium. Under a steady-state condition, (A1- 1) is simplified to:

$$\frac{d\theta}{dr}+\frac{\rho_{bf}}{2\pi r}W_t=0 \quad \text{(A1- 2)}$$

Where; W_t is the heat losses inside the cable by integrating Q_h [W.m^{-1}]. So the temperature rise $\Delta\theta$ at any point M located at a distance d from the cable centre is given by integrating (A1- 2) from $r = \infty$ to $r = d$.

$$\Delta\theta=\int_{\infty}^{d}-\frac{\rho_{bf}}{2\pi r}W_t\,dr \quad \text{(A1- 3)}$$

By applying the Kennelly principle, which places an image cable with - W_t symmetrically with respect to the earth surface, thus

$$\Delta\theta=\Delta\theta'+\Delta\theta''=\int_{\infty}^{d}-\frac{\rho_{bf}}{2\pi r}W_t dr+\int_{\infty}^{d'}\frac{\rho_{bf}}{2\pi r}W_t dr \quad \text{(A1- 4)}$$

$$\Delta\theta=-\frac{\rho_{bf}}{2\pi}W_t\ln d+\frac{\rho_{bf}}{2\pi}W_t\ln d'=\frac{\rho_{bf}}{2\pi}W_t\ln\frac{d'}{d} \quad \text{(A1- 5)}$$

Where; d ´is the distance between point M and the image cable above the ground surface [m]. By applying the superposition principle, (A1- 6) results:

$$\theta=\theta_{amb}+\sum_{j=1}^{n}\frac{\rho_{bf}}{2\pi}W_{tj}\ln\frac{d_j'}{d_j} \quad \text{(A1- 6)}$$

Appendix Two

Appendix Two contains the testing figures for HVDC cable crossing rating modelling in Chapter 6.

Submarine HVDC cable crossing test two – electrical stress-limited rating for both circuits

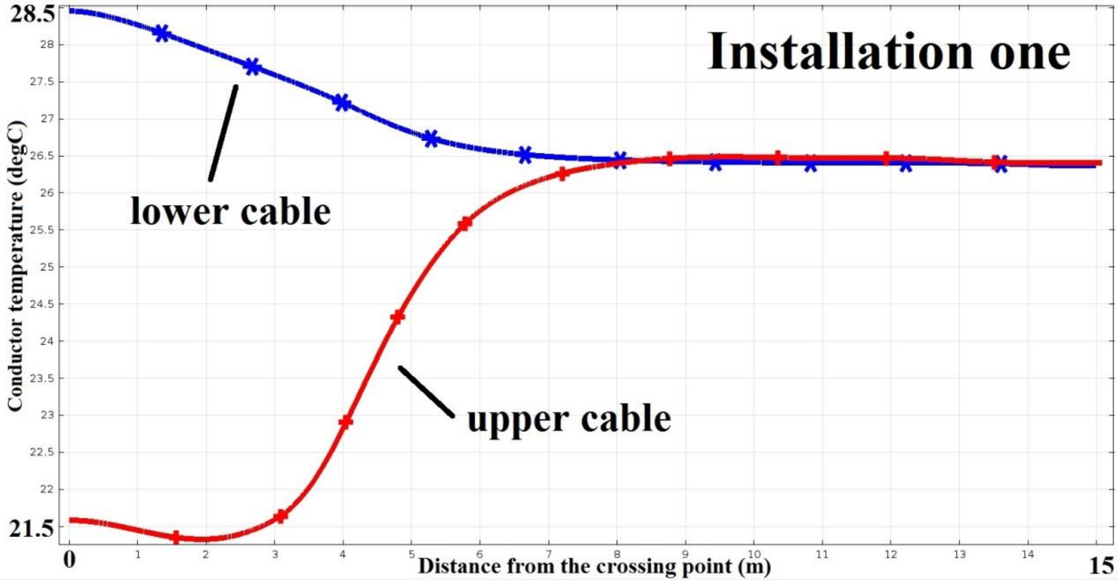

Figure A2.1 – Longitudinal temperature distribution for installation one under test two

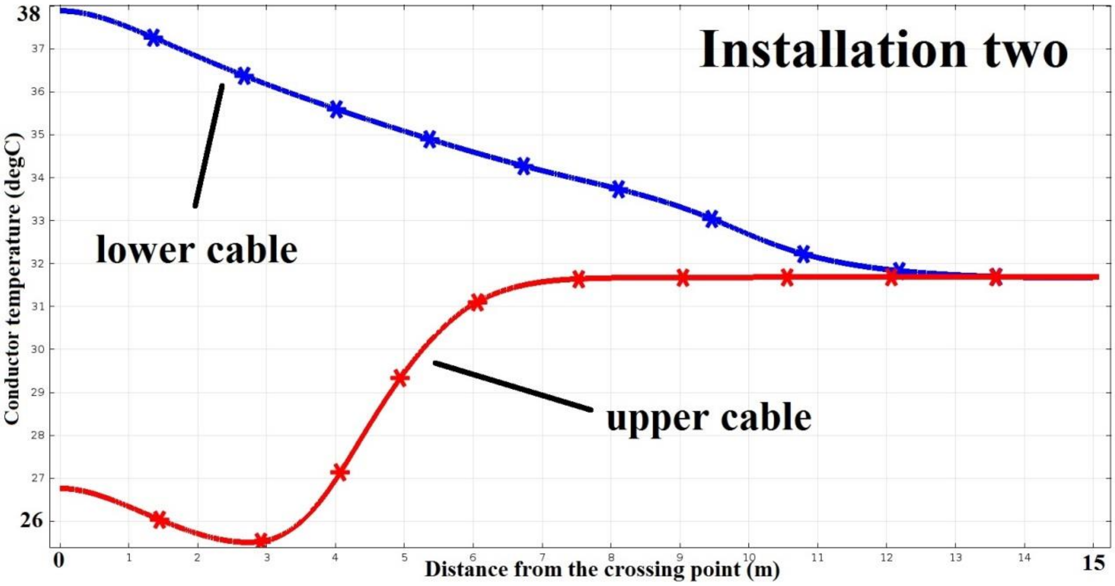

Figure A2.2 – Longitudinal temperature distribution for installation two under test two

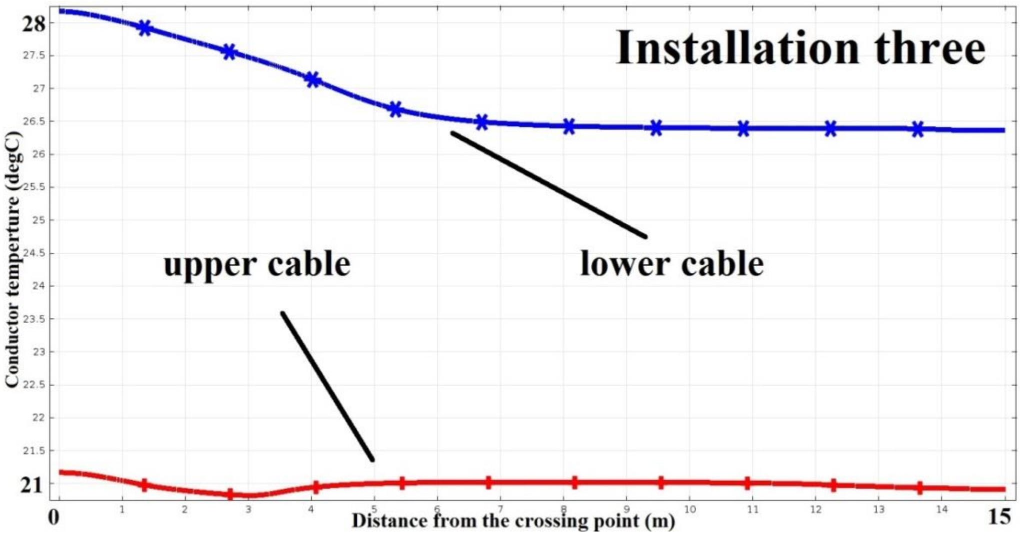

Figure A2.3 – Longitudinal temperature distribution for installation three under test two

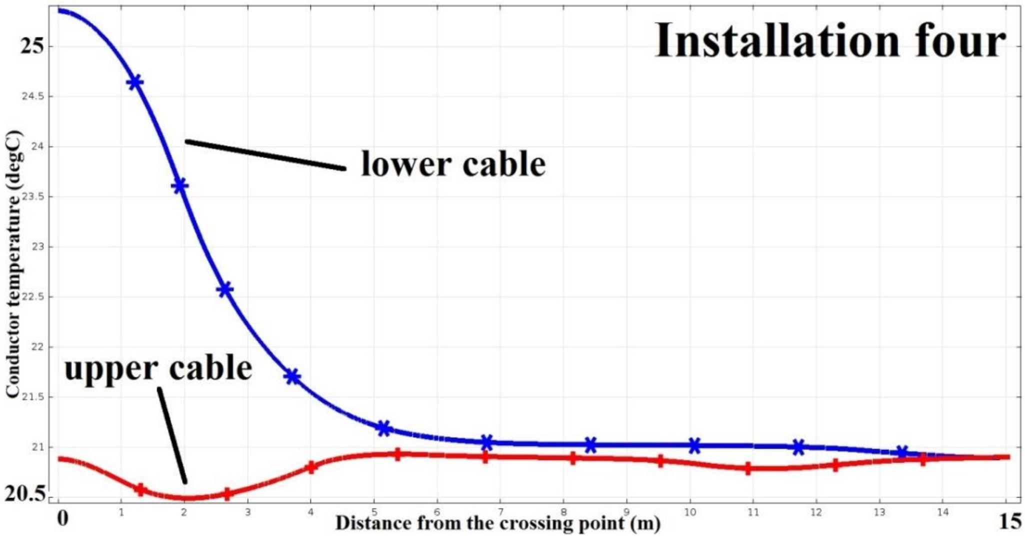

Figure A2.4 – Longitudinal temperature distribution for installation four under test two

Submarine HVDC cable crossing test three – electrical stress-limited/ thermal-limited rating for upper/ lower circuits

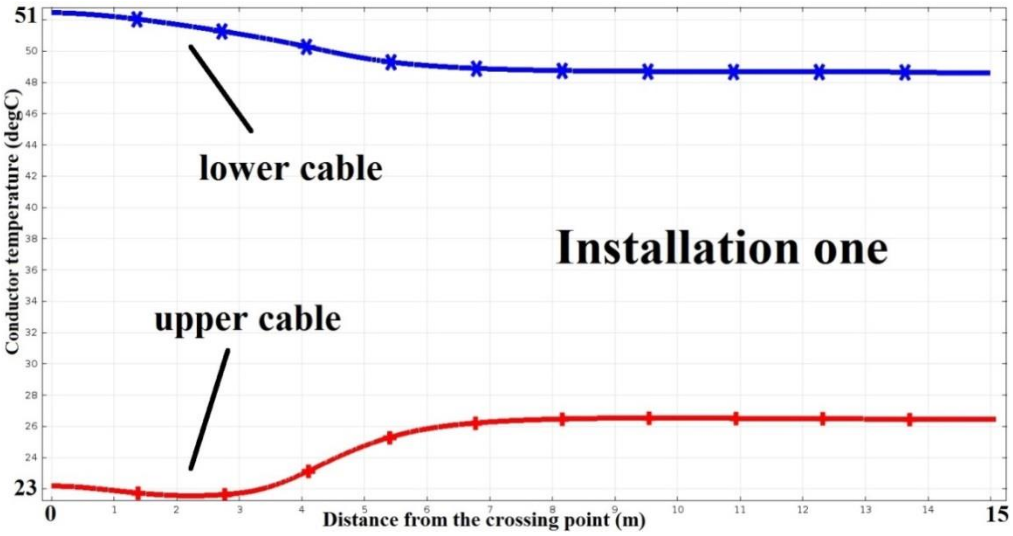

Figure A2.5 – Longitudinal temperature distribution for installation one under test three

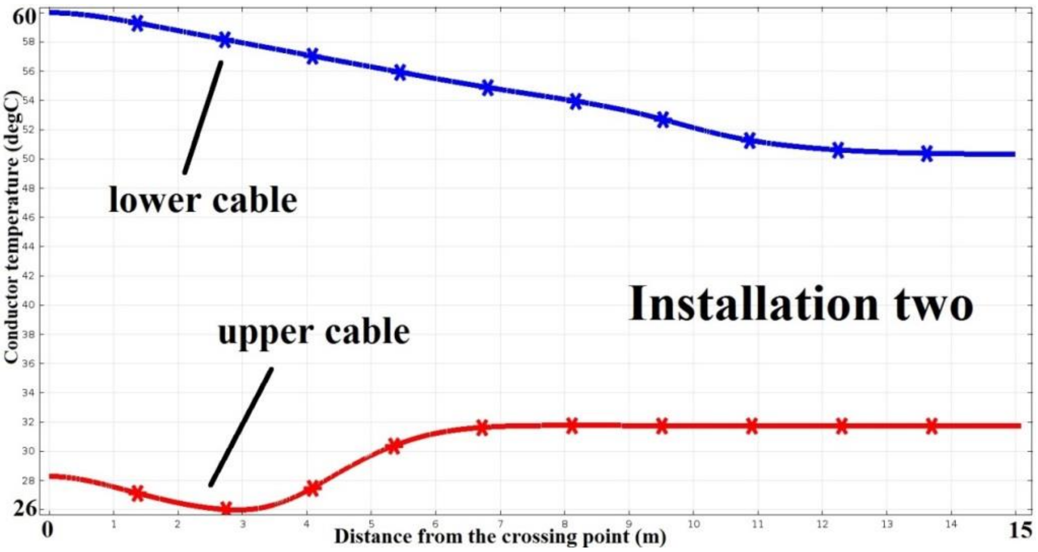

Figure A2.6 – Longitudinal temperature distribution for installation two under test three

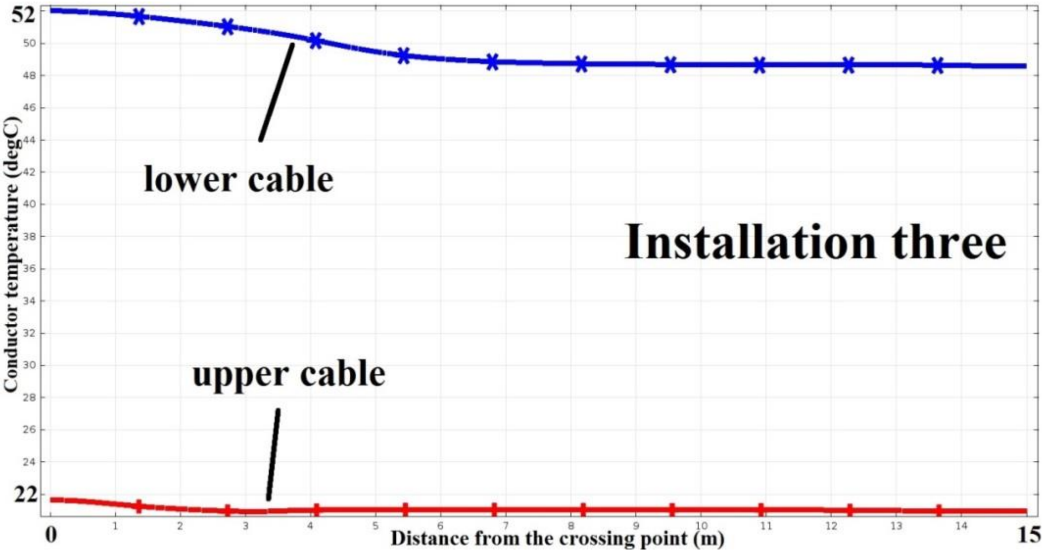

Figure A2.7 – Longitudinal temperature distribution for installation three under test three

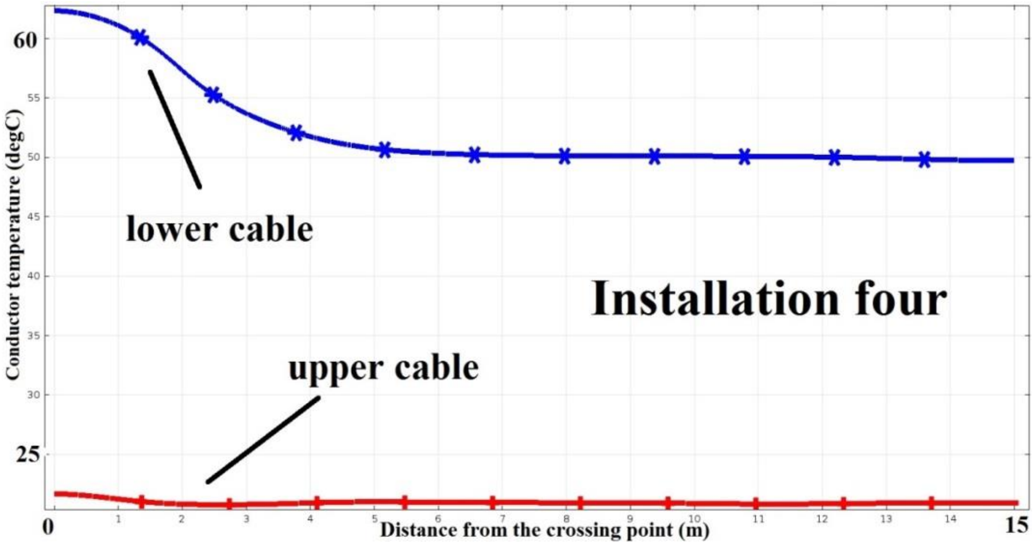

Figure A2.8 – Longitudinal temperature distribution for installation four under test three

Reference

[1] V. Smil, *Science, energy, ethics, and civilization,* Cambridge: Cambridge University Press, 2010.

[2] Department of Energy & Climate Change (DECC), "UK renewable energy roadmap: 2012 update," Dec 2012. [Online]. Available: https://www.gov.uk/government/publications/uk-renewable-energy-roadmap-update. [Accessed Dec 2013].

[3] International Energy Agency (IEA), "World Development Indicators: Energy production and use," Nov 2013. [Online]. Available: http://wdi.worldbank.org/table/3.6. [Accessed Nov 2013].

[4] Department of Energy & Climate Change (DECC), "The Energy Efficiency Strategy: The Energy Efficiency Opportunity in the UK," Nov 2012. [Online]. Available: https://www.gov.uk/government/uploads/system/uploads/attachment_data/file/65602/6927-energy-efficiency-strategy--the-energy-efficiency.pdf. [Accessed Oct 2013].

[5] International Energy Agency (IEA), "Key World Energy STATISTICS," 2006 - 2012. [Online]. Available: http://www.iea.org/statistics/. [Accessed Nov 2013].

[6] Department of Energy & Climate Change (DECC), "Statistics at DECC," Department of Energy & Climate Change, 2004. [Online]. Available: https://www.gov.uk/government/organisations/department-of-energy-climate-change/about/statistics. [Accessed Nov 2013].

[7] U.S. Energy Informaion Administration (EIA), "International Energy Statistics," 1980 - 2011. [Online]. Available: http://www.eia.gov/countries/country-data.cfm?fips=UK. [Accessed Nov 2013].

[8] Department of Energy & Climate Change (DECC), "Nuclear accounts for 19% of UK electricity generation in 2012," Nuclear Engineering International, Jul 2013. [Online]. Available: http://www.neimagazine.com/news/newsnuclear-accounts-for-19-of-uk-electricity-generation-in-2012. [Accessed Nov 2013].

[9] BBC News Business, "UK nuclear power plant gets go-ahead," British Broadcasting Corporation (BBC), Oct 2013. [Online]. Available: http://www.bbc.co.uk/news/business-24604218. [Accessed Dec 2013].

[10] M. Grimston, "The importance of politics to nuclear new build," The Royal Institute of International Affairs, London, 2005.

[11] Y. Du and E. Parsons, "Update on the cost of unclear power," Center for Energy and Environment Policy Research (CEEPR), Cambridge (US), 2009.

[12] BBC Weather Center, "Wind Power," British Broadcasting Corporation (BBC), July 2009. [Online]. Available: http://www.bbc.co.uk/climate/adaptation/wind_power.shtml. [Accessed Dec 2013].

[13] Department of Energy & Climate Change (DECC), “UK renewable energy roadmap: 2013 update,” Nov 2013. [Online]. Available: https://www.gov.uk/government/publications/uk-renewable-energy-roadmap-second-update. [Accessed Dec 2013].

[14] E. Ares, “The Renewables Obligation (RO),” Aug 2012. [Online]. Available: http://www.parliament.uk/briefing-papers/sn05870.pdf. [Accessed Dec 2013].

[15] D. P. Hauser, “System costs an the location of new generating plant in England and Wales,” *Transactions of the Institute of British Geographers,* no. 54, pp. 101-121, 1971.

[16] British Electricity Authority and Area Electricity Boards, “Electricity Act 1947,” 1947. [Online]. Available: http://www.legislation.gov.uk/ukpga/Geo6/10-11/54/contents. [Accessed Dec 2013].

[17] Cigré WG B1, “Statistics of ac underground cable in power networks,” *Electra,* vol. 235, pp. 43-55, 2007.

[18] ABB AB, “Xiangjiaba - Shanghai ±800 kV UHVDC transmission project: world's largest transmission link with breakthrough technology,” 2010. [Online]. Available: http://www05.abb.com/global/scot/scot221.nsf/veritydisplay/91607492c240069bc1257927004ff05c/$file/pow0056%20rev1%20lr.pdf. [Accessed Dec 2013].

[19] B. Badenhorst, C. v. d. Merwe and J. d. V. TAP, “China unveils 1000kV AC transmission grid,” *Energize,* pp. 41-42, 2009.

[20] National Grid, “Undergrouding high voltage electricity transmission lines: The technical issues,” Aug 2013. [Online]. Available: www2.nationalgrid.com/WorkArea/DownloadAsset.aspx?id=13797. [Accessed Jan 2014].

[21] C. Bradley, “HVDC projects within the UK,” Nov 2013. [Online]. Available: http://www.jicable-hvdc13.fr/documents/RoundTable/01_Caroline_Bradley_(UK).pdf. [Accessed Dec 2013].

[22] G. F. Moore, Electric Cables (HANDBOOK), Oxford: Wiley-Blackwell, 1997.

[23] D. Culley, “The future of HVDC in the UK,” in *The Fifth UHVnet Colloquium,* Leicester, 2012.

[24] H. Doyen, H. Ebeling, H. -J. Fiss and M. Labrenz, “Experiences with different cable designs and laying methods in conjunction with the power supply of the islands in the North- and Baltic-Sea,” in *Electricity Distribution, 1989. CIRED 1989. 10th International Conference on,* Brighton, 1989.

[25] T. Ingledow, R. M. Fairfield, E. L. Davey, K. S. Brazier and J. N. Gibson, “British Columbia–Vancouver Island 138-kV submarine power cable,” in *Proceedings of the IEE - Part A: Power Engineering,* 1957.

[26] A. Fujimori, T. Tanaka, H. Takashima, T. Imajo, R. Hata, T. Tanabe, S. Yoshida and T. Kakihana, “Development of 500kV DC PPLP-insulated oil-filled submarine cable,” *IEEE Transactions on Power Delivery,* vol. 11, no. 1, pp. 43-50, 1996.

[27] F. Goodrich and B. Andersen, “The 2000 MW hvdc link between England and France,” *Power Engineering Journal,* pp. 69-74.

[28] T. Worzyk, Submarine Power Cables: Design,Installation,Repair Environmental Aspects, Springer, 2009.

[29] European Wind Energy Association, “Pure Power - wind energy targets for 2020 and 2030,” European Wind Energy Association(EWEA), Brussels, 2011.

[30] P. Penserini and J. M. Prost, “Jicable HVDC'13: Round Table & Conclusion,” Nov 2013. [Online]. Available: http://www.jicable-hvdc13.fr/ClosingSession_en.php. [Accessed Dec 2013].

[31] *BS IEC 60287-1-1:2006:'Electric Cables - Calculation of the current rating',* Electrotechnical committee: British Standards Board,2006, 2006.

[32] Z. Y. Huang, J. A. Pilgrim, P. L. Lewin, S. G. Swingler and D. Payne, “Current rating methodology for mass impregnated HVDC cables,” in *Electrical Insulation Conference (EIC), 2013 IEEE,* Ottawa, 2013.

[33] *BS IEC 60287-3-3:2007:'Electric Cables - Calculation of the current rating',* Electrotechnical committee: British Standards Board,2007, 2007.

[34] F. J. Miranda and H. W. Holdup, “Development of 400kV cable in Great Britain,” *IEEE Transactions on Power Apparatus and Systems,* vol. 86, no. 5, pp. 604-611, 1967.

[35] A. N. Arman, F. J. Miranda and G. R. Bishop, “Progress in oil-filled cables and their accessories,” in *The Proceedings of the Institution of Electrical Engineers*, Surat, 1961.

[36] Y. Zhang, J. Lewiner, C. Alquie and N. Hampton, “Evidence of strong correlation between space-charge buildup and breakdown in cable insulation,” *Dielectrics and Electrical Insulation, IEEE Transactions on,* vol. 3, no. 6, pp. 778-783, dec 1996.

[37] T. Yamanaka, S. Maruyama and T. Tanaka, “The development of DC+/-500 kV XLPE cable in consideration of the space charge accumulation,” in *Properties and Applications of Dielectric Materials, 2003. Proceedings of the 7th International Conference on,* Nagoya, Japan, 2003.

[38] Y. Maekawa, K. Watanabe, S. Maruyama, Y. Murata and H. Hirota, “Research and development of DC+/-500kV extruded cables,” CIGRE Paper No. 21-203, Tokyo, Japan, 2002.

[39] T. Worzyk, “100 years of high voltage DC links,” Modern Power Systems, November 2007. [Online]. Available: http://www.modernpowersystems.com/story.asp?sectionCode=88&storyCode=2050430.

[40] P. Szabo, O. Hassager and E. Strobech, “Modeling of pressure effects in HVDC cables,” *IEEE Transactions on Dielectrics and Electrical Insulation,* vol. 6, no. 6, pp. 845-851, 1999.

[41] R. Liu, “Long-Distance DC electrical power transmission,” *IEEE Electrical Insulation Magazine,* vol. 29, no. 5, pp. 37-46, 2013.

[42] National Grid & Scottish Power Transmission, “Western Link Project,” Consense, 2012. [Online]. Available: http://www.westernhvdclink.co.uk/. [Accessed Dec 2013].

[43] T. Worzyk, M. Bergkvist, P. Nordberg and C. Tornkvist, “Breakdown voltage of polypropylene laminated paper (PPLP) in plain samples and a full scale cable,” in *Electrical Insulation and Dielectric Phenomena, 1997. IEEE 1997 Annual Report., Conference on,* Minneapolis, 1997.

[44] B. Sanden and E. Iidstad, “DC electrical and mechanical characterisation of polypropylene film,” in *IEEE International Conference on Conduction and Breakdown in Solid Dielectrics,* Vasteras, 1998.

[45] T. Nakagawa, “Measurement of space charge accumulation in PPLP,” in *Proceedings of 13th International Conference on Dielectric Liquids (ICDL '99),* Nara, 1999.

[46] Cigré Working Group 02-Study Committee 21, *Recommendations for tests of power transmission dc cables for a rated voltage up to 800kv,* Electra(189), 2000.

[47] Cigré Task Force B1.16, “Addendum to recommendations for tests of power transmission DC cables for a rated voltage up to 800kV,” *Electra,* vol. 218, pp. 39-45, February 2005.

[48] R. Hata, “Solid dc submarine cable insulated with polypropylene laminated paper (PPLP),” *SEI Technical Review,* pp. 3-9, 2006.

[49] B. M. Weedy, “A cable-system thermal analogue,” *Journal of the Institution of Electrical Engineers,* vol. 8, no. 94, pp. 468-469, 1962.

[50] B. M. Weedy, “Thermal transients in a high-voltage cable system with natural and artificial cooling,” *Proceedings of the IEE - Part A: Power Engineering,* vol. 109, no. 47, pp. 461-470, october 1962.

[51] B. M. Weedy and J. P. Perkins, “Steady-state thermal analysis of a 400 kV-cable through joint,” *Proceedings of the IEE,* vol. 114, no. 1, pp. 109-115, 1967.

[52] J. H. Neher, “A simplified mathematical procedure for determining the transient temperature rise of cable systems,” *Power Apparatus and Systems, Part III. Transactions of the American Institute of Electrical Engineers,* vol. 72, no. 2, pp. 712-718, jan. 1953.

[53] Cigré Working Group 08-Study Committee 21, *The steady state thermal behaviour of accessories of cooled cable system,* vol. 128, Electra, 1990, pp. 64-98.

[54] M. M. Abdel Aziz and H. Riege, “A new method for cable joints thermal analysis,” *IEEE Transactions on Power Apparatus and Systems,* Vols. PAS-99, pp. 2386-2392, 1980.

[55] Cigré Working Group 08-Study Committee 21, *The calculation of continuous ratings for force cooled cables,* vol. 66, Electra, 1979, pp. 59-84.

[56] Cigré Working Group 02-Study Committee 21, *Computer method for the calculation of the response of single-core cables to a step function thermal Transient,* vol. 87, Electra, 1983, pp. 41-64.

[57] R. Courant, “Variational methods for the solution of problems of equilibrium and vibration,” *Bulletin of American Mathematical Society,* vol. 49, pp. 1-43, 1943.

[58] J. Nahman and M. Tanaskovic, “Determination of the current carrying capacity of cables using the finite element method,” *Electric Power Systems Research,* vol. 61, no. 2, pp. 109-117, 2002.

[59] C. C. Hwang and Y. H. Jiang, “Extensions to the finite element method for thermal analysis of underground cable systems,” *Electric Power Systems Research,* vol. 64, no. 2, pp. 159-164, 2003.

[60] IEC Technical report TR-62095, *Electric Cables - Calculation for current ratings - finite element method,* 2003.

[61] Z. Y. Huang, J. A. Pilgrim, P. L. Lewin, F. Waite and D. Payne, “Calculating the thermal impact of cable crossings,” in *INSUCON 2013, International Electrical Insulation Conference*, Birmingham, 2013.

[62] M. Jeroense, Charges and Discharges in HVDC Cables: In Particular in Mass-impregnated HVDC Cables, Delft: Delft University Press, 1997, p. 222.

[63] C. Eoll, “Theory of stress distribution in insulation of high-voltage dc cables: part I,” *Electrical Insulation, IEEE Transactions on,* Vols. EI-10, no. 1, pp. 27-35, march 1975.

[64] D. Fabiani, G. Montanari, C. Laurent, G. Teyssedre, P. Morshuis, R. Bodega, L. Dissado, A. Campus and U. Nilsson, “Polymeric hvdc cable design and space charge accumulation. part 1: insulation/semicon interface,” *Electrical Insulation Magazine, IEEE,* vol. 23, no. 6, pp. 11-19, nov.-dec. 2007.

[65] D. Fabiani, G. Montanari, C. Laurent, G. Teyssedre, P. Morshuis, R. Bodega and L. Dissado, “HVDC cable design and space charge accumulation. part 3: effect of temperature gradient,” *Electrical Insulation Magazine, IEEE,* vol. 24, no. 2, pp. 5-14, march-april 2008.

[66] I. McAllister, G. Crichton and A. Pedersen, “Charge accumulation in dc cables: a macroscopic approach,” in *Electrical Insulation, 1994., Conference Record of the 1994 IEEE International Symposium on,* Pittsburgh, USA, 1994.

[67] G. Montanari and P. Morshuis, “Space charge phenomenology in polymeric insulating materials,” *Dielectrics and Electrical Insulation, IEEE Transactions on,* vol. 12, no. 4, pp. 754-767, aug. 2005.

[68] S. L. Roy, F. Boufayed, G. Teyssedre, C. Laurent, P. Segur, R. Bodega, P. Morshuis, G. Montanan and L. Dissado, “Computer simulation of space charge distribution in an XLPE-EPR sandwich,” in *Electrical Insulation and Dielectric Phenomena, 2005. CEIDP '05. 2005 Annual Report Conference on*, Nashville, 2005.

[69] K. W. Wagner, “Erklärung der dielektrischen Nachwirkungsvorgänge auf Grund Maxwellscher Vorstellungen,” *Archiv für Elektrotechnik,* vol. 2, no. 9, pp. 371-387, 1914.

[70] W. Stanley, Dielectric Breakdown of Solids, Oxford: Clarendon Press, 1953.

[71] J. J. O'Dwyer, “Theory of dielectric breakdown in solids,” *J. Electrochem. Soc.,* vol. 116, no. 2, pp. 239-242, 1969.

[72] F. Buller, “Calculation of electrical stresses in dc cable insulation,” *IEEE Transactions on Power Apparatus and Systems,* Vols. PAS-86, no. 10, pp. 1169-1178, 1967.

[73] M. Jeroense and F. Kreuger, “Electrical conduction in hvdc mass-impregnated paper cable,” *IEEE Transactions on Dielectrics and Electrical Insulation,* vol. 2, no. 5, pp. 718-723, October 1995.

[74] Gosse, B. and Gosse, J.P. and Sauviat, M., “Interactions between the solid and the ions of the liquid in impregnated paper,” *IEEE Transactions on Electrical Insulation,* Vols. EI-15, no. 2, pp. 104-111, 1980.

[75] C. C. Reddy and T. Ramu, “On the intrinsic thermal stability in hvdc cables,” *IEEE Transactions on Dielectrics and Electrical Insulation,* vol. 14, no. 6, pp. 1509-1515, December 2007.

[76] J.-M.Oudin and M.Fallou, “Etude et developpement des cables a courant continu,” *Rev.Gen.Elec.,* vol. 75, pp. 257-263, 1966.

[77] C. Eoll, “Theory of stress distribution in insulation of high-voltage dc cables: part II,” *Electrical Insulation, IEEE Transactions on,* Vols. EI-10, no. 2, pp. 49-54, June 1975.

[78] P. G. Priaroggia, P. Metra and G. Miramonti, “Research on the breakdown under type test of non-pressurized paper-insulated HVDC cables,” *European Transactions on Electrical Power,* vol. 3, no. 5, pp. 321-330, 1993.

[79] M. Jeroense and F. H. Kreuger, “Partial discharge measurement on a high voltage direct current mass impregnated paper cable,” in *IEEE International Symposium on Electrical Insulation,* Montreal, 1996.

[80] A. Eriksson, G. Henning, B. Ekenstierna, U. Axelsson and M. Akke, “Development work concerning testing procedures of mass-impregnated HVDC cables,” in *International Council Large Electric Systems (CIGRE),* Paris, 1994.

[81] J. N. Johnsen, “High voltage mass-impregnated power cable”. USA Patent 4 782 194A, 1 Nov 1988.

[82] S. Timoshenko and J. N. Goodier, Theory of Elasticity, New York: McGRAW-HILL, 1951.

[83] D. J. Swaffield, P. L. Lewin and S. J. Sutton, “Methods for rating directly buried high voltage cable circuits,” *IET Generation, Transmission and Distribution,* vol. 2, no. 3, pp. 393-401, 2008.

[84] L. A. Ramdas, “Some new instruments and experimental techniques developed in the agricultural metreology secction at poona,” *J.Sci.Ind.Res,* vol. 7, no. 1, pp. 16-29, 1948.

[85] D. J. Swaffield, P. L. Lewin and M. LeBlanc, “Investigation into the conservatism of high voltage cable rating methods: A comparison between IEC60287 and Finite Element Analysis,” in *Proceedings of the XIVth International Symposium on High Voltage*

Engineering, Beijing, 2005.

[86] *BS IEC 60287-3-1 (1995),BS 7769-3.1 (1997):'Electric Cables - Calculation of the current rating',* Electrotechnical committee: British Standards Board, 1997.

[87] J. Pilgrim, D. Swaffield, P. Lewin, S. Swingler, F. Waite and D. Payne, “Impact of moisture migration on the current rating of high operating temperature power cables,” in *8th International Conference on Insulated Power Cables*, Versailles, 2011.

[88] G. J. Anders, Rating of Electric Power Cables: Ampacity Computations for Transmission, Distribution, and Industrial Applications, McGraw-Hill Inc.,US, 1997.

[89] G. J. Anders, Rating of Electric Power Cables in Unfavorable Thermal Environment, IEEE PRESS, 2005.

[90] M. Sharples, “Offshore electrical cable burial for wind farms: State of the art, standards and guidance & acceptable burial depths, separation distances and sand wave effect,” The Bureau of Ocean Energy Management, Regulation and Enforcement , USA, 2011.

[91] WodV/RH, “Cable installation study for DOWEC,” Van Oord ACZ, Netherlands, 2001.

[92] Mole, P., Featherstone, J. and Winter, S., “Cable protection: Solution through new installation and burial approaches,” in *SubOptic'97,* San Francisco, 1997.

[93] P. Allen, “Selecting appropriate cable burial depths - A methodology,” in *IBC Conference on Submarine Communication*, Cannes, 1998.

[94] A. Pattison and M. Legerton, “Dogger Bank Creyke Beck environmental statement - chapter 5 project description,” Forwind, Reading, UK, 2013.

[95] J. Beale, “Transmission cable protection and stabilisation for the wave and tidal energy industries,” in *Ninth European Wave and Tidal Energy Conference,* Southampton, 2011.

[96] P. Scheers and W. Rutten, “Lower churchill project: Rock berm concept development study report,” Tideway BV, Netherlands, 2011.

[97] “The Art of Dredging,” Marc Van de Velde, 20 11 2013. [Online]. Available: http://www.theartofdredging.com/rockdumping.htm. [Accessed 2013].

[98] “Concrete Mattress Scene,” QLEE, 20 11 2013. [Online]. Available: http://www.turbosquid.com/3d-models/3d-concrete-mattress-scene/714314. [Accessed 2013].

[99] SUBMAT, “Pipeline protection and stabilisation systems,” SLP Engineering, Lowestoft, 2007.

[100] W. H. Somerton, Thermal Properties and Temperature-Related Behavior of Rock/Fluid Systems, Amsterdam: Elsevier, 1992.

[101] W. Woodside and J. H. Messmer, “Thermal conductivity of porous media. I. Unconsolidated sands,” *Journal of Applied Physics*, vol. 32, no. 9, pp. 1688-1699, 1961.

[102] "Seawater," Encyclopædia Britannica, Inc., 2011-2013. [Online]. Available: http://www.britannica.com/EBchecked/topic/531121/seawater/301669/Optical-properties. [Accessed Dec 2013].

[103] C. J. F. Böttcher, Theory of Electric Polarization, Amsterdam: Elsevier Science, 1952, p. 377.

[104] Z. Hashin and S. Shtrikman, "A variational approach to the theory of the elastic behavior of multiphase materials," *Journal of the Mechanics and Physics of Solid,* vol. 11, no. 2, pp. 127-140, 1963.

[105] J. C. Maxwell, A Treatise on Electricity and Magnetism, Oxford: Clarendon Press, 1873.

[106] R. W. Zimmerman, "Thermal conductivity of fluid-saturated rocks," *Journal of Petroleum Science and Engineering,* vol. 3, no. 3, pp. 219-227, 1989.

[107] D. Kunii and J. M. Smith, "Heat transfer characteristics of porous rocks," *AIChE Journal,* vol. 6, no. 1, pp. 71-78, 1960.

[108] A. Revil, "Thermal conductivity of unconsolidated sediments with geophysical applications," *Journal of Geophysical Research,* vol. 105, no. 7, pp. 16749-16768, 2000.

[109] K. S. Mendelson and M. H. Cohen, "The effect of grain anisotropy on the electrical properties of sedimentary rocks," *GEOPHYSICS,* vol. 47, no. 2, pp. 257-263, 1982.

[110] E. E.-M. Gomaa, Thermal Behavior of Partially Liquid Saturated Porous Media, Berkeley, USA: University of California, Berkeley, 1973, p. 650.

[111] H. Ozbek, Thermal Conductivity of Multi-fluid Saturated Porous Media, Berkeley, USA: University of California, Berkeley, 1976.

[112] A. Ghaffari, A Model for Predicting Thermal Conductivity of Rock-fluid Systems, Berkeley, USA: University of California, Berkeley, 1980.

[113] C. T. Hsu, P. Cheng and K. W. Wong, "A lumped-parameter model for stagnant thermal conductivity of spatially periodic porous media," *Journal of Heat Transfer,* vol. 117, no. 2, pp. 264-269, 1995.

[114] D. L. Turcotte and G. Schubert, Geodynamics: Second Edition, Cambridge, UK: Cambridge University Press, 2002.

[115] D. A. Nield and A. Bejan, Convection in Porous Media: Third Edition, New York: Springer, 2006.

[116] R. M. Fand, T. E. Steinberger and P. Cheng, "Natural convection heat transfer from a horizontal cylinder embedded in a porous medium," *International Journal of Heat and Mass Transfer,* vol. 29, no. 1, pp. 119-133, 1986.

[117] A. Nejan, Convection Heat Transfer, New York: Wiley, 1984.

[118] M. A. Combarnous and S. A. Bories, "Hydrothermal convection in saturated porous media,"

Advances in Hydroscience, vol. 10, pp. 231-307, 1975.

[119] K. J. Schneider, “Investigation of the influence of free thermal convection in heat transfer through granular material,” in *Proceeding of 11th International Congress of Refrigeration,* USA, 1963.

[120] R. J. Buretta and A. S. Berman, “Convective heat transfer in a liquid saturated porous layer,” *Journal of Applied Mechanics,* vol. 43, pp. 249-253, 1976.

[121] Y. C. Yen, “Effects of density inversion on free convective heat transfer in porous layer heated from below,” *International Journal of Heat and Mass Transfer,* vol. 17, pp. 1349-1356, 1974.

[122] J. W. Elder, “Steady free convection in porous layer heated from below,” *Journal of Fluid Mechanics,* vol. 27, pp. 29-48, 1967.

[123] T. Kaneko, M. F. Mohtadi and K. Aziz, “An experimental study of natural convection in inclined porous media,” *International Journal of Heat and Mass Transfer,* vol. 17, pp. 485-496, 1974.

[124] V. P. Gupta and D. D. Joseph, “Bounds for heat transport in a porous layer,” *Journal of Fluid Mechanics,* vol. 57, pp. 491-514, 1973.

[125] J. M. Strauss, “Large amplitude convection in porous media,” *Journal of Fluid Mechanics,* vol. 64, pp. 51-63, 1974.

[126] M. A. Combarnous and P. Bia, “Combined free and forced convection in porous media,” *Journal of Petroleum Science and Engineering,* vol. 11, pp. 399-405, 1971.

[127] P. Cheng, “Heat transfer in geothermal systems,” *Advances in Heat Transfer,* vol. 14, pp. 1-105, 1978.

[128] P. Cheng, “ME627 lecture notes,” University of Hawaii, Hawaii, 1980.

[129] J. H. Merkin, “Free convection boundary layers on axisymmetric and two-dimensional bodies of arbitrary shape in saturated porous medium,” *International Journal of Heat and Mass Transfer,* vol. 22, pp. 1461-1462, 1979.

[130] D. B. Ingham and I. Pop, “Natural convection about a heated horizontal cylinder in a porous medium,” *Journal of Fluid Mechanics,* vol. 184, pp. 157-181, 1987.

[131] “Specific Metals and Alloys,” in *Metal Handbook, Volume 2, Properties and Selection: Naonferrous Alloys and Special-Purpose Materials*, Celeveland, ASM International, 1990, pp. 545-555.

[132] M. H. Sharqawy, J. H. Lienhard V and S. M. Zubair, “Thermophysical properties of seawater: a review of existing correlations and data,” *Desalination and Water Treatment,* vol. 16, no. 1-3, pp. 354-380, 2010.

[133] R. D. Hyndman and M. J. Drury, “Physical properties of basalts, gabbrob, and ultramafic rocks,” *Deep Sea Drilling Project Reports and Publications,* vol. 37, pp. 395-401, 2007.

[134] W. J. Cho, S. Kwon and J. W. Choi, “The thermal conductivity for granite with various water contents,” *Engineering Geology,* vol. 107, no. 3-4, pp. 167-171, 2009.

[135] F. J. Millero and A. Poisson, “International one-atmosphere equation of state of seawater,” *Deep Sea Research Part A. Oceanographic Research Papers,* vol. 28, no. 6, pp. 625-629, 1981.

[136] M. Hill, “Physical properties of sea water,” National Physical Laboratory, 2013. [Online]. Available: http://www.kayelaby.npl.co.uk/general_physics/2_7/2_7_9.html. [Accessed 23 Oct 2013].

[137] L. Talley and M. Hendershott, “SIO 201: Introduction to Physical Oceanography,” Sep 2013. [Online]. Available: http://www-pord.ucsd.edu/~ltalley/sio210/readings/gill_appendix3_ppsw.pdf. [Accessed Oct 2013].

[138] J. Bear, Dynamics of Fluids in Porous Media, USA: American Elsevier, 1972.

[139] N. Ramsing and J. Gundersen, “Seawater and Gases (UNISENSE),” 2013. [Online]. Available: http://www.unisense.com/files/PDF/Diverse/Seawater%20&%20Gases%20table.pdf. [Accessed 22 Oct 2013].

[140] “Introduction to COMSOL Multiphysics,” COMSOL Inc, Nov 2013. [Online]. Available: http://www.uk.comsol.com/shared/downloads/IntroductionToCOMSOLMultiphysics.pdf. [Accessed Apr 2014].

[141] P. L. Lewin, J. E. Theed, A. E. Davies and S. T. Larsen, “Method for rating power cables buried in surface troughs,” in *IEE Proc. Generation, Transmission and Distribution*, 1999.

[142] O. C. Zienkiewicz, C. Emson and P. Bettess, “A novel boundary infinite element,” *International Journal for Numerical Methods in Engineering,* vol. 19, pp. 393-404, 1983.

[143] E. Holzbecher and H. Si, “Accuracy tests for COMSOL - and delaunay meshes,” in *COMSOL Conference 2008 Hannover*, Hanover, 2008.

[144] S. V. Patankar, Numerical Heat Transfer and Fluid Flow, Washington: Hemisphere Pub.Co., 1980.

[145] C. Long, Essential Heat Transfer, Malaysia: Pearson Education Limited, 1999.

[146] J. Arrillaga, Y. H. Liu and N. R. Watson, Flexible Power Transmission: The HVDC Options, Hoboken, NJ: Wiley, 2007.

[147] C. W. Lander, Power Electronics, 3rd Edition, London: McGraw-Hill, 1993.

[148] D. S. Sarali and P. Shailaja, “Mitigation of harmonics using thyristor based 12 pulse voltage source PWM rectifier,” *Internation Journal of Research in Engineering and Technology,* vol. 1, no. 3, pp. 267-270, 2012.

[149] T. B. Wood, D. E. Macpherson, D. Banham-Hall and S. J. Finney, “Ripple current propagation in bipole HVDC cables and applications to DC grids,” *IEEE Transaction on*

Power Delivery, vol. 29, no. 2, pp. 926-933, 2014.

[150] G. Mazzanti and M. Marzinotto, Extruded Cables for High-Voltage Direct-Current Transmission: Advances in Research and Development, Wiley-IEEE Press, 2013.

[151] Cigre Working Group 02-Study Committee 21, *Recommendations for tests of power transmission dc cables for a rated voltage up to 800kv,* Electra(189), 2000.

[152] E. Occhini and G. Maschio, "Electrical characteristics of oil-impregnated paper as insulation for hv dc cables," *Power Apparatus and Systems, IEEE Transactions on,* Vols. PAS-86, no. 3, pp. 312-326, 1967.

[153] E. Kuffel, W.S. Zaengl and J. Kuffel, High Voltage Engineering: Fundamentals, 2 ed., Oxford: Newnes, 2000, p. 534.

[154] M. Wang, K. D. Srivastava, J. B. Neilson and A. J. Vandermaar, "Analysis of voltage-time breakdown data for oil-impregnated paper insulation," *Electrical Insulation, IEEE Transactions on,* vol. 26, no. 4, pp. 837 - 839, 1991.

[155] T. Nara, K. Kato, F. Endo and H. Okubo, "Study on dielectric breakdown at dc polarity reversal in oil/pressboard-composite insulation system," in *Electrical Insulation and Dielectric Phenomena, 2009. CEIDP'09. IEEE Conference on*, 2009.

[156] Z. Y. Huang and J. A. Pilgrim, "Thermomechanical pressure analysis for HVDC cables," in *Jicable HVDC'13,* Perpignan, 2011.

[157] Q. Zhang, H. Wang, C. Guo and S. Ma, "Research on the thermal expansion coefficient of electrical insulating oil," *Petroleum Processing and Petrochemicals,* vol. 43, no. 10, pp. 55-59, 2012.

[158] Handbook of Physical Testing of Paper: Volume 2, 2rd ed, Boca Raton: CRC Press Inc, 2001.

[159] L. A. Bloomfield, How Things Work: The Physics of Everyday Life, 3rd Edition, John Wiley & Sons, 2005.

[160] R. C. Hibbeler, "Strain transformation," in *Mechanics of Materials,* Singapore, PERSON HALL, 2010.

[161] E. M. Hackett, K. H. Schwalbe and R. H. Dodds, Constraint Effects in Fracture, Philadelphia: ASTM, 1993.

[162] Metal Handbook, Volume 2, Properties and Selection: Nonferrous Alloys and Special-Purpose Materials, Celeveland: ASM International, 1990.

[163] "Thermal conductivity of seawater and its concentrates," TWT department of MPEI, 2013. [Online]. Available: http://twtmas.mpei.ac.ru/mas/Worksheets/HEDH/Tab-5-5-13-2-Ther-Cond-Seawater.mcd. [Accessed Jan 2014].

[164] G. J. Anders and B. Heinrich, "Cable crossings-derating considerations. II. example of derivation of derating curves," *IEEE Transactions on Power Delivery,* vol. 14, no. 3, pp.

715-720, Jul 1999.